Extreme Mechanics Letters 86 (2026) 102496

Contents lists available at ScienceDirect

Extreme Mechanics Letters

journal homepage: www.elsevier.com/locate/eml

Mechano-diffusion of particles in hydrogels

Jie Ma [a,1], Tsz Hung Wong [a,1], Zhaohan Yu [a], Xinzhe Dai [b], Chuwei Ye [a], Jingjie Yeo [b], Shaoting Lin [a,c,*]

[a] Department of Mechanical Engineering, Michigan State University, East Lansing, MI, USA
[b] Sibley School of Mechanical and Aerospace Engineering, Cornell University, Ithaca, NY, USA
[c] Department of Mechanical Engineering, University of Wisconsin-Madison, Madison, WI, USA

ARTICLE INFO

Keywords:
Mechano-Diffusion
Network-Topology
Nanoparticle Diffusion
Polymer mechanics
Drug Delivery

ABSTRACT

Particle transport is traditionally described by the Stokes–Einstein relation, where diffusivity is primarily governed by particle size and medium viscosity, resulting in a relatively limited design flexibility for controlling transport behavior. Recent studies have shown that modulating the mechanical state of soft materials can dynamically regulate particle diffusion, a phenomenon referred to as mechano-diffusion, introducing a new design dimension for engineering transport in polymer networks. Such mechano-diffusion processes are particularly important in systems where the regulation of particle transport within soft media directly determines system performance, including controlled molecular delivery, selective transport across polymer networks, and particle transport in biological and environmental systems. In recent years, increasing attention has been devoted to mechanics-coupled particle transport in soft materials, motivating the need for a timely and comprehensive review. This review aims to provide a systematic overview of mechano-diffusion by (i) summarizing the fundamental mechanisms governing particle transport in polymer networks, (ii) introducing experimental platforms and computational tools to elucidate transport dynamics, and (iii) highlighting emerging strategies for engineering selective and controllable particle transport for future applications. Overall, this review establishes a unified perspective on mechano-diffusion that bridges polymer mechanics and particle transport, providing new insights for engineering responsive and selective transport processes in soft materials.

1. Introduction

Particle transport in soft materials constitutes a fundamental process underlying a wide range of biological functions [1–5] and technological operations [6–10]. In biological systems, polymeric and hydrogel-like networks serve as the primary media through which molecules, nanoparticles, and macromolecular species migrate within cellular environments, tissues, and organs [11–15]. Beyond biological systems, particle transport in soft and hydrated polymer networks underpins a variety of engineered processes in which controlled molecular mobility and selective transport, such as controlled delivery systems [16–18], selective separation across polymer membranes [19–22], and particle transport in catalytic, filtration, and environmental technologies [9,23–25]. In these contexts, the migration kinetics, transport pathways, and particle–network interactions directly determine transport efficiency, particle permeability, and network selectivity of the system [9,26–29]. Consequently, understanding and controlling particle transport in polymer networks represents a fundamental problem in polymer physics and materials science, with broad implications for bioengineering, nanotechnology, and environmental systems [30–33].

Particle transport is traditionally described within the framework of Brownian diffusion, most commonly captured by the Stokes–Einstein relation, which relates the diffusivity of particles to their size and the viscosity of the surrounding medium [34–36]. Within this classical description, the transport behavior of particles is primarily determined by their intrinsic parameters, while the transport medium is typically treated as a passive environment that does not actively participate in regulating particle motion. As a result, the ability to modulate particle transport is generally limited to adjusting particle properties or bulk fluid characteristics, offering relatively restricted flexibility for engineering transport behavior. While this framework provides a robust foundation for understanding diffusion in simple liquids and

* Corresponding author at: Department of Mechanical Engineering, Michigan State University, East Lansing, MI, USA.
E-mail addresses: linshaot@msu.edu, slin88@wisc.edu (S. Lin).
[1] These authors contribute equally.

https://doi.org/10.1016/j.eml.2026.102496
Received 30 March 2026; Received in revised form 21 May 2026; Accepted 27 May 2026
Available online 1 June 2026
2352-4316/© 2026 Elsevier Ltd. All rights are reserved, including those for text and data mining, AI training, and similar technologies.

homogeneous solutions, it becomes increasingly inadequate for describing particle migration in complex soft materials, where the geometric structure and energy state of polymer networks can dynamically influence transport processes [37–39].

In contrast to classical diffusion in simple fluids, particle transport in soft materials occurs within deformable and structurally heterogeneous environments, such as polymer networks, hydrogels, and biological matrices [28,40–42]. These media are composed of interconnected polymer chains that form porous and mechanically responsive networks, whose microstructure and mechanical state can be readily altered by external stimuli including mechanical deformation [43,44], osmotic swelling [45–48], or acoustic excitation [49]. As a consequence, particle transport in such systems is not governed solely by particle size and solvent viscosity, but is strongly influenced by the evolving configuration of the polymer network itself [41,50]. Recent studies have shown that mechanical modulation of polymer networks can dynamically regulate particle mobility, energy barriers for particle hopping, and effective transport pathways [41,50,51]. This mechanics-coupled transport behavior, often referred to as mechano-diffusion, introduces an additional design dimension for controlling particle transport by tuning the mechanical state of the surrounding network.

This strong coupling between mechanics and transport in soft materials arises from the intrinsic structural characteristics of polymer networks. Unlike pure liquids, polymer networks consist of interconnected chains that form nanoscale meshes and dynamically fluctuating pores through which particles migrate [39,52,53]. Mechanical deformation or network reconfiguration can alter key structural parameters, including mesh size, pore connectivity, and local energy barriers for particle hopping, thereby modifying the transport landscape experienced by diffusing particles [51,54–57]. In many hydrogel and biological systems, particle diffusion therefore proceeds through mechanisms such as hopping [51], obstruction [57], or transient pore opening [41], which are highly sensitive to the mechanical state of the surrounding network [58]. As a result, mechanical perturbations can substantially amplify, suppress, or selectively regulate particle mobility, establishing a direct coupling between network mechanics and mass transport [58,59].

In recent years, mechanics-coupled particle transport in soft materials has attracted rapidly growing attention across multiple research communities. A series of experimental studies have demonstrated that external mechanical stimuli can dynamically regulate particle mobility in polymer networks [60,61]. Meanwhile, theoretical and computational investigations have provided new insights into the underlying transport mechanisms [62–65]. These advances collectively highlight mechano-diffusion as an emerging paradigm for regulating particle transport in complex soft environments. With the rapid expansion of this field, a timely synthesis of recent progress is essential to consolidate current understanding and to outline future opportunities for engineering controllable and selective transport processes in soft materials.

In this review, we provide a comprehensive overview of mechano-diffusion in soft materials and establish a unified perspective on mechanics-regulated particle transport in polymer networks. Specifically, we first summarize the fundamental physical mechanisms governing particle transport in deformable polymer networks, including diffusion modes associated with network structures, confinement effects, and mechanically modulated transport energy landscapes. We then introduce representative experimental platforms and computational approaches developed to quantify particle diffusivity and transport behavior in soft materials, enabling systematic investigation of mechano-diffusion under diverse mechanical stimuli. Finally, we discuss emerging strategies for engineering controllable and selective particle transport by leveraging mechano-diffusion, and highlight future opportunities in applications such as drug delivery, in-situ biosensing, and strain-induced hemostasis, as well as in the integration of high-throughput experimental platforms, computational simulations, and machine learning.

The review is organized as follows. **Section 2** introduces the biological and physical significance of mechano-diffusion. **Section 3** introduces the structural characteristics of polymer networks, with emphasis on network topologies, crosslinking mechanisms, and their mechanical properties. **Section 4** discusses the fundamental diffusion behaviors of particles in undeformed polymer networks, establishing the baseline transport regimes governed by the particle–mesh size relationship. **Sections 5** and **6** then examine mechano-diffusion in deformed polymer networks under static and dynamic mechanical loading, respectively, highlighting how mechanical perturbations reshape transport pathways and diffusion regimes. **Section 7** summarizes experimental platforms developed to characterize mechano-diffusion, including both indirect ensemble-based methods and direct single-particle tracking approaches. **Section 8** reviews computational simulation strategies for studying particle transport in polymer networks, covering model construction, and trajectory-based analysis of transport observables. **Section 9** discusses stimuli-responsive molecular transport in polymer networks and presents a unified framework for understanding stimulus-induced mechano-diffusion mechanisms. **Section 10** further extends the discussion to active particle transport in polymer networks, emphasizing the coupling between particle activity, network mechanics, and transport behavior. Finally, **Section 11** highlights representative applications of mechano-diffusion and outlines future perspectives, followed by concluding remarks..

2. Mechano-Transport in Biological Systems and Engineering Applications

The regulation of molecular transport by mechanical forces is ubiquitous across biological systems [66–68]. In living organisms, soft tissues are continuously exposed to mechanical cues arising from physiological activities such as tissue growth, organ motion, fluid pressure, and external mechanical stimulation [69–71]. These forces originate from diverse biological processes, including cellular proliferation, muscle contraction, blood flow, and interstitial fluid movement. As a result, biological tissues rarely exist in a mechanically steady state; instead, they function within dynamic mechanical environments in which stresses, deformations, and pressure gradients continuously evolve. Importantly, transport in these systems is not limited to mechano-diffusion in its strict sense, where deformation directly alters diffusive pathways [69,72–75]. More broadly, molecular transport in biological systems is often guided by mechanical forces through multiple modes, including pressure-driven flow, deformation-coupled diffusion, and force-mediated interstitial transport [66,76,77].

Mechanical forces can substantially influence mass transport processes within biological environments through several coupled mechanisms [75,78,79]. First, mechanical loading can directly alter the microstructure of soft tissues by deforming extracellular matrices, compressing porous structures, and modifying pore connectivity within the interstitial space [80–83]. Such structural changes regulate the effective pathways available for molecular diffusion and particle migration. Second, mechanical forces can generate or modify pressure gradients and interstitial fluid flow within tissues, thereby introducing convective transport in addition to diffusion [83,84]. Third, mechanical stresses can influence the spatial organization and packing density of cells and extracellular matrices, producing heterogeneous transport environments in which local diffusivity and permeability vary significantly across the tissue [85–87]. Consequently, the transport of molecules, nutrients, and therapeutic agents in biological tissues is often strongly coupled with mechanical loading conditions rather than being governed solely by intrinsic physicochemical properties.

Static mechanical stresses are particularly prominent in dense biological environments such as solid tumors [88,89] (Fig. 1). During tumor growth, the continuous proliferation of cancer cells and the excessive deposition of extracellular matrix (ECM) components generate compressive stress within the tumor mass [90–92]. These stresses can

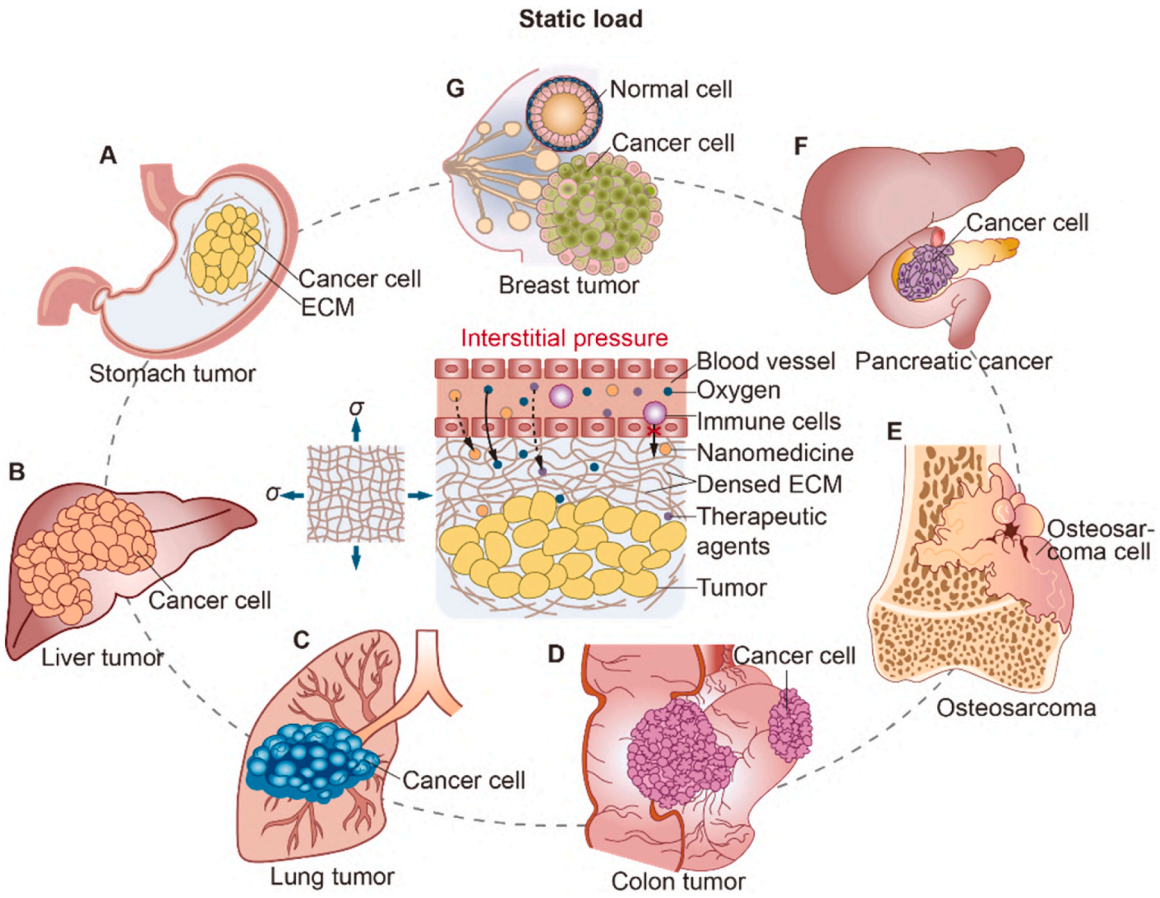


Fig. 1. Static mechanical loading in tumor microenvironments. Solid tumors generate compressive stresses and elevated interstitial pressure due to tumor growth and dense extracellular matrix (ECM), which regulate the transport of oxygen, immune cells, nanomedicines, and therapeutic agents. Representative tumors include stomach (A), liver (B), lung (C), colon (D), osteosarcoma (E), pancreatic (F), and breast (G).

compress surrounding tissues and blood vessels while simultaneously elevating interstitial fluid pressure within the tumor microenvironment [90,92,93]. Elevated interstitial pressure reduces the pressure gradient between blood vessels and the tumor interstitium [94], thereby hindering the transvascular transport and penetration of therapeutic molecules [89,95]. In addition, the dense ECM network, composed of collagen fibers, glycoproteins, and proteoglycans, forms a complex porous architecture that restricts molecular diffusion and nanoparticle transport [87,96]. ECM not only reduces effective pore accessibility but also creates highly tortuous transport pathways, resulting in heterogeneous spatial distributions of oxygen, immune cells, nanomedicine, and other therapeutic agents within tumor tissues [97,98]. As a consequence, mass transport in tumors becomes strongly dependent on the mechanical state of the surrounding microenvironment [93,99].

In contrast, many physiological tissues experience dynamic mechanical loading during periodic biological activities (Fig. 2) [68,100,101]. Examples include compression in intervertebral discs during daily spinal loading, peristaltic motion in the gastrointestinal tract that drives luminal transport, cyclic contraction and relaxation of skeletal muscle during movement, sliding compression and fluid exudation in articular cartilage during joint motion, pulsatile shear stress generated by blood flow within vascular networks, and pressure-driven flow in lung interstitial spaces during respiration [102–106]. These dynamic mechanical forces can enhance or regulate molecular transport by periodically deforming tissue structures, inducing fluid flow, and modifying pore accessibility within soft biological matrices [80,107,108]. For example, cyclic compression of cartilage can drive interstitial fluid exchange that facilitates nutrient transport, while peristaltic motion in the intestine enhances mixing and transport of molecules [80,103]. Similarly, muscle contraction can generate transient pressure gradients that promote fluid redistribution and solute transport within surrounding tissues. Fundamentally, static and dynamic mechanical environments influence mass transport through distinct mechanisms [105,109–111]. Static mechanical stresses primarily regulate transport by altering the structural characteristics of the porous architecture, such as by compressing tissue structures, reducing pore accessibility, and modifying pressure gradients, which together restrict molecular diffusion and nanoparticle transport [112–114]. In contrast, dynamic mechanical loading can actively regulate transport by periodically deforming tissue structures and inducing fluid flow within biological matrices. As a result, static stresses mainly modify the structural conditions governing transport, whereas dynamic mechanical forces can directly enhance or regulate mass transport through coupled deformation and fluid movement [105,108,111,115].

Taken together, these observations highlight a fundamental principle: in soft biological tissues, molecular transport is frequently governed not only by physicochemical properties but also by the mechanical state of the surrounding structure. Mechanical forces can reshape transport pathways, alter energy barriers associated with molecular migration, and modulate the balance between diffusion and convection in complex biological matrices. Inspired by these biological systems, synthetic soft materials have been increasingly explored as model platforms for studying mechanics-regulated transport phenomena.

Among these materials, polymer networks represent a particularly versatile class of soft matter in which network topology, crosslinking mechanisms, and mechanical deformation can be systematically designed and controlled [59,116–118]. Because polymer networks share key structural similarities with biological extracellular matrices, they

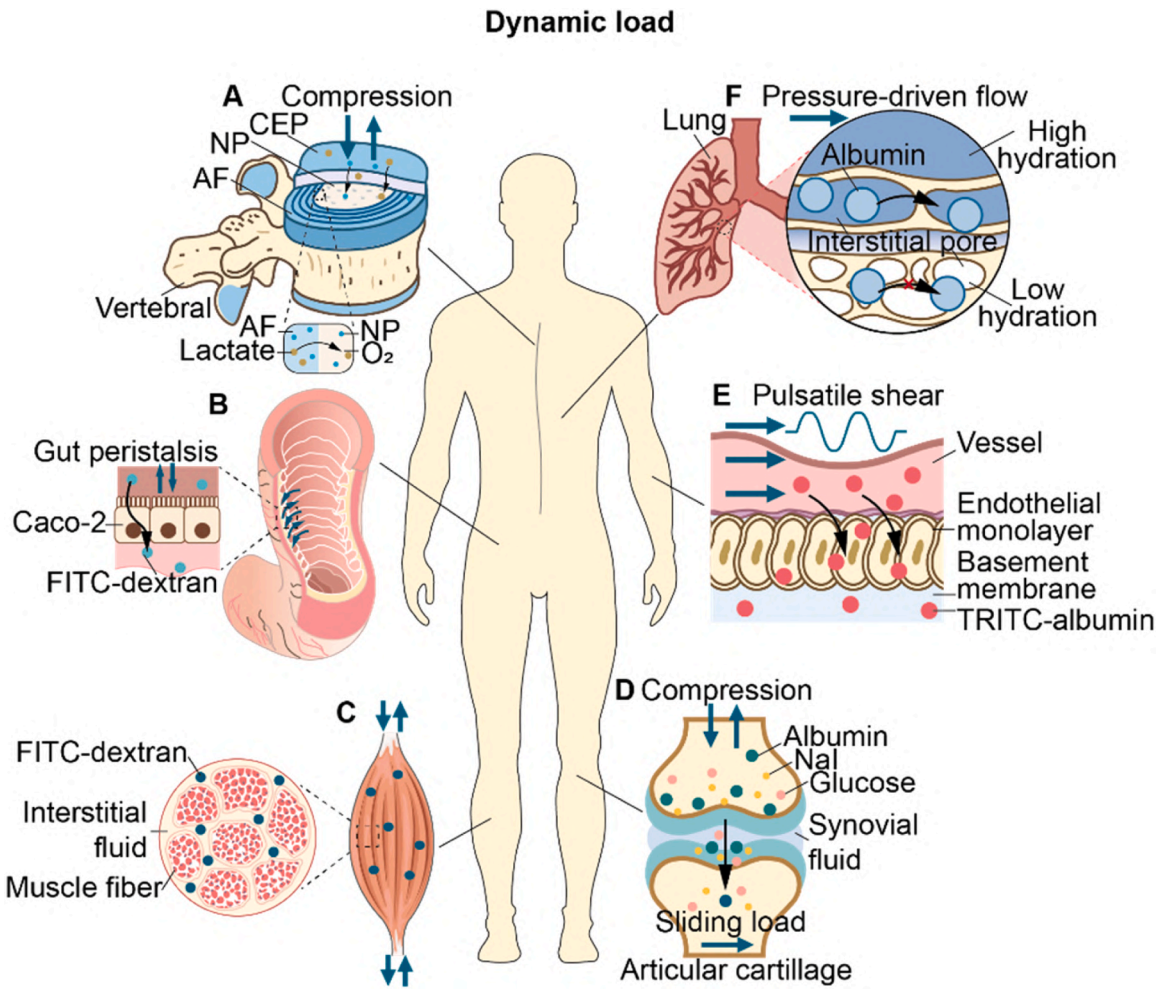


Fig. 2. Dynamic mechanical loading in physiological systems. Dynamic mechanical forces regulate molecular transport in tissues through mechanisms such as compression, peristalsis, muscle contraction, pulsatile shear, and pressure-driven flow. Representative examples include intervertebral disc (CEP refers to cartilage endplate, NP refers to nucleus pulposus, and AF refers to annulus fibrosus) (A), gut epithelium (B), skeletal muscle (C), articular cartilage (D), vascular endothelium (E), and lung interstitium (F).

provide an attractive platform for investigating how mechanical perturbations influence particle transport in soft materials. In particular, hydrogels—highly hydrated polymer networks—have emerged as one of the most widely studied systems due to their structural resemblance to biological tissues and their ability to accommodate diffusive transport for molecules and nanoparticles [119–122].

Building on these characteristics, extensive efforts have been devoted to developing stimuli-responsive hydrogel systems in which molecular transport can be actively regulated through externally applied triggers (Fig. 3). A wide range of external stimuli—including mechanical deformation [41,50,123–125], ultrasound [126–130], electric fields [131–133], light [134,135], thermal stimuli [136,137], swelling [138], and magnetic fields [139,140]—have been explored to modulate the structure and transport properties of polymer networks. Mechanical deformation can alter network anisotropy and pore accessibility through stretching, compression, or torsion, thereby modifying the effective diffusion pathways available for molecular migration. Ultrasound stimulation can generate acoustic cavitation and microstreaming that enhance molecular transport and facilitate drug release from hydrogel matrices. Electric fields can drive electrophoretic motion of charged species or induce electro-osmotic flow within hydrogel networks, enabling electrically controlled transport. Light-responsive hydrogels utilize photochemical reactions or photothermal effects to induce structural transitions in the network, while temperature-responsive systems rely on thermally induced phase transitions that alter polymer chain interactions and mesh size. Magnetic-field-responsive hydrogels, often incorporating magnetic nanoparticles, can undergo magnetically induced deformation or heating that further modulates transport behavior.

Collectively, these stimuli-responsive systems demonstrate that molecular transport in polymer networks can be dynamically regulated by external perturbations that modify network structure, fluid flow, or local energetic landscapes. Such approaches have been widely explored in applications including controlled drug delivery, wearable biomedical devices, transdermal transport, and implantable therapeutic systems [120,141–143]. Despite these advances, most existing studies have primarily focused on achieving stimulus-triggered release or enhancing overall diffusivity, whereas the fundamental physical mechanisms governing stimulus-regulated diffusion within polymer networks remain less clearly understood. Particularly, how mechanical perturbations modify transport pathways and energy barriers associated with particle migration in soft polymer networks remains an area that requires systematic investigation. It is worth noting that biological tissues are inherently evolving systems shaped by processes such as cellular growth and matrix remodeling, whereas most engineered materials possess relatively stable structures once formed, resulting in an inherent gap between biological and engineered transport environments.

Understanding these mechanisms is therefore essential for establishing a unified framework for mechanics-regulated transport in soft materials. In this context, polymer networks provide an ideal model



Fig. 3. Applications of externally regulated molecular transport in stimulus-responsive polymer networks. Representative examples of externally stimuli response to molecular release induced by (A–E) mechanical deformation, (F–J) ultrasound, (K–M) electric fields, (N, O) light, (P, Q) thermal stimuli, (R) swelling, (S) pH variation, and (T) magnetic fields. 123. Copyright American Chemical Society (A); from Ref. 124. Copyright Elsevier (B); from Ref. 129. Copyright the Royal Society of Chemistry (C); from Ref. 126. Copyright American Chemical Society (F); from Ref. 127. Copyright American Chemical Society (G); from Ref. 130. Copyright AAAS (J); from Ref. 132. Copyright Elsevier (L); and from Ref. 136. Copyright Elsevier (P). 80 under a CC BY-NC license, Springer Nature (D). 125 under a CC BY 4.0 license, AAAS (E). 131 under a CC BY 4.0 license, Springer Nature (K), and from Ref. 135 under a CC BY 4.0 license, Springer Nature (O). 128 under a CC BY license, Elsevier (H), and from Ref. 129 under a CC BY license, Wiley (I), from Ref. 133 under a CC BY license, Wiley (M), and from Ref. 134 under a CC BY license, Wiley (N). 137. Copyright Wiley (Q); from Ref. 138. Copyright Wiley (R); from Ref. 139. Copyright Wiley (S); and from Ref. 140. Copyright Springer Nature (T). (a) Reproduced with permission from Ref. (b) Adapted from Ref. (c) Adapted from Ref. (d) Adapted from Ref. (e) Adapted from Ref. (f) Adapted with permission from Ref.

platform because their structural topology, crosslinking chemistry, and mechanical responses can be precisely designed and controlled. By systematically examining the structural characteristics of polymer networks, it becomes possible to elucidate how mechanical deformation and other external stimuli influence particle diffusion and transport behavior in soft materials.

3. Network Architecture, Mechanical Properties, and Particle Descriptors

In classical diffusion studies, mass transport is most often examined in media that are structurally invariant, such as homogeneous solutions [144,145]. In such systems, diffusion behavior is primarily determined by the intrinsic properties of the medium, such as its viscosity, temperature, or microstructural characteristics, which remain essentially constant. The medium is therefore typically treated as a passive transport environment whose structure does not respond to external perturbations. By contrast, polymer networks represent a fundamentally different class of transport media that are intrinsically deformable and structurally reconfigurable (Fig. 4 **left**). Constructed from flexible polymer chains interconnected by crosslinking points, polymer networks can undergo substantial conformational rearrangements and topological reorganization under external stimuli, particularly mechanical deformation. As a result, unlike diffusion in conventional systems where transport is largely governed by solvent properties, diffusion in polymer networks is controlled jointly by particle characteristics and the structure and mechanical state of the polymer network, whose deformation-induced structural changes actively regulate molecular transport [146–148].

Within this framework, particle diffusion and release in polymer networks emerge from the interplay between particle attributes and network structure. Particle properties—such as size, shape, mechanical rigidity, and surface chemistry—govern how particles interact with polymer chains and traverse the network environment (Fig. 4 **upper right**) [146,147,149,150]. At the same time, the architecture of the polymer network, together with its deformation-induced structural evolution, defines the spatial accessibility and connectivity of transport pathways (Fig. 4 **lower right**) [151,152]. Distinct network topologies can respond to applied strain through markedly different modes of structural reconfiguration, resulting in pronounced differences in the emergence, redistribution, or suppression of accessible transport routes. Consequently, the influence of mechanical deformation extends beyond a simple geometric modulation of diffusion pathways. Rather, deformation can fundamentally redefine the permeability of polymer networks by reorganizing their internal network structures. Under such conditions, polymer networks may display markedly different diffusion and penetration behaviors toward different particles in undeformed and deformed states. Upon deformation, an initially restrictive polymer network may open transport pathways for some particles while continuing to exclude others, thereby giving rise to selective diffusion governed by the interplay between particle characteristics and the deformation-dependent structure of the network [146,153]. Through mechanical regulation of polymer network structure, diffusion thus emerges as a state-dependent and particle-dependent transport process with inherent selectivity. This perspective provides a unifying basis for understanding the diverse diffusion behaviors observed in polymer networks and establishes a conceptual foundation for subsequent discussions of diffusion control mechanisms and their manifestation across different application contexts.

3.1. Deformable Polymer Networks

3.1.1. Network Architecture

One key parameter governing particle transport is the architecture of the polymer network through which diffusion occurs. Establishing this framework provides a basis for analyzing particle–network coupled diffusion and understanding how polymer deformation influences transport behavior. Given the fundamental differences among polymer networks, systems reported in the literature can be categorized based on two key structural dimensions: network architecture and crosslinking mechanism.

Fig. 5**A** illustrates randomly crosslinked network, which refers to three-dimensional polymer networks formed through covalent or physical crosslinks that are randomly distributed in space [154,155]. In such networks, the positions of crosslinks, the lengths of network strands, and the local connectivity are not strictly controlled, resulting in statistically distributed structural features [156]. Owing to their simple fabrication and broad material compatibility, randomly crosslinked networks represent the most common and fundamental class of polymer networks and are widely used as baseline systems for understanding and comparing the mechanical behavior of different network architectures. At the structural level, the intrinsic randomness in crosslink distribution and strand length inevitably introduces pronounced network heterogeneity, causing different regions of the network to carry and accommodate mechanical loads in markedly different ways [156,157]. As a result, under mechanical deformation, stress cannot be transmitted uniformly throughout the network and instead tends to concentrate in short strands or regions of locally high crosslink density, where mechanical instability is preferentially initiated [156,158]. This structural heterogeneity directly limits the stretchability and fracture resistance of randomly crosslinked networks. With increasing crosslink density, the network modulus increases substantially; however, the stretchability and energy dissipation capacity decrease rapidly due to the absence of reconfigurable or dissipative structural motifs, leading to a pronounced

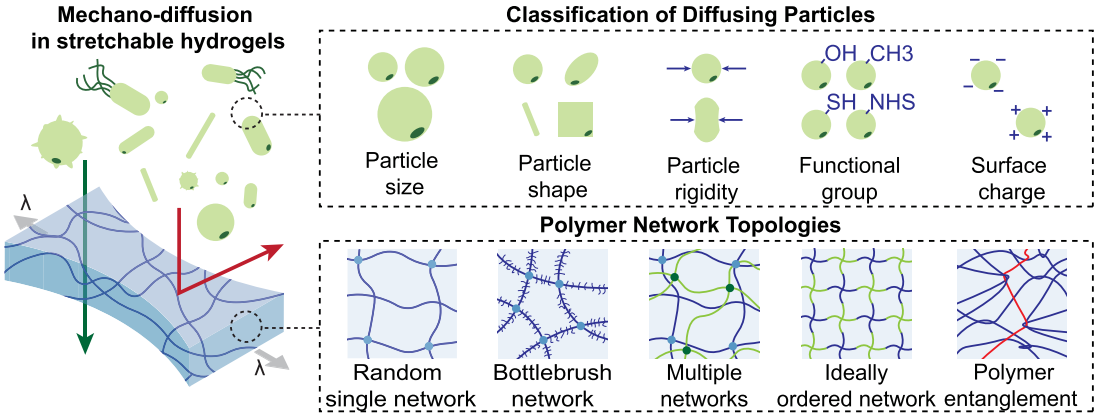


Fig. 4. Schematic overview of mechano-diffusion. Deformation-induced coupling between particles and polymer networks as a unifying mechanism for tunable transport in soft materials.

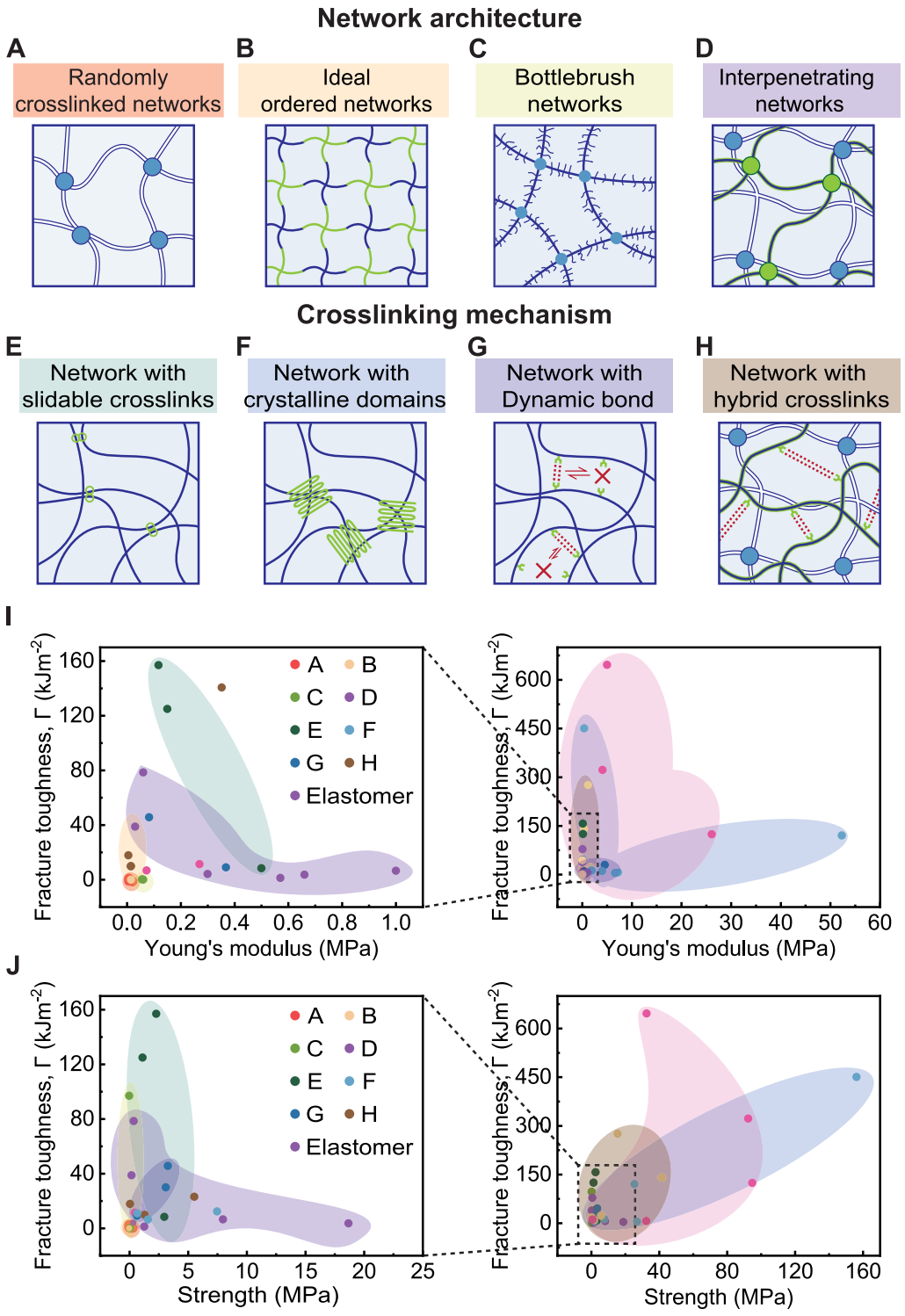


Fig. 5. Polymer network architectures and their mechanical property. A–H. Schematic representations of representative polymer network topologies: (A) randomly crosslinked, (B) ideally ordered, (C) bottlebrush, (D) multiple, (E) slidable crosslink, (F) crystalline-domain, (G) dynamic-bond, and (H) hybrid-crosslink networks. Literature-reported mechanical property distributions of various polymer architectures shown as Young's modulus versus fracture toughness (I) and strength versus fracture toughness (J).

stiffness–toughness trade-off [154,158,159]. Consequently, failure in these networks is typically governed by localized instability, and the fracture behavior is characteristically brittle [158,159]. Quantitatively, for conventional single-network hydrogels lacking effective energy-dissipation mechanisms—such as standard polyacrylamide (PAAm) hydrogels with random covalent crosslinking—their fracture toughness typically falls within a low range of $\Gamma \approx 1-10$ Jm^{-2} (Fig. 5**I**, **J**) [160,161]. Notably, PAAm hydrogels prepared with low crosslink concentrations and substantial chain entanglement can also exhibit relatively high toughness, as will be discussed later [162]. This magnitude has been widely reported in the literature and is commonly regarded as a representative benchmark for brittle single-network

hydrogels [159].

In contrast to randomly crosslinked networks, ideal networks are constructed through precise molecular design and well-controlled synthetic strategies [163]. Their crosslink connectivity, strand length, and overall network topology are highly uniform, closely approximating the assumptions of ideal elastic network models (Fig. 5**B**) [164–166]. Representative examples include end-linked star-shaped networks, where the synthesis is specifically designed to systematically suppress the broad strand-length distributions, dangling chains, and loop defects that are prevalent in randomly crosslinked systems. Structurally, this high degree of uniformity significantly reduces spatial heterogeneity within the network, allowing mechanical stress to be distributed more evenly under deformation and rendering stress transfer closer to the ideal affine deformation assumption. As a result, ideal networks typically exhibit highly predictable elastic responses that closely match theoretical models, with their modulus being precisely tunable through strand length and crosslink density [167]. Nevertheless, similar to randomly crosslinked networks, ideal networks generally lack intrinsic energy-dissipation or reconfigurable mechanisms [168]. Under large deformation or crack propagation, load bearing is still dominated by covalent strand rupture [168]. Although statistical stress concentration is alleviated, fracture extensibility and fracture toughness remain limited, and the overall failure behavior continues to be characterized by elastic dominance and low energy dissipation. From a mechanical perspective, ideal networks therefore represent a "structural uniformity limit," serving as an important reference framework for isolating and understanding the role of network heterogeneity in governing mechanical behavior.

Bottlebrush networks constitute another distinct class of polymer networks, in which the fundamental building blocks consist of polymer backbones densely grafted with side chains and subsequently crosslinked to form a three-dimensional network (Fig. 5**C**) [169,170]. In these systems, strong steric repulsion among the densely grafted side chains significantly stretches the backbone conformation, placing network strands in a highly extended state even in the absence of external deformation [171,172]. This architectural feature differentiates bottlebrush networks from both randomly crosslinked and ideal networks. Structurally, the presence of dense side chains effectively suppresses backbone entanglement and local chain collapse [172–174], thereby reducing network heterogeneity arising from strand-length fluctuations or topological defects, while simultaneously imparting enhanced conformational flexibility at the chain level. Consequently, under mechanical loading, bottlebrush networks typically exhibit lower effective moduli and more gradual stress–strain responses [174–176], with relatively uniform stress distribution and substantially reduced local stress concentration compared with randomly crosslinked networks (Fig. 5**I**, **J**). The enhanced softness and conformational flexibility introduced by side-chain grafting primarily modify chain conformation and deformation modes, rather than introducing new energy-dissipation pathways. In the absence of reversible bonds, sacrificial structures, or multi-network architectures, fracture in bottlebrush networks is still governed predominantly by covalent rupture of backbone chains or crosslinking points, resulting in only limited improvement in fracture toughness [177,178]. Accordingly, from a mechanical standpoint, bottlebrush networks represent a class of single-network systems in which molecular-level architectural design effectively modulates softness and stress distribution, while the overall energy-dissipation capacity and fracture resistance remain intrinsically constrained.

Apart from single networks, interpenetrating networks refer to polymer systems formed by two or more interpenetrating or sequentially constructed networks with distinct structural characteristics or crosslinking densities (Fig. 5**D**) [179,180]. Unlike single networks, interpenetrating networks typically combine a relatively rigid, highly crosslinked primary network with a more compliant, loosely crosslinked secondary network, each contributing differently to mechanical response and structural stability [181,182]. At the structural level, the presence of network components with different stiffness and extensibility creates a hierarchical architecture that enables load redistribution and transfer between networks [154]. During deformation, the stiffer network preferentially undergoes local damage, while the softer network preserves overall continuity, thereby suppressing rapid crack propagation [182,183]. In contrast to stress concentration caused by structural heterogeneity in randomly crosslinked networks, stress redistribution in interpenetrating networks arises from cooperative interactions and progressive damage among the constituent networks. Moreover, by varying polymer chemistry, crosslink density, mechanical properties, and the number of network components, interpenetrating networks provide substantial design flexibility for tuning mechanical performance. Mechanically, this hierarchical structure significantly alters the stiffness–toughness trade-off typical of single-network systems [154,179]. While homogeneous networks typically favor high strength and stiffness, heterogeneous network structures are generally more favorable for fracture resistance due to their enhanced energy-dissipation capability. Compared with randomly crosslinked, ideal, or bottlebrush networks, interpenetrating networks can achieve markedly higher fracture extensibility and toughness while maintaining relatively high modulus and strength (Fig. 5**I**, **J**). This enhancement originates primarily from irreversible damage of the primary network, which dissipates mechanical energy, while the secondary network maintains load-bearing capacity [181–183]. In cyclic loading–unloading experiments, this mechanism is reflected in pronounced hysteresis loops and high hysteresis ratios, indicating efficient energy dissipation [182, 184]. Consequently, interpenetrating networks represent a class of polymer networks in which hierarchical structure and controlled damage mechanisms enable enhanced fracture resistance and stable, energy-dissipative failure behavior.

3.1.2. *Crosslinking Mechanisms*

In addition to network topology, the physical nature and connectivity of crosslinking points also play an important role in determining the mechanical properties of polymer networks. Among them, slidable crosslinks form a distinctive class in which crosslinking points can move along polymer chains while maintaining network connectivity (Fig. 5**E**) [185,186]. Unlike conventional covalent crosslinks that are spatially fixed, such structures are typically realized through ring-like molecules or topological architectures, allowing redistribution of strand length and local chain tension during deformation [187]. At the structural level, crosslink mobility alters stress distribution within the network, enabling loads to be redistributed over a larger volume, reducing local stress concentration, and promoting more uniform chain deformation [187]. In contrast to randomly crosslinked networks, where stress heterogeneity arises from strand-length variations and structural disorder, stress redistribution in slidable crosslink networks primarily results from crosslink mobility. Mechanically, this movable connectivity enhances extensibility and delays crack initiation and propagation, helping the material maintain structural integrity at large strains. Unlike multiple-network systems, slidable crosslink networks do not rely on bond rupture or sacrificial structures for substantial energy dissipation, their mechanical improvement mainly arises from stress homogenization. Consequently, slidable crosslink networks represent a class of polymer networks in which crosslink mobility regulates stress transfer pathways, leading to more stable fracture behavior than conventional randomly crosslinked networks, while their intrinsic energy-dissipation capacity remains relatively constrained [188].

Another representative class of crosslinking mechanism arises from crystalline domains that act as physical crosslinks (Fig. 5**F**) [189–191]. In such networks, polymer chains form locally ordered regions through crystallization, and these crystalline domains function as junction points that connect chains and restrict their motion [192–194]. Unlike conventional covalent crosslinks, these junctions originate from intermolecular ordering, and their formation and disruption are typically governed by temperature, strain, or other external conditions. At the

structural level, crystalline domains are usually dispersed throughout the network as finite-sized but relatively strong physical nodes. Their presence increases the effective crosslink density while introducing hierarchical organization associated with phase structure. During deformation, crystalline domains can progressively fracture or melt, altering network connectivity and releasing localized stress [195,196]. In contrast to slidable crosslink networks, where stress redistribution arises primarily from crosslink mobility, stress regulation in crystalline-domain networks is dominated by the progressive failure of physical junctions. From a mechanical perspective, these breakable physical crosslinks can significantly enhance energy dissipation and, in many cases, improve fracture toughness (Fig. 5**I**, **J**) [190,197,198]. Under cyclic loading–unloading, the gradual disruption and partial reformation of crystalline domains often produce pronounced hysteresis loops, indicating substantial mechanical energy dissipation [190,199]. Consequently, polymer networks containing crystalline domains represent a class of materials in which phase transitions and breakable physical junctions provide effective energy-dissipation mechanisms. Their mechanical behavior differs fundamentally from that of slidable crosslink networks and offers an alternative structural strategy for enhancing strength and toughness in polymer networks.

In addition to energy dissipation through the fracture of physical junctions, another important crosslinking mechanism arises from dynamic bonds (Fig. 5**G**) [200,201]. In these networks, crosslinking points are formed by chemical bonds or physical interactions that can reversibly dissociate and reform under appropriate conditions, including hydrogen bonding, ionic interactions, or metal–ligand coordination [202]. These networks continuously reorganize their connectivity under deformation or external stimuli, allowing energy dissipation while maintaining overall network integrity [200,203]. At the structural level, the reversibility of dynamic bonds enables progressive bond rupture and reformation during loading, thereby continuously adjusting network connectivity and local stress distribution at the molecular scale. This dynamic rearrangement not only mitigates stress concentration but also imparts a degree of self-recovery to the material [204,205]. From a mechanical perspective, dynamic-bond networks typically exhibit pronounced hysteresis and strain-rate dependence, with energy dissipation arising from repeated bond breakage and reformation [206]. Compared with crystalline-domain networks, this dissipation mechanism is often more continuous and controllable, although the overall mechanical performance is constrained by the intrinsic bond strength and exchange kinetics. Consequently, dynamic-bond networks represent a class of polymer networks in which reversible connectivity and structural rearrangement enable effective energy dissipation and mechanical regulation, often leading to improved toughness, fatigue resistance, and self-recovery capability (Fig. 5**I**, **J**).

However, in many practical systems, a single crosslinking mechanism is insufficient to simultaneously achieve high strength, toughness, and structural stability. As a result, increasing attention has been devoted to hybrid crosslinking strategies, in which multiple types of crosslinks are incorporated within a single network (Fig. 5**H**) [189,207]. A common approach combines permanent covalent crosslinks with reversible physical interactions, allowing the permanent network to provide structural stability while the reversible network contributes to energy dissipation and stress redistribution [205,208,209]. Structurally, such systems often exhibit multi-scale or multi-mechanism architectures, where different crosslink types play distinct roles during deformation, enabling load sharing and progressive dissipation. Mechanically, hybrid-crosslinked networks can often achieve significantly enhanced fracture toughness and fatigue resistance while maintaining relatively high modulus and strength, owing to the synergistic action of multiple dissipation pathways [205,210]. Therefore, hybrid crosslinking represents an effective design strategy for overcoming the performance limitations of single crosslinking mechanisms and for achieving a balanced combination of strength, toughness, and stability in polymer networks (Fig. 5**I**, **J**).

In addition to hydrogels, elastomers also belong to the broader class of three-dimensional polymer networks formed by crosslinked polymer chains [211,212]. Their macroscopic mechanical behavior is similarly governed by chain elasticity, crosslink density, and network architecture. From this perspective, elastomers and hydrogels share a common physical foundation, and their deformation mechanisms can generally be interpreted within the framework of polymer network elasticity. The most fundamental difference between the two systems lies in the presence or absence of solvent [213,214]. Hydrogels typically contain a large fraction of water or other solvents and operate in a swollen state, resulting in relatively low polymer volume fractions and reduced effective load-bearing capacity of network strands [215]. In contrast, elastomers are usually used in dry or minimally swollen conditions, where the polymer volume fraction and chain density are significantly higher, allowing more efficient stress transfer and generally higher modulus and strength under comparable network structures [211,216,217]. Moreover, the presence of solvent in hydrogels introduces additional effects, including osmotic pressure, swelling-induced deformation, and polymer–solvent interactions, which often couple the mechanical response to environmental conditions [218–220]. From a mechanical standpoint, previous studies indicate that elastomers typically span a broader accessible range of moduli, strengths, and fracture energies than hydrogels, and in many cases reach higher overall values [191,221]. This difference largely arises from their higher polymer content and more effective load-bearing pathways. However, it should be noted that these ranges depend strongly on polymer chemistry, crosslinking strategy, and network architecture, and substantial variation exists among different classes of elastomers (Fig. 5**I**, **J**). Therefore, elastomers and hydrogels may be viewed as two representative soft material systems that share similar network physics but differ significantly in solvent content and chain density.

Taken together, the mechanical behavior of polymer networks can be systematically tuned over a wide range by controlling network topology and crosslinking mechanisms, which in turn regulate the available energy-dissipation pathways. From single-network systems such as randomly crosslinked, ideal, and bottlebrush networks, to multiple networks, slidable crosslinks, crystalline domains, dynamic bonds, and hybrid crosslinking strategies, a coherent structure–mechanics framework has emerged. The statistical distributions summarized in Fig. 5**I** and **J** should be interpreted as representative reference ranges rather than absolute boundaries, as the reported mechanical properties of polymer networks can vary significantly depending on material chemistry, processing conditions, and measurement methods. This framework not only provides a unified perspective for understanding the mechanical diversity of soft polymeric materials, but also establishes an essential foundation for analyzing how polymer networks regulate molecular transport and stimulus-responsive behavior.

3.2. *Diffusing Particles*

With the network microstructure defined above, the diffusion problem becomes inherently two-sided: the network specifies the constraints, whereas the particle determines how those constraints shape migration through the network. We therefore focus next on particle descriptors that govern mechano-diffusion under deformation. Transport of particles through polymer networks is commonly modeled as diffusion in a heterogeneous, deformable medium characterized by a mesh-scale microstructure. In mechano-diffusion, however, transport is governed not only by the network but also by the particle itself: its geometry, mechanics, and interactions define how the particle can move through the deformed network and thereby determine which migration mechanism dominates. We therefore classify diffusing particles using four key variables that map directly onto mechano-diffusion mechanisms: (i) particle size relative to the network mesh, (ii) shape anisotropy quantified by the aspect ratio (α), (iii) mechanical compliance relative to the host network, and (iv) particle–network interaction strength and

reversibility.

Size sets the baseline diffusion regime through the particle-to-mesh ratio and thus governs whether migration is well described by weakly hindered diffusion or requires activated escape from confinement. When the particle dimension is far below the characteristic mesh size, the network is modeled as an effective continuum and the diffusivity approaches the free-diffusion limit with modest hindrance. As the particle size approaches the mesh size, diffusion becomes increasingly controlled by transient pore availability and local chain rearrangements, and diffusion can become strongly hindered, increasingly intermittent, or effectively activated. Fig. 6 emphasizes that relevant biological and engineered particles span from a few nanometers (e.g., ferritin, proteins, and inorganic nanoparticles) to tens of micrometers and beyond (e.g., cells, oocytes, and microbeads), implying that mechano-diffusion cannot be discussed without specifying the size regime and the associated rate-limiting step.

3.2.1. Geometry

Shape and anisotropy introduce degrees of freedom that are less relevant for spheres—most notably rotation, alignment, and translation–rotation coupling—and these effects become decisive under deformation. Even in undeformed networks, anisotropy changes the set of orientations compatible with transient openings and therefore modifies the statistics of pore-crossing events. Under tensile or shear deformation, anisotropy becomes a direct route to mechanically programmable diffusion because deformation both biases particle orientation and generates direction-dependent pathway availability, leading to anisotropic effective diffusivities and mechanically gated selectivity. The broad aspect ratio distribution represented in Fig. 6—from near-spherical objects to filamentous phage and rod-like engineered particles—highlights that aspect ratio (α) is not a minor geometric detail but a key parameter for mechano-diffusion [222–232,235,233,234]. For example, Influenza A virus is typically on the order of 10^2 nm in diameter, placing it in a transport regime where motion through mucus and related extracellular barriers becomes sensitive to steric hindrance and transient pore accessibility [231]. HIV falls within a similar submicron size range, and its passage through mucosal and matrix-rich environments is likewise shaped by geometric confinement together with particle–matrix interactions [235]. By contrast, *Bacillus anthracis* in Fig. 6 represents a distinctly anisotropic biological particle, with an aspect ratio of approximately 5–8 [227]. Relative to near-spherical objects, such rod-like geometry introduces orientational constraints during migration through crowded or deformable networks, so that rotation, alignment with available pathways, and direction-dependent steric hindrance synergistically govern the diffusion behavior.

3.2.2. Mechanics

Mechanical compliance determines whether a particle behaves as a rigid excluded-volume obstacle or as a deformable body capable of accommodating confinement. More specifically, it governs how the deformation required for passage through a constriction is distributed between the particle and the surrounding network. When the particle moduli and network moduli are comparable—as in many biological objects and in soft engineered carriers such as microgels and microcapsules—transport can be facilitated by coupled deformation of both phases, which reduces steric penalties, alters the effective contact area, and lowers the energetic cost of traversing narrow openings. By contrast, stiff inorganic particles (e.g., diamond and metal oxides) behave much more like rigid inclusions, so that passage depends primarily on the availability of sufficiently large pathways and on the deformation capacity of the network itself, with geometric and topological constraints dominating the diffusion response. The wide modulus range summarized in Tables 1, 2 thus provides a concrete basis for distinguishing compliance-assisted diffusion from geometry-dominated diffusion in deformed polymer networks.

Representative cases in Tables 1, 2 further clarify how modulus maps onto diffusion behavior. For example, oocytes occupy an extremely soft mechanical regime, with reported moduli of only 50–100 Pa [238], so confinement during transport can be accommodated in part by particle deformation; as a result, diffusion through crowded or deformable polymer networks is governed not only by pore size, but also by the

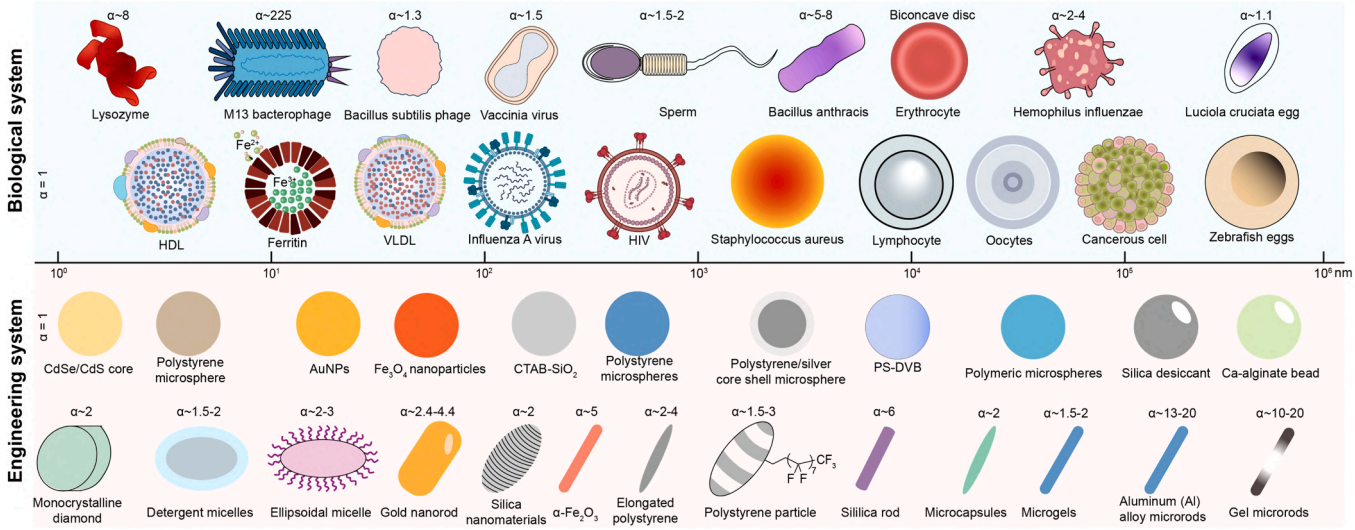


Fig. 6. Multi-scale overview of diffusing particles in polymer networks. Representative particles from biological and engineered systems are organized by characteristic size and annotated by aspect ratio (α) to highlight the wide ranges of length scales and shape anisotropy relevant to mechano-diffusion. Biological system (left-to-right, top row then bottom row): lysozyme [222]; M13 bacteriophage [223]; *Bacillus subtilis* phage [224]; vaccinia virus [225]; sperm [226]; *Bacillus anthracis* [227]; erythrocyte (biconcave disc) [228]; *Haemophilus influenzae* [229]; *Lucilia cruciata* egg [230]; HDL [231]; ferritin [232,233]; VLDL [231]; influenza A virus [234]; HIV [235]; *Staphylococcus aureus* [236]; lymphocyte [237]; oocytes [238]; cancerous cell [239]; zebrafish eggs [240]. Engineering system (left-to-right, top row then bottom row): CdSe/CdS core [241]; polystyrene microsphere [242]; AuNPs [243]; Fe_3O_4 nanoparticles [244]; CTAB–SiO_2 [245]; polystyrene microspheres [242]; polystyrene/silver core–shell microsphere [246]; PS–DVB [247]; polymeric microspheres [242]; silica desiccant [248]; Ca–alginate bead [249]; monocrystalline diamond [250]; detergent micelles [251]; ellipsoidal micelle [252]; gold nanorod; silica nanomaterials (EMSNs) [253]; α-Fe_2O_3 [254]; elongated polystyrene [255]; polystyrene particle [242]; silica rod; microcapsules [256]; microgels [257]; aluminum (Al) alloy microrods [258]; gel microrods [259].

Table 1
Spherical and ellipsoid particles in biological system.

Particle	Shape	Size, α	Modulus
Lipoprotein [260,261]	Spherical	Low-Density Lipoprotein over 20 nm, HDL 7–14 nm, VLDL	7.8 MPa for rat [231]
Exosome [262]	Spherical	50–200 nm [263] 30–150 nm [264]	Deformable [262] 5–15 MPa [265]
sFerritin	Spherical	12 nm [232,233]	250–800 MPa [266]
Poliovirus [267]	Spherical	30 nm [268]	/
HIV [235]	Spherical [269]	120 nm [270]	930–115 MPa [269]
Influenza A virus	Spherical [234]	100 nm [271]	0.05 nN/nm [234]
cancer cell	Spherical [239]	190–200 μm [239]	230–1250 Pa [239]
Staphylococcus aureus	Spherical [236]	0.5–1.5 μm [236]	0.35–2.3 MPa [272]
Lymphocyte [237]	Spherical	6.2–7.8 μm [237]	1.24 ± 0.09 kPa [273]
Oocytes [238]	Spherical	60 μm [238]	50–100 Pa [238]
Zebrafish eggs	Spherical	1–1.2 mm [240]	0.91±0.09 MPa [274]
Erythrocyte	Biconcave [228]	7.5–8.7 μm [228]	15–55 kPa [275]
Lysozyme	ellipsoid	1.8*9 nm, α = 5 [222]	/
M13 bacteriophage	Ellipsoid	6.6 nm*880 nm, α = 133 [276]	56 MPa [223]
Sperm	Ellipsoid	Oval-shaped head 3–5 μm in length and 2–3 μm in width, a midpiece (7–8 μm), and a tail (45 μm) [277]	0.9×10^{-21} N.m^2 (bending stiffness) [226]
Haemophilus influenzae	Ellipsoid	1*0.3 μm, α = 3.3 [278]	0.035 ± 0.015 N/m [229]
E-coli	Ellipsoid	α = 2–4 [279]	2–18 MPa [280]
Bacillus subtilis phage	Ellipsoid	54*42 nm, α = 1.28 [224]	1.8 GPa [224]
Vaccinia virus	Ellipsoid	300*200 nm, α = 1.5 [225]	/
Bacillus anthracis	Ellipsoid	1*5–8 μm, , α = 5-8 [227]	/
Luciola cruciate egg	Ellipsoid	0.55*0.5 mm, α = 1.1 [230]	/

Table 2
Spherical and ellipsoid particles in engineering system.

Particle	Shape	Size, α	Modulus
C_{70} molecule	Ellipsoid	0.78*0.694 nm, α = 1.12 [281]	1.9±0.1 GPa [282]
Monocrystalline diamond	Ellipsoid	6*3–5.4 nm, α = 2 [250]	1085–1189 GPa [283]
Detergent micelles	Ellipsoid	2.43 nm*1.61 nm, α = 1.5–2 [251]	/
α-Fe_2O_3 [254]	Ellipsoid	500 nm*120 nm, α = 5 [254]	236 GPa [284]
Elongated polystyrene [255]	Ellipsoid	692*325 nm−1078*270, α = 2–4 [255]	1.18 GPa [252]
Silica nanomaterials (EMSNs) [253]	Ellipsoid	150*80 nm, α = 2 [253]	26± GPa [285]
Microcapsules	Ellipsoid	~50 μm, α = 2–3 [256]	9 kPa [256]
microgels	Ellipsoid	400 μm,α = 1.5–2 [257]	
Gel microrods	Ellipsoid	0.05–0.3 mm *1–3 mm, α = 10–20, 6% [259]	4–13 kPa (10% w/v) [286]
aluminum (Al) alloy microrods	Ellipsoid	3 mm*150 μm−230μm,α = 13–20 [258]	/
AuNPs	Spherical	5 nm [243]	~100 GPa
CdSe core	Spherical	2.8–5.5 nm [241]	65–370 GPa [287]
Fe_3O_4 nanoparticles	Spherical	12 nm [244]	150–230 GPa [284]
polystyrene microspheres	Spherical	100–500 nm [242]	/
CTAC-SiO_2	Spherical	100–200 nm [245]	~73 GPa [288]
Polystyrene Microspheres	Spherical	800 nm [289]	2–8 GPa [290]
Polymeric Microspheres	Spherical	20 μm [291]	/
PS-DVB	Spherical	10 μm [247]	/
polystyrene/silver core–shell microsphere	Spherical	5.6 μm [246]	/
silica desiccant	Spherical	2–4 mm [248]	0.95 GPa [292]
Ca-alginate beads	Spherical	2.6–3 mm [249]	53.2–131 kPa [249]

ability of the particle to deform, redistribute contact stresses, and reduce the energetic penalty associated with crossing local constrictions. By contrast, AuNPs lie at the opposite end of the compliance spectrum, with a modulus of approximately 100 GPa, and therefore behave much more like rigid inclusions, for which diffusion is controlled primarily by geometric confinement and by the deformation capacity of the surrounding network rather than by deformation of the particle itself [243]. Taken together, these examples show that the broad compliance spectrum compiled in Tables 1,2 corresponds to fundamentally different modes of transport through polymer networks, ranging from compliance-assisted passage to geometry-dominated diffusion.

3.2.3. *Interactions*

Interfacial interactions provide an additional control variable for mechano-diffusion and are especially important in targeted delivery, selective sensing, and efficient separation. In the weak-interaction limit, transport is primarily obstruction-limited and can often be rationalized by particle size, aspect ratio (α), and compliance. When particles interact reversibly with the surrounding network, however, diffusion can become interaction-limited because migration is then coupled to repeated binding and debonding events.

The strength of such interactions is commonly represented in different ways in biological and engineering systems. In biological systems, it is often described by the equilibrium association constant K_{eq}, which quantifies the tendency of two binding partners to remain associated at equilibrium; larger K_{eq} therefore indicates stronger affinity and a greater likelihood of transient retention or recognition-mediated slowing during transport [293]. As summarized in Fig. 7**A** and Tables 3–6, biologically relevant interactions span a broad affinity hierarchy, progressing from monovalent biomolecular recognition to multivalent recognition, functional multimeric protein binding, and engineered high-affinity binding [294–307]. In engineering systems, by contrast, interaction strength is more naturally represented by the bond energy E_b, which describes the energetic required to break or rearrange a bond [308]. As summarized in Fig. 7**B** and Tables 7–9, these interactions can first be classified into permanent covalent bonds [309–314], dynamic covalent bonds [315–321], and non-covalent physical bonds [154,322–324], with each class occupying a different energetic regime and therefore imposing a different barrier to particle motion. Together, K_{eq} and E_b provide complementary ways to parameterize interaction-controlled diffusion: the former is especially useful for biological recognition, whereas the latter is more relevant to for engineered bonding motifs. In mechano-diffusion, these interactions are not merely chemical labels; they define an energetic and kinetic bottleneck that can couple directly to deformation when contact forces alter bond lifetime, rupture probability, or rebinding kinetics.

Taken together, Figs. 6, 7 and Tables 1–9 define a particle-centered design space for mechano-diffusion, organized by size, aspect ratio (α), compliance, and interaction strength/reversibility. Across this space, particle transport is shaped not by a single descriptor, but by the coupled effects of geometric restriction, mechanical accommodation, and interfacial binding within an evolving network microstructure. This framework provides a unified basis for linking particle properties to deformation-dependent diffusion behavior and will serve throughout the remainder of this review as the basis for formulating mechanistic principles for mechanically controlled transport and selectivity.

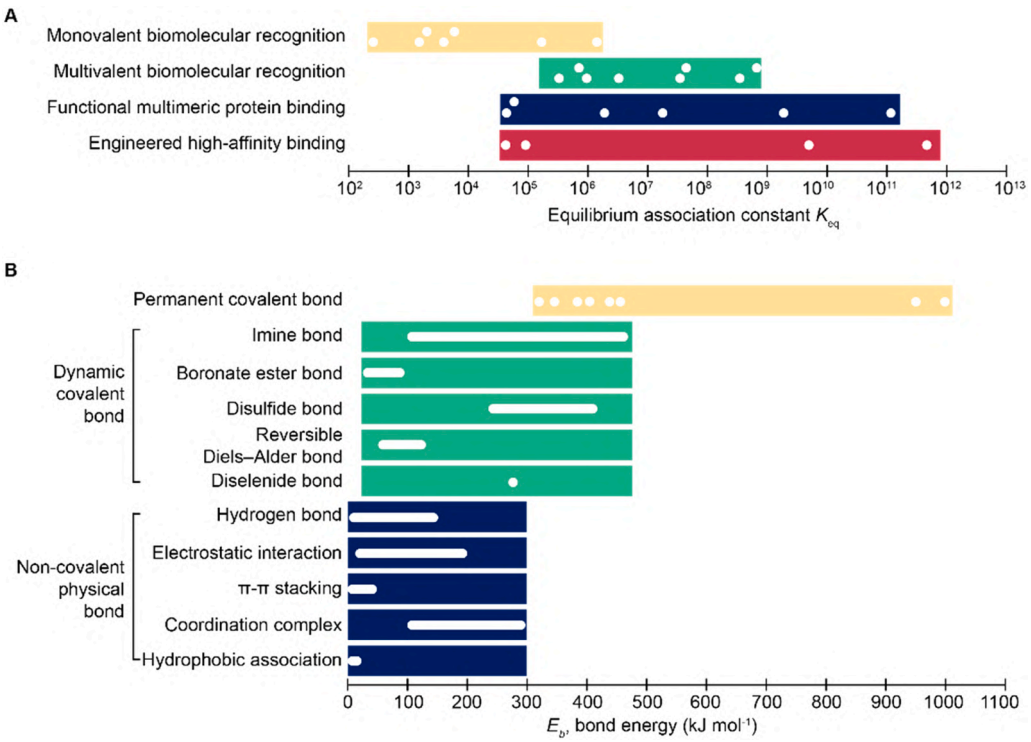


Fig. 7. Interaction strength governing particle–network binding in mechano-diffusion. (A) Representative ranges of equilibrium association constants K_{eq} for biomolecular interactions relevant to biological transport, spanning monovalent recognition, multivalent recognition, multimeric protein binding, and engineered high-affinity binding. (B) Representative bond energy ranges E_b for interactions commonly used in engineered systems, including permanent covalent bonds, dynamic covalent bonds, and non-covalent physical interactions. Together, K_{eq} and E_b provide complementary parameters of interaction strength that influence binding-mediated diffusion in polymer networks.

Table 3
Bio Monovalent biomolecular recognition.

Particle parts	K_d (M)	K_{eq} (M^{-1})
VCC β-prism – Me-α-mannose [294]	2.70×10^{-3}	3.7×10^2
VCC β-prism – Mannotriose [294]	2.29×10^{-3}	4.37×10^2
RbmC1 β-prism – Me-α-mannose [294]	5×10^{-4}	2×10^3
RbmC1 β-prism – Mannotriose [294]	5.88×10^{-7}	1.7×10^6
RbmC2 β-prism – Me-α-mannose [294]	1.79×10^{-4}	5.6×10^3
RbmC2 β-prism – GlcNAc-Man [294]	1.59×10^{-4}	6.3×10^3
RbmC2 β-prism – Mannotriose [294]	4.17×10^{-4}	2.4×10^3
Pin1 WW domain – Cdc25-derived phosphopeptide [295]	1.17×10^{-4}	8.55×10^3
Pin1 WW domain – tau phosphopeptide	2.30×10^{-4}	4.35×10^3
BCL2-C-Nt – L-Gal [295]	2.00×10^{-3}	5.0×10^2
BCL2-C-Nt – α-methyl-L-Fuc [296]	2.70×10^{-3}	3.7×10^2

Table 4
Bio Multivalent biomolecular recognition.

Particle parts	K_d (M)	K_{eq} (M^{-1})
VCC β-prism – NGA2 [294]	2.00×10^{-6}	5.0×10^5
VCC β-prism – NA2 [294]	1.00×10^{-6}	1.0×10^6
VCC β-prism – A2 [294]	1.10×10^{-6}	9.1×10^5
VCC β-prism – Asialofetuin [294]	2.00×10^{-6}	6.7×10^5
RbmC2 β-prism – Pentasaccharide [294]	2.00×10^{-6}	9.1×10^8
RbmC2 β-prism – NGA2 [294]	2.00×10^{-6}	6.7×10^8
RbmC2 β-prism – Asialofetuin [294]	2.00×10^{-6}	5.4×10^7
RbmC1 β-prism – Asialofetuin [294]	2.00×10^{-6}	6.3×10^7

Table 5
Bio Functional multimeric protein binding.

Particle parts	K_d (M)	K_{eq} (M^{-1})
BMP−2 – Noggin [297]	4.0×10^{-10}	2.5×10^9
LDL receptor ECD – PCSK9 [298]	1.0×10^{-9}	1.0×10^9
RhoGDI – prenylated RhoA·GDP [299]	5.0×10^{-12}	2.0×10^{11}
ZNRF1 RING domain – Ube2N [300]	5.0×10^{-8}	2.0×10^7
BAF [2] dimer – Emerin (LEM) [301]	5.88×10^{-7}	1.7×10^6
CAR D1 – CAR D1 [302]	1.6×10^{-5}	6.25×10^4
APEG−1 – APEG−1 [303]	2.0×10^{-5}	5.0×10^4

4. Diffusion in Undeformed Hydrogels

4.1. Effects of Mesh Size

Molecular diffusion and transport in polymer networks have been extensively investigated across a wide range of material systems, crosslinking strategies, and environmental conditions. Accordingly, diffusion behavior is commonly characterized by using quantitative transport metrics such as diffusivity, permeability, and release rates, which provide standardized measures for evaluating transport across diverse polymer matrices. This parameter-based perspective offers an effective means to compare transport efficiency under different conditions. At the same time, it naturally raises a complementary and more fundamental question: beyond variations in transport rates, through what mechanisms do molecules migrate within polymer networks?

To address this question, regardless of the specific polymer network architecture or diffusing particle properties, the relative size

Table 6
Bio Engineered high-affinity binding.

Particle parts	K_d (M)	K_{eq} (M^{-1})
DS4 – recombinant human DKK1 [304]	4.90×10^{-13}	2.04×10^{12}
ZHER2 affibody – HER2 extracellular domain [305]	2.20×10^{-11}	4.55×10^{10}
Api88 (designer peptide) – DnaK [306]	5.0×10^{-6}	2.0×10^{5}
SARS-CoV−2 Mpro – GC376 [307]	1.6×10^{-6}	6.25×10^{5}

Table 7
Permanent covalent bond.

Particle parts	Bond energy (kJ/mol)
Si-O	452 [309]
C-C	356 [309]
C-O	326 [309]
C-N	305 [310]
Si-N	439 [311]
Si-C	397 [312]
N≡N	945 [313]
C≡O	1072 [314]

Table 8
Dynamic covalent bond.

Particle parts	Bond energy (kJ/mol)
Imine bond	67–477 [315]
Boronate ester bond	27.2–93.3 [316]
Disulfide bond	240–425 [317,318]
Reversible Diels–Alder bond	37.6–130 [319,320]
Diselenide bond	280 [321]

Table 9
Non-covalent physical bond.

Particle parts	Bond energy (kJ/mol)
Hydrogen bond	0.8–167 [322,323]
Electrostatic interaction	5–200 [324]
Coordination complex	100–300 [324]
hydrophobic association	0–20 [154]
$\pi-\pi$ stacking	0–50 [154]

relationship between the particle and the characteristic mesh size of the network constitutes a general parameter for describing particle migration within polymer matrices. This size ratio provides a highly general and broadly applicable entry point for interpreting transport behavior across diverse systems. Within this framework, particle motion in undeformed polymer networks defines a baseline transport state, capturing the intrinsic migration modes permitted by the underlying geometric confinement and spatial connectivity. Establishing this baseline is a prerequisite for understanding how external stimuli mechanically modify effective accessibility of pathways within the network and, consequently, reshape particle trajectories and diffusion modes.

One conceptual understanding of particle diffusion in polymer networks can be established by considering the relative relationship between the characteristic mesh size (ξ) of the polymer network and the size of the diffusing particle (d) (Fig. 8). When the particle size is significantly larger than the average mesh size ($d >> \xi$), the particle is effectively confined within a local polymer cage formed by surrounding chains. Under this strong confinement, long-range migration is suppressed and particle migration is effectively arrested at the macroscopic scale. This immobilized state persists until the particle size approaches, or slightly exceeds, the polymer mesh size ($d \sim \xi$). In this intermediate regime, particle migration is commonly described as hopping diffusion, where transport occurs through activated transitions between neighboring cages [51]. To migrate from one cage to the next, the particle must overcome an energy barrier associated with deforming or rearranging the surrounding polymer chains. As a result, particle mobility in this regime is governed by polymer-mediated energetic constraints. With decreasing particle-to-mesh size ratio, the activation barrier is progressively reduced, leading to a rapid, nonlinear increase in effective diffusivity. Correspondingly, the diffusivity–size relationship in this regime exhibits a convex dependence.

As the particle size is further reduced and becomes smaller than the average mesh size ($d < \xi$), the diffusion mechanism gradually transitions from an energy-governed mechanism to one dominated by geometric constraints and spatial accessibility [325]. In this regime, particles can migrate along continuous pathways through the polymer matrix without the need to overcome significant activation barriers. Instead, diffusion is hindered primarily by steric obstruction and topological constraints imposed by the polymer chains, which act as obstacles that deflect particle trajectories upon collision. Despite these interactions, particle motion remains continuous. As particle size

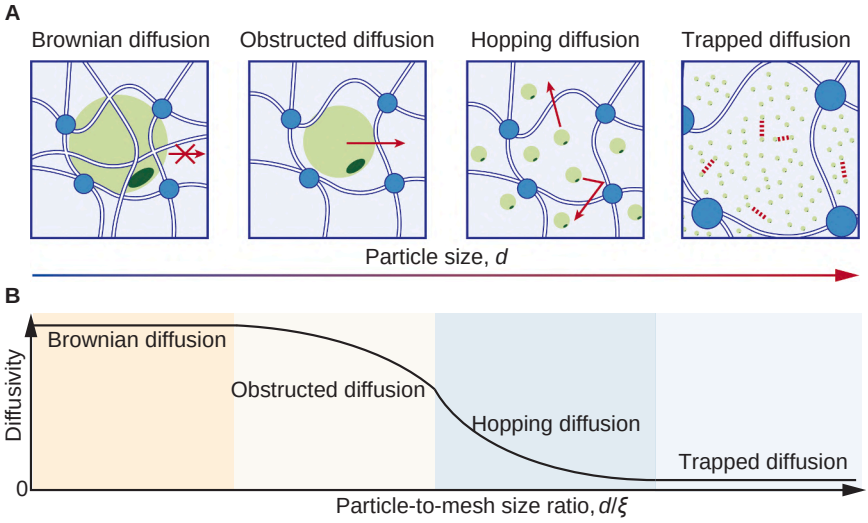


Fig. 8. Diffusion regimes governed by particle–network size relationships. Particle transport exhibits continuous changes in diffusivity but distinct diffusion behaviors as network accessibility increases, transitioning from immobilization and activated hopping to obstructed and Brownian diffusion. (A) Schematic illustrations of particles of different sizes diffusing within a polymer network. (B) Schematic illustration of diffusivity variation as a function of the particle-to-mesh size ratio.

decreases further ($d << \xi$), the frequency of particle–polymer collisions diminishes and boundary effects become less pronounced, resulting in a continued but more gradual increase in diffusivity [326]. In this geometry-dominated regime, the diffusivity–size relationship therefore becomes concave. In the limiting case where the particle size is much smaller than the characteristic mesh size, the polymer network becomes effectively transparent at the length scale relevant to particle motion. Under these conditions, the influence of the polymer matrix on diffusion is negligible, and particle diffusion is governed primarily by intermolecular interactions with the surrounding medium. Diffusion in this limit closely resembles Brownian diffusion in a homogeneous fluid and is largely independent of the polymer network architecture.

Taken together, particle diffusion in polymer networks can be understood as a regime-dependent process governed by the size relationship ratio between the diffusing particle and the network mesh. These baseline diffusion regimes in undeformed networks provide a necessary reference for understanding how external perturbations subsequently modify diffusion behavior.

4.2. Effects of Network Architecture

After accounting for the dominant effect of the particle-to-mesh size ratio (d/ξ), the influence of polymer network architecture on particle diffusion primarily arises from differences in structural homogeneity, topological constraints, chain dynamics, and the local energy landscape of the polymer networks. For example, in randomly crosslinked networks, the spatial distribution of crosslinking points exhibits statistical fluctuations, leading to broad distributions of strand length and local confinement. As a result, even when the average mesh size is comparable, diffusion pathways remain spatially heterogeneous, and particles experience different degrees of resistance in different regions. This heterogeneity can produce spatial variations in effective diffusivity and may lead to weakly diffusive behavior over certain time scales. In contrast, ideally ordered networks possess more uniform connectivity and narrower strand-length distributions, which significantly improves the statistical uniformity of diffusion pathways. Consequently, diffusion behavior in such systems generally agrees more closely with predictions from homogeneous network models and exhibits reduced temporal and spatial variability. Furthermore, in bottlebrush or highly branched networks, densely grafted side chains introduce strong steric repulsion that alters chain packing and reduces entanglement density. This structural feature increases the amplitude of thermal fluctuations within the network, thereby raising the probability of transient channel opening. As a result, even at comparable average mesh sizes, the effective free-energy barriers for particle migration may be lowered, leading to enhanced diffusion.

When polymer networks possess more complex structural hierarchy, diffusion behavior is often governed by multiscale network dynamics. For example, in interpenetrating-network polymers, differences in modulus, crosslink density, and relaxation time between constituent networks create spatial regions with distinct mechanical and dynamical properties. As particles migrate through such heterogeneous environments, they may experience alternating degrees of confinement, leading to segmented diffusion rates or the emergence of multiple characteristic time scales. A related effect is observed in slidable crosslink networks, where crosslinking points can move along polymer chains. This mobility enables local topological rearrangement when the network is perturbed, reducing local constraints and stress concentration. Therefore, particle diffusion becomes less sensitive to local deformation or disturbance, and diffusion behavior tends to be more stable compared with permanently crosslinked systems. In networks containing crystalline domains acting as physical crosslinks, diffusion is often influenced by phase structure. Crystalline regions function as rigid junctions that restrict chain mobility, yet they may partially melt or reorganize under changes in temperature or mechanical strain. Such structural transitions can generate diffusion pathways that open or close over time or space, resulting in diffusion behavior that is strongly coupled to phase evolution and often exhibits gated or stimulus-responsive characteristics. Furthermore, in dynamic-bond networks, where crosslinks have finite lifetimes, the network topology continuously evolves through bond exchange or reversible association. Particle diffusion therefore becomes coupled to the characteristic time scales of bond exchange or network relaxation. When the network rearrangement rate approaches or exceeds the particle diffusion time scale, newly accessible pathways are continually generated, and diffusion may display pronounced time dependence. Finally, in hybrid crosslinked networks, permanent covalent crosslinks coexist with reversible or physical junctions, giving rise to multiple relaxation time scales. This multiscale dynamics allow diffusion to be governed simultaneously by long-term structural constraints and short-term local rearrangements, often producing multistage or time-dependent diffusion behavior.

Overall, when particle size and the average polymer mesh size are effectively fixed, the influence of polymer network architecture on diffusion primarily originates from how network topology and chain dynamics modify the spatial heterogeneity, topological constraints, and characteristic relaxation times experienced by diffusing species. This implies that diffusion in polymer networks is governed not only by static geometric structure, but also by the hierarchical organization of the network and its rearrangement dynamics, which together determine the diffusion mode and its time-dependent behavior.

5. Mechano-Diffusion in Deformed Hydrogels under Static Loading

5.1. Isotropic Particles at Different Stress States

Section 4 established the undeformed-network baseline in which particle diffusion is primarily organized by the relative size ratio between the particle diameter d and the characteristic mesh size ξ. Classical diffusion models, including the Stokes–Einstein relation, obstruction-based models, and hopping-based models, provide useful baseline descriptions for different particle-to-mesh size regimes in undeformed polymer networks. However, these models are generally formulated for undeformed or statistically stationary networks, in which parameters such as mesh size, obstruction factor, hopping barrier, and network relaxation time are treated as fixed or equilibrium quantities.

Under static mechanical loading, this baseline is modified because deformation changes both the geometry of the local diffusion pathway and the elastic state of the surrounding polymer chains. In mechano-diffusion, quantities that are fixed in classical models become coupled to the mechanical state of the network. Static loading can alter local mesh geometry, polymer-cage shape, chain stretch, and elastic energy barriers, while anisotropic loading can further introduce direction-dependent transport pathways. Therefore, the central question is no longer only whether a particle is smaller or larger than the undeformed mesh size, but how the applied deformation transforms the accessible opening, the local cage geometry, and the energetic barrier that the particle must overcome during transport. Classical models should therefore be viewed as limiting descriptions that must be extended through deformation-dependent geometric and energetic terms.

When the particle size is much smaller than the mesh size ($d \ll \xi$), the particle experiences negligible confinement from the polymer network. In this limit, the network imposes minimal resistance to particle motion, and the particle undergoes Brownian diffusion similar to that in a pure solvent. The diffusion coefficient therefore follows the classical Stokes-Einstein relation [326,327],

$$D = \frac{k_B T}{3\pi\eta d} \tag{1}$$

where D is the diffusion coefficient, k_B is the Boltzmann constant, T is the absolute temperature, and η is the dynamic viscosity of the surrounding

fluid. It should be emphasized that the Stokes–Einstein relation represents an idealized limiting case rather than a general description of particle diffusion in polymer networks. This relation assumes that the surrounding medium behaves as a homogeneous continuum fluid characterized by a single effective viscosity, and that the diffusing particle experiences negligible steric confinement or specific interactions with the medium. These assumptions are reasonable for sufficiently small particles in dilute liquids or weakly confining networks, but they become increasingly invalid in hydrogels and polymer matrices, where finite mesh size, spatial heterogeneity, polymer-chain fluctuations, and polymer–particle interactions can strongly influence particle transport.

In polymer networks, the diffusing particle migrates through a heterogeneous environment formed by polymer chains, crosslinks, entanglements, and transient free-volume fluctuations. When the particle size approaches the characteristic mesh size, the particle no longer samples the medium as a uniform continuum. Instead, its motion becomes sensitive to local pore geometry, steric obstruction by polymer strands, polymer-chain fluctuations, and possible polymer–particle interactions. Therefore, the diffusivity may deviate substantially from the Stokes–Einstein prediction and can no longer be described solely by hydrodynamic drag in an effective viscous medium. In this sense, the Stokes–Einstein relation should be regarded as the small-particle, weak-confinement limit of a broader diffusion framework in polymer networks.

For particles in the obstruction-dominated regime, the undeformed mesh size in the obstruction model can be replaced by the deformation-dependent effective opening,

$$\frac{D}{D_{\mathrm{liq}}} = \exp\left[-\frac{\pi}{4}\left(\frac{d}{\xi_{\mathrm{eff}}}\right)^2\right] \tag{2}$$

where D_{liq} is the particle diffusivity in the pure liquid phase. Here, ξ_{eff} is defined as the diameter of the inscribed circle of the local cage, denoting the characteristic opening of the deformed polymer cage along the relevant diffusion direction. Because static loading generally deforms the network anisotropically, ξ_{eff} can be direction-dependent, leading to anisotropic obstruction even for isotropic particles.

When the particle size becomes comparable to the mesh size ($d \sim \xi$), diffusion can no longer be described solely by geometric obstruction. To pass through the network, the particle must locally deform the surrounding polymer cage, and diffusion becomes a thermally activated hopping process [51,328–331]. As schematically illustrated in Fig. 9**A**, the particle resides transiently in a cage formed by neighboring polymer chains and escapes from one cage to another through activated events [54,332,333]. During a hopping event, the particle must squeeze through a local opening in the surrounding polymer cage [334]. This process requires temporary displacement and stretching of the enclosing polymer chains. In the undeformed state, the cage may be idealized as a nearly symmetric polygonal structure, whereas under deformation it becomes distorted and direction-dependent. In both cases, ξ_{eff} characterizes the effective pore size available for particle diffusion and therefore serves as the relevant geometric descriptor for diffusion through a deformed cage. As the particle passes through the cage, the surrounding chains are stretched relative to their initial configurations, giving rise to an increase in the elastic free energy of the network. This free energy increase defines the energy barrier associated with hopping. For particles with sizes comparable to the mesh size, the energy barrier scales approximately as [51,54,329,330,333,335]

$$\frac{U}{k_B T} \cong \left(\frac{d}{\xi}\right)^2 \tag{3}$$

Accordingly, hopping diffusion is an activated process, and the corresponding diffusivity depends exponentially on the energy barrier height [51,330],

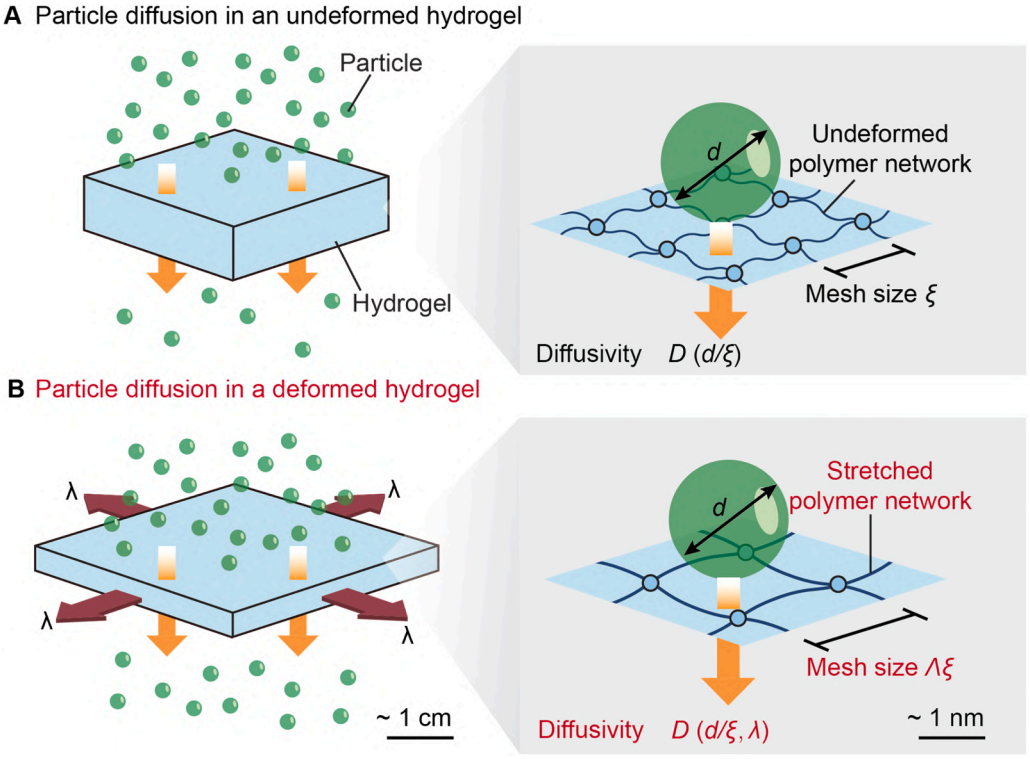


Fig. 9. Schematic illustration of particle diffusion in undeformed and deformed polymer networks. (A) Diffusion in an undeformed hydrogel. The particle of diameter d migrates through cages formed by surrounding polymer chains with characteristic mesh size ξ, giving a diffusivity $D(d/\xi)$. (B) Diffusion in a mechanically deformed hydrogel. Network stretching modifies the local cage geometry and increases the effective mesh size to $\Lambda\xi$, thereby altering the available diffusion opening and the resulting diffusivity $D(d/\xi, \lambda)$. These schematics illustrate how deformation modifies the geometric confinement governing particle transport in polymer networks.

$$D_0 \cong \frac{\xi_c^2}{\tau_r}\left(\sqrt{\frac{U}{k_B T}}\right)^{-1} \exp\left(-\frac{U}{k_B T}\right) \tag{4}$$

where ξ_c is the correlation length and τ_r is the characteristic relaxation time of the polymer network. Because the hopping barrier originates from elastic deformation of the surrounding network chains, its magnitude depends directly on the constitutive response of the polymer network. Different network architectures and constitutive models therefore lead to different energetic penalties for cage deformation, and consequently to different hopping barriers and diffusivities.

Under static mechanical loading, deformation of the hydrogel modifies both the geometry of the local polymer cage and the energetic state of the surrounding chains. As schematically illustrated in Fig. 9**B**, the resulting change in diffusivity can be understood through two coupled mechanisms: geometric modulation and energy modulation. Geometric modulation arises because deformation changes the size and shape of the local diffusion opening; energy modulation arises because deformation alters the chain stretch state before and during particle diffusion, thereby modifying the hopping barrier.

For particles in the obstruction-dominated regime ($d < \xi$), the diffusivity in the deformed hydrogel can be described by replacing the undeformed mesh size with the effective local opening ξ_{eff},

$$\frac{D}{D_{\text{liq}}} = \exp\left[-\frac{\pi}{4}\left(\frac{d}{\xi_{\text{eff}}}\right)^2\right] \tag{5}$$

Because deformation is generally anisotropic, ξ_{eff} may depend on the direction of particle diffusion. For particles in the hopping-dominated regime ($d \sim \xi$), the diffusivity in the deformed hydrogel, normalized by that in the undeformed state, is expressed as

$$\frac{D}{D_0} = \sqrt{\frac{U_0}{U}} \exp\left(\frac{U_0 - U}{k_B T}\right) \tag{6}$$

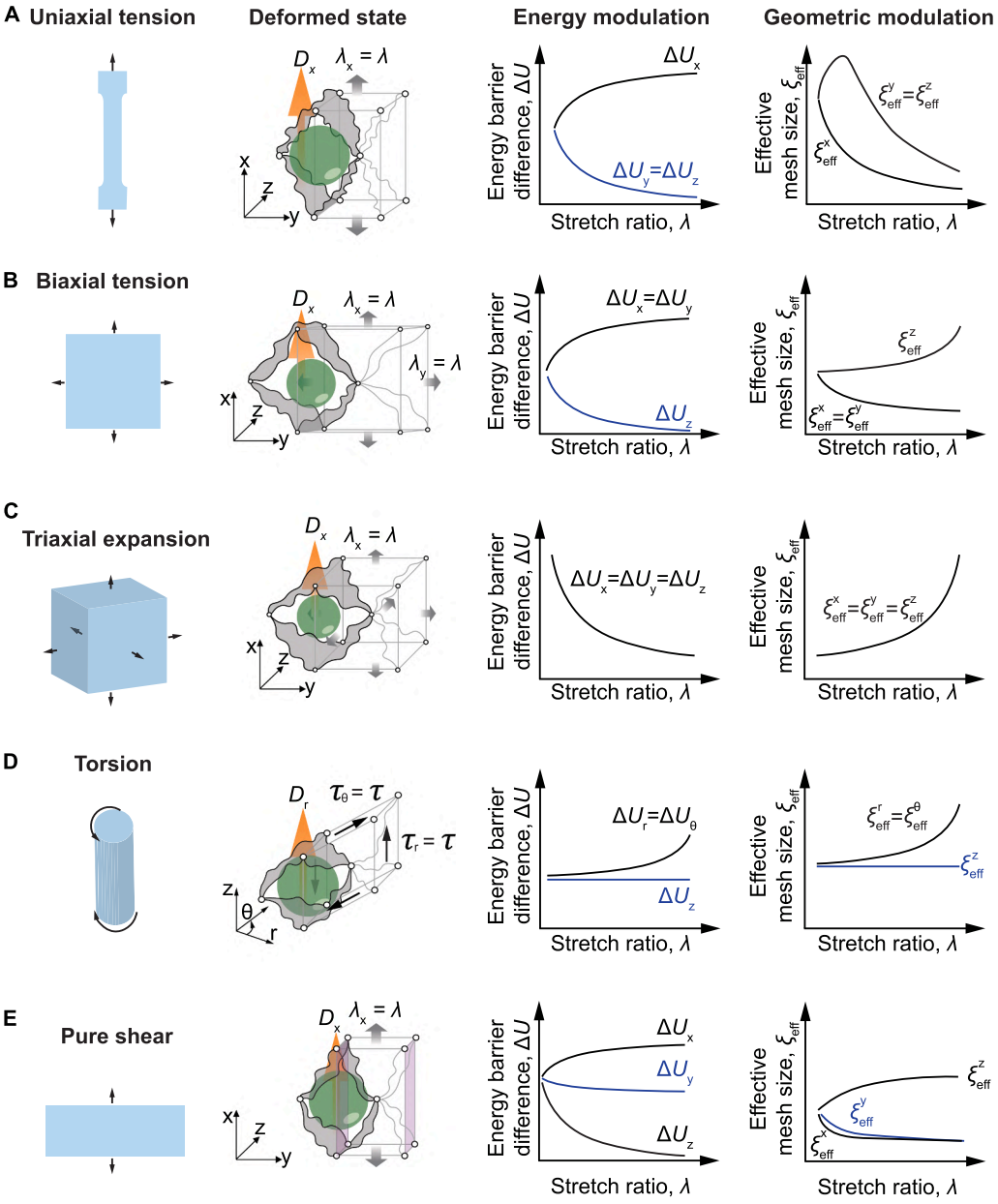


Fig. 10. Effect of different deformation modes on hopping diffusion in polymer networks. (A) Uniaxial tension, (B) biaxial tension, (C) triaxial extension, (D) torsion, and (E) pure shear. Deformation alters both the hopping energy barrier ΔU and the effective mesh size ξ_{eff}, leading to strain-induced modulation of particle diffusivity through coupled energetic and geometric effects.

where U_0 is the hopping barrier in the undeformed hydrogel and U is the hopping barrier in the deformed hydrogel. Mechanical deformation may reduce the free energy increment required for particle diffusion and thus lower the hopping barrier ($U < U_0$). Quantitatively, the energy barrier is determined by the free energy difference between the chain state before particle diffusion and the more stretched state during particle diffusion, which can be evaluated using the constitutive free energy function of the network,

$$U_0 = W(\Lambda_H^0) - W(\Lambda_L^0) \tag{7}$$

$$U = W(\Lambda_H) - W(\Lambda_L) \tag{8}$$

where Λ_L^0 and Λ_H^0 denote, respectively, the chain stretch ratios before and during particle diffusion in the undeformed hydrogel, while Λ_L and Λ_H denote the corresponding chain stretch ratios in the deformed hydrogel. Here, W is the free energy function of the polymer network. In the following, several common deformation modes of hydrogels are analyzed as representative examples to illustrate how static loading regulates isotropic particle diffusion.

Under uniaxial tension, the polymer network is stretched along the loading direction x with $\lambda_x = \lambda$ and contracts in the transverse directions y and z (Fig. 10**A**), so that the polymer cage is deformed anisotropically [54,243]. This deformation renders the hopping response direction-dependent: the energy barrier difference $\Delta U = U_0 - U$, i.e., ΔU_x, ΔU_y, and ΔU_z all decrease with increasing stretch ratio, but with $\Delta U_x > \Delta U_y = \Delta U_z$, while the effective mesh size exhibits the opposite trend distinction, with ξ_{eff}^x decreasing monotonically and $\xi_{\text{eff}}^y = \xi_{\text{eff}}^z$ varying non-monotonically. Because energetic modulation and geometric modulation act in opposite ways along different directions, their combined effect on particle diffusivity can be competing: the reduction of the energy barrier tends to enhance diffusion, whereas the simultaneous decrease of the effective diffusion opening when the particle diffuses perpendicularly to the stretching direction suppresses it. Consequently, particle diffusivity under uniaxial tension exhibits a direction-dependent response to stretch. Diffusion parallel to the loading direction decreases monotonically with the increasing stretch ratio because the Poisson effect reduces the effective mesh size of the polymer cage along the loading direction, whereas diffusion perpendicular to the loading direction shows a non-monotonic dependence on stretch ratio arising from the competing geometric confinement and energetic barriers governing the hopping process. The combined energetic and geometric anisotropy therefore leads to anisotropic hopping diffusion under uniaxial tension.

Under biaxial tension, the polymer network is stretched equally along the x-and y-directions with $\lambda_x = \lambda_y = \lambda$ and contracts along the transverse z-direction (Fig. 10**B**), so that the polymer cage is deformed anisotropically [243]. This deformation renders the hopping response direction-dependent: $\Delta U_x = \Delta U_y$ increase but ΔU_z decreases with increasing stretch ratio which is $\Delta U_x = \Delta U_y < \Delta U_z$, while $\xi_{\text{eff}}^x = \xi_{\text{eff}}^y$ decrease and ξ_{eff}^z increases with stretch. Similar to uniaxial tension, particle diffusivity is regulated through coupled energetic and geometric modulation. However, because stretching occurs simultaneously in two orthogonal directions, the decrease in the energy barrier and the change in the effective mesh size are both amplified. Consequently, the tuning ratio of particle diffusivity under biaxial tension is generally larger than that under uniaxial tension.

Under triaxial extension, the polymer network is stretched equally along all three spatial directions, so that $\lambda_x = \lambda_y = \lambda_z = \lambda$ (Fig. 10**C**), and the polymer cage expands isotropically. As a result, both the energy barrier and the effective mesh size lose their directional distinction: $\Delta U_x = \Delta U_y = \Delta U_z$ decreases monotonically with increasing stretch ratio, whereas $\xi_{\text{eff}}^x = \xi_{\text{eff}}^y = \xi_{\text{eff}}^z$ increases monotonically. The resulting energetic and geometric isotropy gives rise to isotropic particle diffusion under triaxial extension. Such triaxial extension represents an isotropic volumetric deformation equivalent to hydrostatic conditions [336]. In classical poroelastic descriptions under hydrostatic conditions, particle diffusivity is typically treated as a constant material parameter, with diffusion driven by pressure gradients. However, the present framework indicates that even under isotropic deformation the particle diffusivity is not strictly constant. Because both the energy barrier and the effective mesh size evolve with volumetric deformation, the particle diffusivity becomes a function of the stretch ratio. Consequently, hydrostatic deformation can regulate particle diffusion through deformation-dependent energetic and geometric modulation of the polymer cage.

Under torsion, the polymer network is subjected to shear deformation in the circumferential and radial directions, as indicated by $\tau_\theta = \tau$ and $\tau_r = \tau$ in Fig. 10**D**, so that the polymer cage is distorted in the $r\theta$ -plane while remaining unchanged along the z-direction [337]. This directional asymmetry is reflected in both the energetic and geometric responses. The hopping energy barriers in the radial and circumferential directions remain identical and increase with increasing torsion, $\Delta U_r = \Delta U_\theta$, whereas the energy barrier along the axial direction remains constant, ΔU_z. The geometric modulation differs from stretch-dominated deformations because torsion corresponds to a volume-preserving shear. At small torsion, the effective mesh size in the $r\theta$ -plane remains nearly unchanged, whereas at larger torsion the polymer cage becomes increasingly skewed and the local diffusion opening decreases, leading to a reduction of the effective mesh size. Torsion therefore induces anisotropic hopping diffusion through shear-driven distortion of the polymer cage. Because torsion preserves volume but breaks the geometric symmetry of the network, particle diffusion becomes direction-dependent even without volumetric deformation. Diffusion is primarily modulated within the $r\theta$ -plane, while the z-direction remains comparatively unaffected.

Under pure shear, the polymer network is stretched along the x-direction with $\lambda_x = \lambda$, while the y-direction remains unchanged and the thickness direction contracts correspondingly (Fig. 10**E**), thereby imposing an anisotropic deformation on the polymer cage. The resulting hopping diffusion is strongly direction-dependent. ΔUx increases because the particle needs to overcome higher energy barrier to enlarge the polymer cage and achieve one hopping diffusion step. Although ΔU_y and ΔU_z, decrease with increasing stretch ratio ΔU_x increases and they remain ordered as $\Delta U_z < \Delta U_y < \Delta U_x$. Meanwhile, the effective mesh sizes evolve differently along the three directions: ξ_{eff}^z increases, ξ_{eff}^y decreases, and ξ_{eff}^x remains small and decreases slightly. These distinct evolutions of the energy barrier and the effective mesh size jointly regulate anisotropic hopping diffusion. The combined energetic and geometric anisotropy therefore gives rise to anisotropic hopping diffusion under pure shear. In contrast to torsion, which corresponds to simple shear and primarily skews the polymer cage without directional stretch, pure shear deforms the polymer cage through directional stretching and compression. As a result, the diffusion pathways are not only distorted but also expanded or contracted along different principal directions, leading to a diffusion behavior that differs fundamentally from that induced by simple shear.

Across these deformation states, hopping diffusion is jointly regulated by energy modulation and geometric modulation. Energy modulation arises from deformation-induced changes in the elastic free energy of polymer chains during particle hopping, which determine the directional hopping energy barriers. Geometric modulation arises from deformation-induced changes in the effective mesh size ξ_{eff} of the polymer cage, which likewise become direction-dependent under different deformation states. The coupling of these two mechanisms determines the directional hopping diffusivity in deformed polymer networks under static loading. In addition, particle diffusion in polymer networks may undergo a transition between different diffusion regimes depending on the ratio between particle size d and mesh size ξ_{eff}. When $d < \xi_{\text{eff}}$, diffusion is characterized by obstruction model, whereas when

$d \sim \xi_{\text{eff}}$, diffusion becomes dominated by hopping diffusion. The mesh size ξ_{eff} is governed by the deformation gradient **F**. Through the resulting change in the ratio d/ξ_{eff}, mechanical loading can shift particle diffusion between obstruction-dominated and hopping-dominated regimes.

5.2. Distinct Diffusion Characteristics of Isotropic and Anisotropic Particles in Polymer Networks

Unlike isotropic particles, anisotropic particles possess an additional orientational degree of freedom that directly couples to the deformation-induced anisotropy of the surrounding polymer cage. Therefore, under static loading, their diffusion cannot be described by translational motion alone. Instead, particle transport must be characterized by the coupled evolution of position and orientation, because deformation can simultaneously bias particle alignment, alter rotational mobility, and generate direction-dependent translational diffusivity.

Rotational diffusion plays distinct roles in isotropic and anisotropic particles, as illustrated in Fig. 11**A**. For isotropic particles, rotational diffusion does not alter particle configuration. For anisotropic particles, by contrast, rotational diffusion changes particle orientation and therefore becomes an essential component of diffusion. This difference further leads to distinct directional characteristics during translational diffusion, as shown in Fig. 11**B**. In undeformed and statistically homogeneous polymer networks, isotropic particles diffuse without directional preference. Anisotropic particles, however, exhibit direction-dependent diffusion because their geometric asymmetry gives rise to different diffusional resistances parallel and perpendicular to the major axis [338,339]. As a result, anisotropic particles possess an intrinsic directional preference even in the absence of network deformation.

Diffusion of anisotropic particles must be described by both translational and rotational diffusivities, as illustrated in Fig. 11**C**. Translational diffusion is described by the displacement vector $\Delta \boldsymbol{r}(t)$, defined as the vector from the initial particle position to its position at time t. Rotational diffusion is described by the angular displacement $\Delta\theta(t) = \theta(t) - \theta(0)$, where $\theta(t)$ is the angle between the major axis and the x-axis at time t. Since both particle position and orientation evolve during diffusion, $\Delta \boldsymbol{r}(t)$ and $\Delta\theta(t)$ must be considered simultaneously. Their statistical quantification is summarized in Fig. 11**D**. The translational diffusivity is obtained from the mean-squared displacement (MSD) [339,340]:

$$D_t = \frac{1}{4}\frac{d}{dt}\langle |\Delta \boldsymbol{r}(t)|^2 \rangle \tag{9}$$

$$\langle |\Delta \boldsymbol{r}(t)|^2 \rangle = \frac{1}{N}\sum_{i=1}^{N} |\Delta \boldsymbol{r}_i(t)|^2 = \frac{1}{N}\sum_{i=1}^{N} \left[(x_i(t) - x_i(0))^2 + (y_i(t) - y_i(0))^2 \right] \tag{10}$$

where N is the number of particles (or independent trajectories) used for statistical averaging, $\boldsymbol{r}_i(t) = (x_i(t), y_i(t))$ denotes the position vector of particle i at diffusion step t, and $\boldsymbol{r}_i(0)$ is its initial position.

Rotational diffusion is characterized by the mean-squared angular displacement $\langle [\theta(t) - \theta(0)]^2 \rangle$, from which the rotational diffusivity is obtained as

$$D_r = \frac{1}{2}\frac{d}{dt}\langle [\theta(t) - \theta(0)]^2 \rangle \tag{11}$$

where $\langle [\theta(t) - \theta(0)]^2 \rangle$ is defined as

$$\langle [\theta(t) - \theta(0)]^2 \rangle = \frac{1}{N}\sum_{i=1}^{N} \left[(\theta_i(t) - \theta_i(0))^2 \right] \tag{12}$$

where $\theta_i(t)$ is the orientation angle between the major axis of particle i and the x-axis in the global coordinate system, and $\theta_i(0)$ is its initial orientation angle. Accordingly, translational diffusivity is determined from the time dependence of the mean-squared displacement, whereas rotational diffusivity is determined from that of the mean-squared angular displacement. For isotropic particles, diffusion is adequately characterized by D_t alone. For anisotropic particles, both D_t and D_r are required.

5.3. Anisotropic Particles: Single-Particle versus Multi-Particle Diffusion

Diffusion of anisotropic particles under static loading is governed by the coupled evolution of particle translation, particle orientation, and deformation-induced anisotropy of the surrounding polymer cage [339,341]. Unlike isotropic particles, whose diffusion can be described solely by translational motion, anisotropic particles possess an orientational degree of freedom that directly affects their diffusion behavior. Consequently, static deformation influences anisotropic particle diffusion not only by modifying the geometry of the local diffusion pathway, but also by biasing particle orientation toward energetically favored states [342].

For a single anisotropic particle, translational motion and rotational motion already coexist even in the undeformed state. As illustrated in Fig. 12**A**, in the absence of external loading, the particle diffuses within the surrounding polymer cage through displacement of its geometric

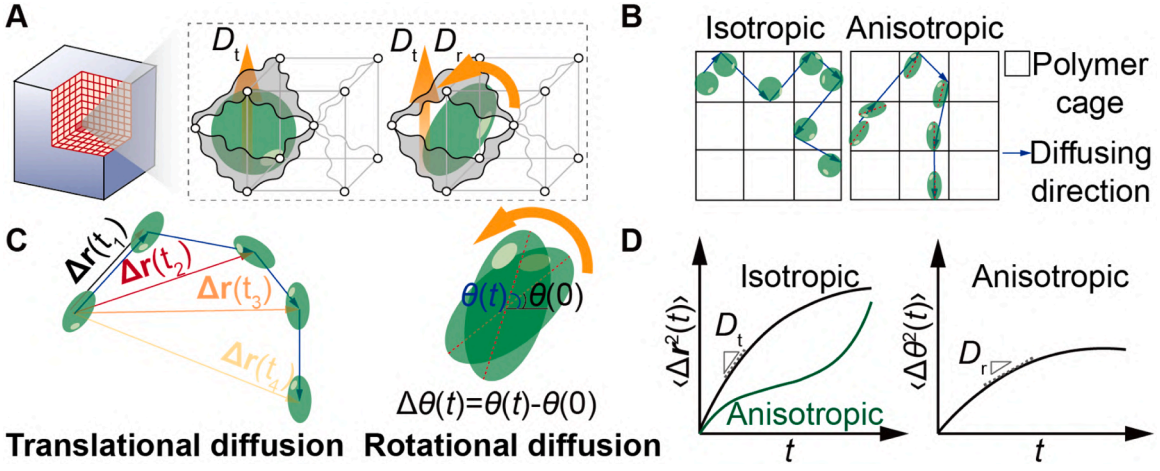


Fig. 11. Translational and rotational diffusion of anisotropic particles in polymer networks. (A) Isotropic vs anisotropic particles. (B) Direction-dependent translational diffusion. (C) Translational displacement $\Delta \boldsymbol{r}(t)$and angular displacement $\Delta\theta(t)$. (D) Mean-squared displacement and mean-squared angular displacement used to determine $D_t$and D_r.

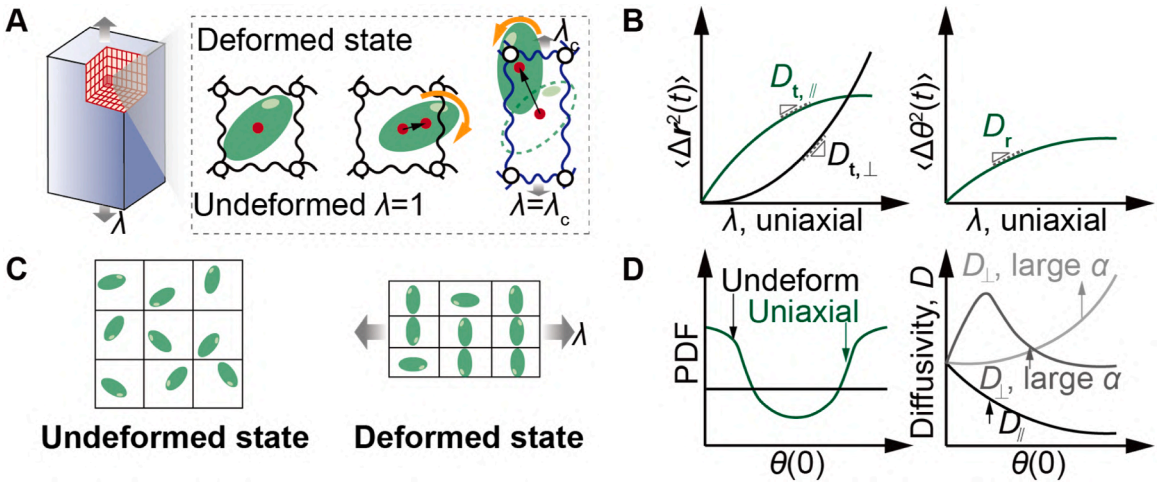


Fig. 12. Coupled translational, rotational, and orientational statistics of anisotropic particles under mechanical loading. (A) Translational and rotational diffusion of a single anisotropic particle within a polymer cage and deformation-induced reorientation under uniaxial tension. (B) Directional components of translational diffusivity parallel and perpendicular to the loading direction. (C) Reorientation of multiple anisotropic particles from random orientation in the undeformed state to alignment under deformation. (D) Orientation-dependent probability density and corresponding diffusivity components $D_{\parallel}$ and $D_{\perp}$, illustrating the combined effects of particle orientation and aspect ratio α on anisotropic diffusion.

center together with continuous change of its orientation. Here, the red point denotes the geometric center of the particle, while the curved arrow indicates particle rotation. Although the undeformed polymer network is statistically isotropic, the particle orientation remains an independent configurational variable. Therefore, diffusion of a single anisotropic particle cannot be described by translation alone, even before external deformation is applied.

Under static loading, this orientational degree of freedom gives rise to strain-induced reorientation. When the hydrogel is deformed, the local polymer cage becomes anisotropic, so that the energetic cost associated with diffusion depends on particle orientation relative to the loading direction. Under uniaxial tension, for example, the particle's major axis tends to rotate toward the tensile direction, as schematically shown in Fig. 12**A** for $\lambda = \lambda_c$. This reorientation reflects the tendency of the system to evolve toward the minimum-barrier configuration. Specifically, alignment of the particle's major axis with the loading direction minimizes the energy barrier that must be overcome during diffusion, because diffusion in this configuration minimizes the unfavorable deformation of the surrounding polymer cage. Thus, static deformation actively selects the preferred particle orientation rather than merely modifying the environment through which the particle diffuses.

This deformation-induced orientational bias is accompanied by anisotropy in translational diffusivity. As shown in Fig. 12**B**, the translational diffusivity of a single anisotropic particle under uniaxial loading must be resolved into the component parallel to the loading direction, $D_{t,\parallel}$, and the component perpendicular to the loading direction, $D_{t,\perp}$. These two components exhibit distinct dependencies on the applied stretch λ. The parallel component $D_{t,\parallel}$ increases with increasing λ, indicating that stretching facilitates particle diffusion along the tensile direction. By contrast, the perpendicular component $D_{t,\perp}$ evolves differently with λ, reflecting the fact that deformation of the polymer cage does not promote transverse motion to the same extent. Accordingly, static loading splits translational diffusivity into direction-dependent components and renders particle diffusion increasingly anisotropic as deformation grows.

For multiple anisotropic particles, static loading not only modifies the diffusivity of a single particle but also reshapes the orientational statistics of multiple anisotropic particles. In the undeformed state, the major axes of the particles are randomly distributed, with no preferred direction, as shown in Fig. 12**C**. Equivalently, the initial orientation angle $\theta(0)$, defined as the angle between the particle's major axis and the x-axis before diffusion, follows a uniform distribution. Once external loading is applied, however, the particles collectively reorient in response to the deformation-induced anisotropy of the network. Under uniaxial tension, their major axes progressively align with the loading direction, because this orientation corresponds to the lowest diffusion barrier. Therefore, deformation alters not only the diffusion of individual anisotropic particles, but also the orientational organization of the entire particle population.

This loading-induced orientational redistribution can be described quantitatively by an orientation-dependent probability density function. As shown in Fig. 12**D**, the probability density function is uniform with respect to $\theta(0)$ in the undeformed state, consistent with random orientation. Under uniaxial tension, however, the orientation probability density becomes a non-uniform function of $\theta(0)$. Assuming that the loading direction is along the x-axis, the probability density reaches its maxima near $\theta(0) = 0$ and $\theta(0) = \pi$, where the particle major axis is aligned with the tensile direction. These orientations are statistically favored because they correspond to the lowest diffusion barriers. In contrast, the probability density reaches its minimum near $\theta(0) = \pi/2$, where the particle is oriented perpendicular to the tensile direction and the barrier for diffusion is highest. More generally, different deformation modes generate different orientational energy landscapes and therefore different orientational probability distributions.

The translational diffusivity of multiple anisotropic particles is further governed by the combined effects of particle orientation and particle aspect ratio α, where α is defined as the ratio of the major to minor axis dimensions. As shown in Fig. 12**D**, the translational diffusivity can again be decomposed into the components parallel and perpendicular to the loading direction. The parallel component, $D_{\parallel}$, decreases monotonically with increasing $\theta(0)$, indicating that diffusion along the tensile direction is most favorable when the particle is initially aligned with that direction and becomes progressively less favorable as the particle rotates away from it. This trend holds irrespective of the particle aspect ratio α. By contrast, the perpendicular component, $D_{\perp}$, exhibits a more complex dependence on both $\theta(0)$ and α. For particles with low aspect ratio, $D_{\perp}$ decreases with increasing $\theta(0)$. For particles with high aspect ratio, however, $D_{\perp}$ first increases and then decreases with $\theta(0)$, giving rise to a non-monotonic dependence. This distinction indicates that transverse diffusion becomes increasingly sensitive to particle shape as particle anisotropy increases.

Taken together, anisotropic particle diffusion under static loading is regulated by the interplay among translation, orientation, and

deformation-induced anisotropy of the surrounding polymer network. For a single anisotropic particle, deformation changes the preferred particle orientation and resolves translational diffusivity into components parallel and perpendicular to the loading direction. For multiple anisotropic particles, deformation further redistributes particle orientations, leading to non-uniform orientational statistics and orientation-dependent diffusivity. Consequently, mechano-diffusion of anisotropic particles in deformed hydrogels must be understood as a coupled process involving particle shape, particle orientation, applied deformation, and the anisotropic energy landscape imposed by the polymer cage.

5.4. Role of Network Topology

Network topology is important in mechano-diffusion because diffusivity in polymer networks is governed not only by the instantaneous mesh size, but also by how the network deforms and reconfigures under load [151,152]. Different topologies generate different deformation fields, pore evolution pathways, and degrees of structural heterogeneity, so they do not produce the same deformation-dependent diffusivity even under comparable macroscopic strain [106,343,344]. For this reason, topology enters mechano-diffusion through the constitutive law: it determines how mechanical loading is translated into network reconfiguration, and thus how diffusivity evolves with deformation [149].

This topology dependence is less apparent in single-network systems with fixed covalent junctions, where the network is commonly treated within an affine hyperelastic framework. As shown in Table 10, ideal spring networks, such as tetra-arm PEG networks [167], are the simplest case and are often described by the Neo-Hookean model. Randomly crosslinked networks, including PAAm single-network hydrogels and GelMA hydrogels, remain within the same general constitutive picture, but their greater structural disorder usually requires more flexible phenomenological models, such as Neo-Hookean, Mooney–Rivlin, Gent, Ogden, and Arruda–Boyce formulations [345–349]. In diffusion problems, these networks provide a conceptually straightforward framework for relating deformation to diffusivity, because the diffusion pathways are often assumed to evolve approximately affinely with the bulk deformation.

This picture changes when network reconfiguration becomes non-affine. In entangled networks, such as high-molecular-weight PAAm [351] and ultra-high-molecular-weight PVA hydrogels, deformation is additionally constrained by chain entanglements, so the diffusion geometry cannot be inferred directly from the macroscopic deformation gradient [148]. Slip-link models are therefore more suitable than classical affine hyperelastic laws. A similar constitutive shift occurs in slide-ring networks, represented by polyrotaxane-based PEG hydrogels. These systems are also described by slip-link-type physical models, but for a different reason: the junctions are movable, so deformation is accompanied by junction redistribution [186,354]. In both cases, non-affine reconfiguration alters the local diffusion pathways in a manner that can significantly modify diffusivity relative to affine single-network predictions [151].

For networks with reversible connectivity, the coupling to diffusion becomes even stronger because the diffusion structure evolves not only with strain, but also with junction kinetics. In physically crosslinked networks, such as alginate–Ca^{2+} and gelatin hydrogels, constitutive behavior is commonly described using maxwell-type models [355], poro-viscoelastic models [356,366], or transient network theory [357]. Dynamic covalent networks, such as imine (Schiff-base) crosslinked hydrogels, are likewise often represented using maxwell-type viscoelastic formulations, since bond exchange permits network rearrangement during loading [358,361]. In these systems, diffusivity is affected not only by elastic pore distortion, but also by time-dependent bond dissociation, re-formation, or exchange, which continuously modifies the effective diffusion network.

A further level of complexity arises in multi-network systems. In hierarchical networks, such as alginate–gelatin composite hydrogels, the mechanics are often described using additive free energy models, reflecting contributions from multiple structural levels. In interpenetrating-network systems, especially DN hydrogels such as alginate–PAAm and PAMPS/PAAm, the response is commonly modeled using two-network formulations coupled with damage evolution [367]. For diffusion, these topologies are important because diffusion is then regulated by coupled reconfiguration of multiple subnetworks, and in DN systems potentially also by damage-induced changes in connectivity and confinement. Thus, the influence of topology on diffusivity becomes inseparable from how the constitutive model represents network interaction and structural evolution under load [368].

The significance of network topology in mechano-diffusion therefore lies in more than material classification. It defines the constitutive pathway by which deformation reshapes the diffusion landscape and thereby determines how diffusivity should be modeled in deformed polymer networks.

Regarding the sensitivity of the predicted transport behavior to network heterogeneity, hydrogels inherently exhibit spatial variations

Table 10
Network topologies and corresponding constitutive models.

Network topology			Constitutive model	Phenomenological/ physical model	Network reconfigurations
Single-network class	Ideal spring network	Tetra-arm PEG [167]	Neo-Hookean model [167]	Phenomenological	Affine
	Randomly crosslinked network	PAAm single-network hydrogel GelMA hydrogel	Neo-Hookean model [345] Mooney–Rivlin model [346] Gent model [348] Ogden model [349] Arruda–Boyce model [350]	Phenomenological	Affine
	Entangled network	High–Mw PAAm hydrogel [351] Ultra-high molecular weight PVA hydrogel [353]	Slip-link model [352,353]	Physical	Non-affine
	Slide-ring network	Polyrotaxane-based PEG hydrogel [186,354]	Slip-link model [186,354]	Physical	Non-affine
	Physically crosslinked network	Alginate–Ca^{2+} hydrogel [355] Gelatin hydrogel [357]	Maxwell-type [355] poro-viscoelastic model [356] Transient network theory [357]	Physical & phenomenological	Non-affine
	Dynamic covalent network	Imine (Schiff-base) crosslinked hydrogel [358,359]	Maxwell model&viscoelasticity [358]	Phenomenological & physical	Non-affine
Multi-network class	Hierarchical network [360]	Alginate–gelatin composite hydrogel [361]	Additive free-energy models [362]	Phenomenological	Non-affine
	Interpenetrating network (IPN) [44]	Alginate–PAAm DN hydrogel [363] PAMPS / PAAm DN hydrogel [365]	Two-network + damage evolution models [364]	Phenomenological	Non-affine

in mesh size, and using a single mean mesh size therefore represents an idealization [340,369]. Nevertheless, moderate heterogeneity is expected to primarily smooth and broaden quantitative variations, rather than eliminate the underlying transition between diffusion regimes. As the transition is governed by the relative size ratio between the particle and the characteristic network scale, its physical origin remains unchanged, although heterogeneity may affect the sharpness and effective location of the transition. In addition, viscoelastic relaxation may further reduce the effective hopping energy barrier relative to purely elastic predictions. Thus, the mean mesh size approximation captures the dominant features of the regime transition, while more detailed heterogeneous or time-dependent models may refine quantitative predictions [370,371].

Taken together, the above discussion illustrates that classical diffusion models remain useful as baseline descriptions for mechano-diffusion, while also clarifying where additional considerations are needed for deformed hydrogels. The Stokes–Einstein relation captures the weak-confinement limit, obstruction-based models describe geometric restriction by polymer meshes, and hopping-based models account for activated transport through transient network openings. These models provide important physical insights into how particle size, mesh size, and network constraints regulate diffusion in polymer networks. At the same time, mechano-diffusion introduces coupling between particle transport and network deformation that is not fully represented in these classical descriptions in their original forms. In many models, structural and transport parameters such as mesh size, obstruction factor, hopping barrier, and network relaxation time are treated as fixed, equilibrium, or statistically stationary quantities. In mechanically deformed hydrogels, these parameters may become deformation-dependent and direction-dependent because loading alters local mesh geometry, polymer-cage shape, chain stretch, accessible free volume, elastic energy barriers, relaxation dynamics, and particle orientation distributions. Therefore, mechano-diffusion should not be viewed simply as a direct substitution of deformed geometric parameters into classical diffusion models, but rather as a coupled transport–mechanics problem in which particle mobility and network deformation are mutually linked.

6. Mechano-diffusion in Deformed Hydrogels under Dynamic Loading

Section 5 focused on particle diffusion in polymer networks under static loading, where mechanical deformation regulates diffusion through geometric modulation of the local diffusion opening and energetic modulation of the hopping energy barrier [347]. In many practical systems, however, hydrogels are subjected to time-dependent mechanical loading, such as cyclic deformation, oscillatory strain, and acoustic excitation [372–374]. Under these conditions, the polymer network no longer remains in a time-independent deformed configuration. Instead, chain configuration, cage geometry, and diffusion pathways evolve continuously in time [375]. Particle diffusion is therefore governed not only by strain-induced geometry and energy, but also by the competition among characteristic time scales associated with mechanical loading, polymer relaxation, and hopping dynamics [328,329,331].

6.1. Time Scales Governing Mechano-Diffusion

Dynamic loading introduces an additional governing time scale associated with deformation of the polymer network [347,376]. As illustrated in Fig. 13**A**, the deformation process may vary from quasi-static loading to rapid dynamic loading. The characteristic stretching time scale can be written as

$$\tau_s \sim \frac{1}{\dot{\lambda}} \tag{13}$$

where $\dot{\lambda}$ denotes the stretch rate. When the load is applied slowly, the hydrogel approaches the quasi-static regime, and particle diffusion is governed primarily by the static deformation state of the network. When the loading rate increases, however, the polymer cage surrounding the particle evolves during diffusion, and the hopping energy barrier becomes time-dependent. The influence of loading rate can be understood by comparing the diffusion time τ_d with the stretching time τ_s, as illustrated in Fig. 13**B**. When deformation is slow relative to particle

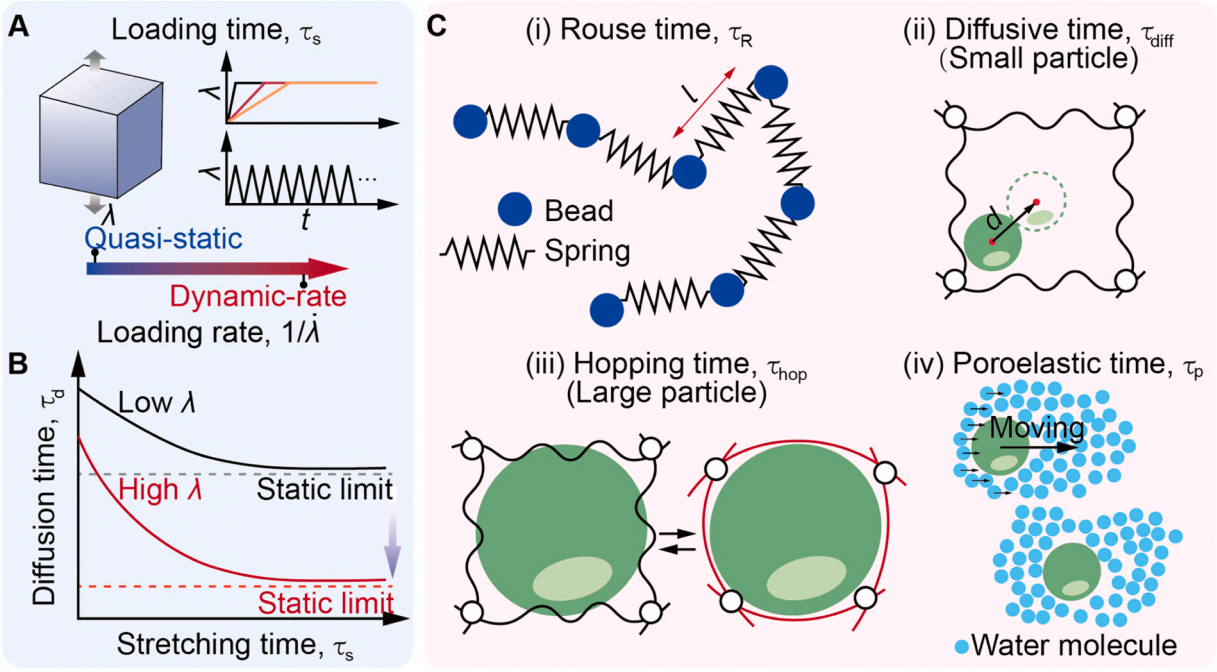


Fig. 13. Characteristic time scales governing mechano-diffusion under dynamic loading. (A) Deformation ranging from quasi-static to dynamic loading, characterized by the stretching time scale $\tau_s \sim 1/\dot{\lambda}$. (B) Influence of loading rate on diffusion time relative to the stretching time scale. (C) Hierarchy of characteristic time scales in polymer networks, including the Rouse relaxation time τ_R, diffusive time τ_{diff}, hopping time τ_{hop}, and poroelastic time τ_p, which together determine the dominant diffusion mechanism under dynamic deformation.

diffusion, the diffusion time approaches the static-loading limit [328]. As the loading rate increases, dynamic deformation modifies the local cage configuration and reduces the characteristic escape time required for particles from the cage [377].

Understanding this behavior requires considering several characteristic time scales within the hydrogel system, as summarized in Fig. 13**C**. The Rouse relaxation time τ_R describes the conformational relaxation of polymer chains [325,378]. When particles are significantly smaller than the network mesh size, diffusion occurs through Brownian motion characterized by the diffusive time τ_{diff}. For larger particles with sizes comparable to the mesh size, diffusion is dominated by hopping diffusion, characterized by a hopping time τ_{hop}, which depends strongly on the energy barrier associated with polymer chain deformation [330]. In addition, solvent migration within the network introduces the poroelastic time scale τ_p, corresponding to fluid redistribution during deformation [379–381]. The interplay among these time scales determines the dominant diffusion mechanism [371]. When $\tau_s \gg \tau_R$, polymer chains relax rapidly and particle diffusion approaches the static limit. Conversely, when $\tau_s \approx \tau_R$, deformation dynamically modulates the polymer configuration before relaxation occurs, producing rate-dependent diffusion behavior [370].

Dynamic loading thus introduces a hierarchy of time scales that governs particle diffusion in hydrogels. The competition among mechanical deformation, polymer relaxation, particle hopping, and solvent migration establishes the kinetic framework for mechano-diffusion under time-dependent mechanical conditions.

6.2. Coupled Effects of Network Elasticity and Reversible Interactions

As discussed in **Section 3.3** (Diffusing Particles: Geometry, Mechanics, and Interactions), particle diffusion in polymer networks is regulated not only by deformation of the network but also by interactions between particles and polymer chains [382](Figs. 6–7 and Tables 1–2) [147,338,383,384]. Two energetic contributions therefore govern diffusion: the elastic energy required to deform polymer chains and the reversible interaction energy associated with particle–polymer binding [382]. The physical origin of these two mechanisms is illustrated schematically in Fig. 14**A**. When a particle attempts to escape from a local cage formed by surrounding chains, the chains must stretch to create a transient opening, giving rise to an elastic energy barrier. In addition, particles may form reversible bonds with functional groups on polymer chains. The interaction strength is commonly described by

$$E_a = -RT\ln K_{eq} \tag{14}$$

where K_{eq} is the equilibrium binding constant. Reversible binding introduces an additional kinetic process in which particles attach to and detach from the network.

When reversible interactions are present, particle diffusion may proceed through a walking diffusion mechanism, where particles migrate through the network via repeated binding and release events [146,147,152]. This mechanism couples hopping diffusion with reversible binding kinetics and can significantly modify the effective particle diffusivity. Examples of such interaction-mediated diffusion have been demonstrated in several experimental systems. As shown in Fig. 14**B**, DNA-gated hydrogels can selectively regulate the diffusion of cargo molecules through transient DNA–DNA interactions between the cargo and gating strands embedded in the hydrogel network [385]. In this system, cargo molecules bearing complementary DNA sequences can partition into the hydrogel and subsequently diffuse through the network by sequential binding and release events. The diffusion process involves two coupled steps, illustrated in Fig. 14**C**. In the first step, reversible interactions facilitate cargo partitioning into the hydrogel network. In the second step, transient binding enables cargo molecules to move through the network via walking diffusion. The efficiency of this diffusion process depends strongly on the strength of the interaction [146,148]. As illustrated in Fig. 14**D**, weak interactions prevent particles from entering the hydrogel, whereas excessively strong interactions immobilize particles within the network. Enhanced diffusion occurs only at intermediate interaction strengths, where reversible binding is sufficiently strong to promote particle partitioning yet sufficiently transient to allow repeated hopping events.

These examples illustrate a general principle: reversible particle–polymer interactions can convert purely hindered diffusion into interaction-assisted hopping diffusion. The resulting diffusion behavior depends sensitively on the balance between the elastic energy barrier associated with network deformation and the kinetic time scale of reversible binding.

The combined effects of hopping and reversible binding lead to distinct diffusion regimes. As illustrated in Fig. 15**A**, these regimes can be organized in terms of the hopping time τ_{hop} and the binding time τ_b. When hopping is much faster than binding, diffusion approaches Brownian motion. When binding dominates, particles remain trapped in

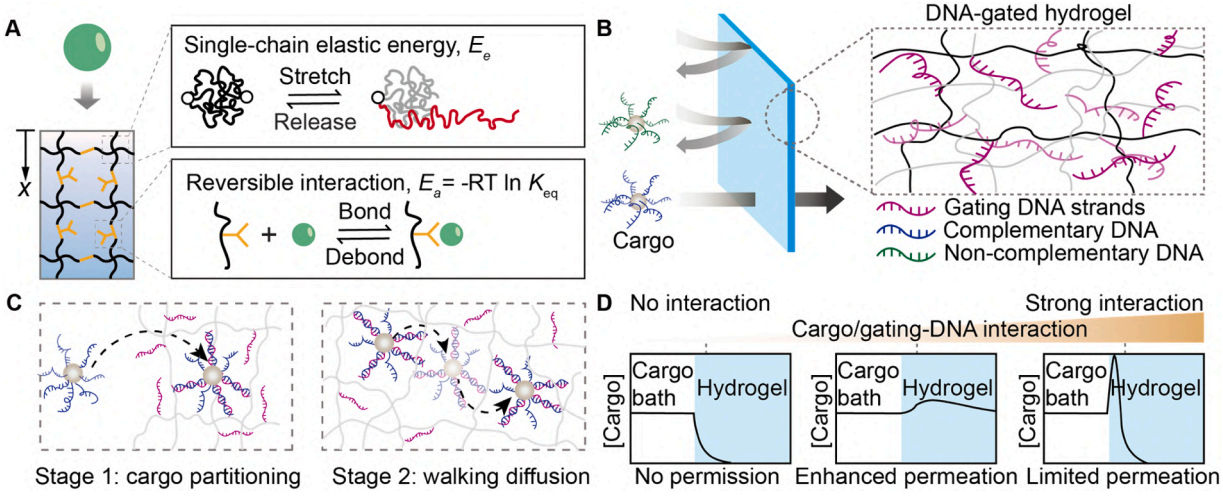


Fig. 14. Interaction-mediated diffusion through reversible particle–network binding. (A) Schematic illustration of elastic cage deformation and reversible particle–polymer binding that contribute to the diffusion barrier. (B) Example of interaction-controlled transport in DNA-gated hydrogels [385]. (C) Two-step walking diffusion mechanism involving particle partitioning into the network followed by migration through sequential binding and release events. (D) Dependence of particle transport on interaction strength, showing suppressed entry at weak interactions, immobilization at strong interactions, and enhanced diffusion at intermediate binding strength. Adapted with permission from Ref. [385]. Copyright 2021 American Chemical Society.

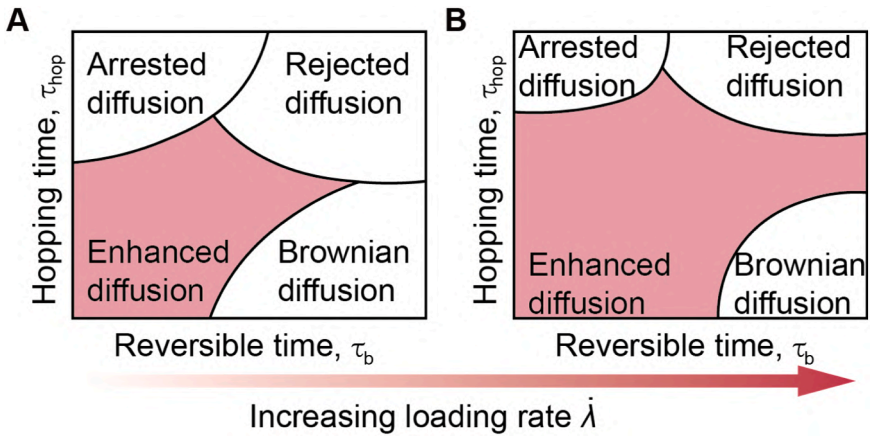


Fig. 15. Diffusion regimes governed by the competition between hopping and reversible binding. (A) Diffusion regimes organized in the $(\tau_{hop}|\tau_b)$ space, illustrating Brownian diffusion, arrested diffusion, and enhanced diffusion when hopping and binding occur on comparable time scales. (B) Effect of dynamic loading on the regime diagram, where deformation modifies the hopping time τ_{hop} and shifts the boundaries between diffusion regimes, expanding the region of enhanced diffusion.

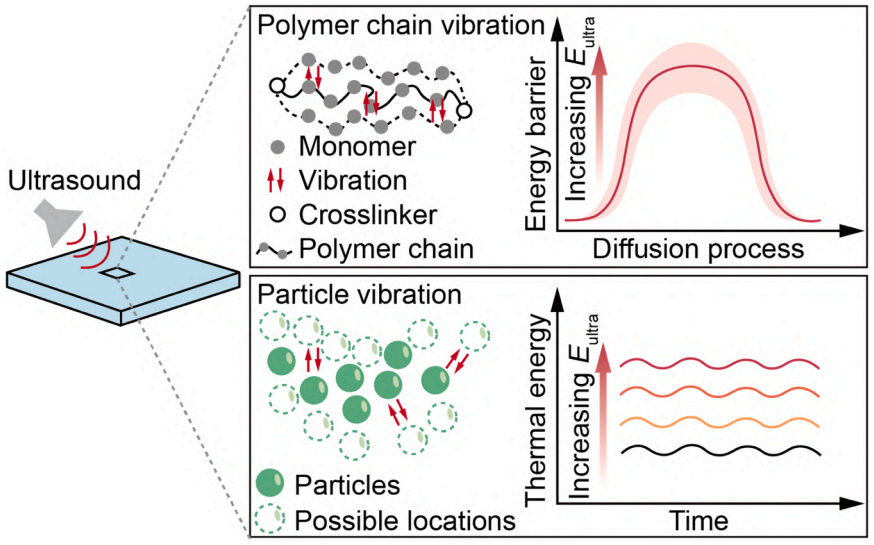


Fig. 16. Ultrasound-driven active mechano-diffusion in polymer networks. External ultrasonic excitation induces oscillatory deformation of the polymer network and enhances particle vibration, jointly modifying the hopping energy barrier and increasing the probability of cage escape. The combined effects of network deformation and particle vibration accelerate particle diffusion and can amplify size-dependent diffusion selectivity within the hydrogel.

bound states and diffusion is arrested. When hopping and binding occur on comparable time scales, repeated attachment and detachment facilitate particle migration and produce enhanced diffusion. Dynamic loading modifies the hopping energy barrier and therefore the hopping time τ_{hop}. Increasing the loading rate alters the boundaries between diffusion regimes in $(\tau_{hop}|\tau_b)$ space, as illustrated in Fig. 15**B**, thereby expanding the region corresponding to enhanced diffusion. Particle diffusion under dynamic loading is therefore governed jointly by network elasticity, reversible particle–polymer interactions, and the time scale of mechanical deformation.

6.3. *Active Mechano-Diffusion Driven by External Mechanical Stimuli*

External mechanical excitation provides an effective strategy to actively regulate mechano-diffusion in polymer networks by dynamically modifying the mechanical state of the network and the associated energy barrier governing particle motion. Among various external stimuli, ultrasonic excitation has recently emerged as a particularly attractive approach because it enables non-contact, spatially programmable, and temporally controllable regulation in hydrogel-based systems. Recent studies have highlighted the growing importance of ultrasound–hydrogel coupling in bioadhesion, implantable sensing, and biointegrated acoustic devices, further underscoring that ultrasound-mediated transport and mechanics in soft polymer networks are important for both fundamental understanding and technological applications [386–389]. Under ultrasonic stimulation, the polymer network experiences rapid oscillatory deformation. Recent studies in hydrogel model systems have shown that focused ultrasound can induce measurable matrix displacement/deformation and alter nanoparticle motion within the network [390]. Polymer chains surrounding a diffusing particle undergo repeated stretching and relaxation, which alters the elastic energy stored in the network. Because the hopping energy barrier for a particle escape from a polymer cage is determined by the deformation of the surrounding chains, oscillatory deformation of the network directly modifies the instantaneous energy barrier height associated with particle motion. In this sense, ultrasonic excitation introduces a time-dependent mechanical perturbation to the mechano-diffusion energy landscape.

In addition to deforming the polymer network, ultrasonic excitation

also enhances the kinetic motion of particles embedded within the hydrogel. Acoustic energy increases particle vibration and velocity fluctuations within the mesh space, thereby increasing the frequency with which particles attempt to overcome the hopping barrier separating neighboring polymer cages. As a result, particle motion is governed not only by thermal motion but also by mechanically induced oscillatory motion [390]. The mechano-diffusion process under ultrasonic stimulation can therefore be understood as a coupling between network deformation and particle vibration. Oscillatory deformation of the polymer network dynamically modifies the elastic energy stored in the surrounding chains and alters the hopping energy barrier, while particle vibration increases the probability that particles cross this barrier. The combined effect increases the rate of hopping events between neighboring polymer cages and accelerates particle diffusion within the network [390,391].

The influence of ultrasonic excitation depends strongly on the relationship between particle diameter d and the network mesh size ξ. When $d < \xi$, particles move relatively freely within the polymer mesh and ultrasound mainly enhances particle kinetic motion, leading to a moderate increase in diffusion rate. In contrast, when $d \approx \xi$, particles are temporarily confined within polymer cages and diffusion proceeds through hopping between neighboring cages. In this regime, oscillatory deformation of the network alters the elastic energy required for cage escape, while particle vibration increases the likelihood of crossing the hopping barrier. Consequently, ultrasonic excitation can significantly enhance mechano-diffusion even for particles that are strongly confined by the polymer network.

Because particles of different sizes experience different mechano-diffusion regimes, their responses to ultrasonic excitation are inherently non-uniform. Smaller particles respond more efficiently to the injected acoustic energy and exhibit a larger increase in kinetic activity, whereas larger particles remain partially constrained by steric confinement within the polymer network. As a result, ultrasonic excitation can amplify the intrinsic size-dependent disparity in mechano-diffusion behavior between different particle species, leading to enhanced diffusion selectivity within the same polymer network [390,391]. Unlike conventional selectivity mechanisms based on static mesh filtration or chemical affinity, ultrasound-driven mechano-diffusion relies on a dynamically tunable mechanical field that continuously modifies the elastic energy landscape governing particle motion. This externally driven regulation of mechano-diffusion provides a flexible strategy for controlling particle diffusion in soft polymer networks and offers potential opportunities for applications such as targeted drug release, adaptive separation systems, and responsive biosensing platforms [343].

7. Mechano-Diffusion Characterization Platform

Beyond theoretical studies on mechano-diffusion, experimental methodologies capable of probing particle transport are essential for validating mechanistic interpretations and resolving diffusion behaviors across different temporal and spatial scales. The preceding sections have established how particle diffusion in polymer networks is governed not only by network topology and particle-polymer interactions, but also by the nature of mechanical loading, ranging from quasi-static deformation to high-rate dynamic excitation. These considerations motivate the development and systematic comparison of experimental approaches that can quantify nanoparticle diffusivity in deformed media while accommodating mechanical constraints, optical accessibility, and time-scale requirements. Accordingly, this section focuses on mechano-diffusion characterization platforms, introducing both indirect and direct measurement methods and discussing their respective capabilities and limitations in capturing strain-dependent and rate-dependent mechano-diffusion phenomena.

7.1. Indirect Methods of Diffusivity Measurement

Indirect methods for measuring particle and molecular diffusivity constitute a broad class of experimental techniques that measure transport properties by characterizing diffusion behaviors of a system containing many particles in the medium, through the measurement of visible light intensity correlations, fluorescence intensity fluctuations, or color gradients in diffusion patterns, rather than by direct visualizing individual particle trajectories. Representative methods include dynamic light scattering (DLS) [392,393], fluorescence correlation spectroscopy (FCS) [394,395], fluorescence recovery after photobleaching (FRAP) [54,396,397], two-chamber diffusion cells [398], and nuclear magnetic resonance (NMR) [399,400].

Dynamic light scattering shown in Fig. 17**A** determines particle diffusivity by analyzing temporal fluctuations in the intensity of scattered light caused by Brownian motion of particles in suspension. Through the measurement of the intensity autocorrelation function and its exponential decay, the translational diffusion coefficient is extracted via the scattering vector-dependent decay rate. When a monochromatic laser beam illuminates a dilute dispersion, each particle acts as a scattering center, and the superposition of scattered waves at the detector produces an interference pattern whose intensity fluctuates in time as particles undergo random thermal motion. These fluctuations are characterized by the normalized intensity autocorrelation function, $g_2(\tau) = \langle I(t)I(t+\tau)\rangle/\langle I(t)\rangle^2$, which measures the decay of temporal correlations in the scattered intensity. The measured intensity correlation function is related to the electric-field autocorrelation function $g_1(\tau)$ through the Siegert relation, $g_2 = 1 + \beta|g_1(\tau)|^2$, where β is an instrumental coherence factor determined by the detection optics, ranging from 0.5 to 1. For monodisperse particles undergoing purely diffusive Brownian motion, the field autocorrelation function exhibits a single-exponential decay, $g_1(\tau) = \exp(-\Gamma\tau)$, with the decay rate Γ given by Berne & Pecora [401]

$$\Gamma = Dq^2 \tag{15}$$

where D is the translational diffusion coefficient, q is the scattering vector, $q = (4\pi n/\lambda) \bullet \sin(\theta/2)$, n is the refractive index of the medium, λ is the laser wavelength in vacuum, which can vary from 488 nm to 633 nm, and θ is the scattering angle, which is commonly 90° in conventional right-angle DLS measurements. By fitting the experimentally measured autocorrelation function, Γ can be extracted and the diffusivity D can be obtained. The principal advantage of DLS lies in its experimental simplicity, rapid data acquisition, and suitability for dilute suspensions of nanoparticles over a wide size range. However, DLS inherently provides an average diffusivity and is highly sensitive to polydispersity, multiple scattering, and aggregation. Moreover, it requires optically transparent samples and is not readily applicable to heterogeneous or solid-like media such as crosslinked hydrogels under deformation.

Fluorescence correlation spectroscopy, shown in Fig. 17**B**, measures diffusivity by correlating spontaneous fluctuations in fluorescence intensity as labeled particles stochastically traverse a small, optically defined observation volume. By fitting the fluorescence autocorrelation function, the characteristic diffusion time is obtained and converted to a diffusivity using calibrated optical parameters. In a typical confocal or two-photon FCS setup, a tightly focused laser creates a femtoliter-scale detection volume. As fluorescent particles diffuse in and out of this volume due to Brownian motion, the number of emitters within the detection region fluctuates, leading to corresponding fluctuations in the detected fluorescence signal F(t). These fluctuations are quantified using the normalized temporal autocorrelation function, $G(\tau) = \langle \delta F(t)\, \delta F(t+\tau)\rangle/\langle F(t)\rangle^2$, $\delta F(t) = F(t) - \langle F(t)\rangle$, which characterizes how rapidly fluorescence intensity fluctuations decorrelate in time. For particles undergoing free translational diffusion in three dimensions, and assuming a Gaussian-shaped confocal detection volume, the

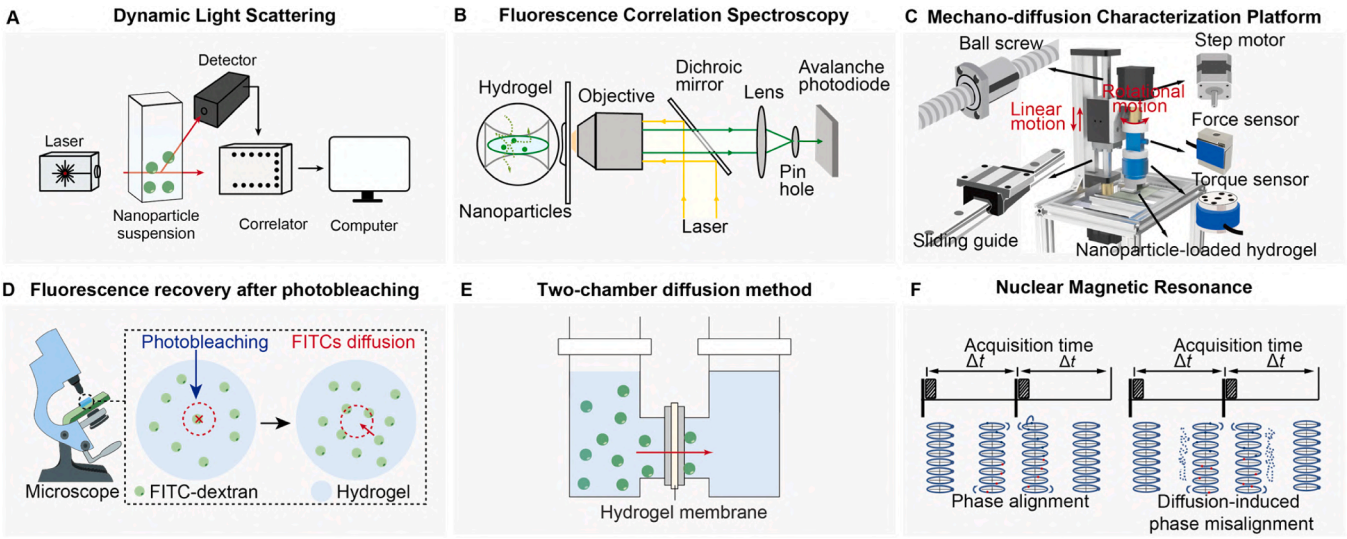


Fig. 17. Indirect methods for diffusivity measurement. (A) Dynamic Light Scattering (DLS), which extracts particle diffusivity from temporal fluctuations of scattered light intensity arising from ensemble Brownian motion; (B) Fluorescence Correlation Spectroscopy (FCS), which determines diffusivity by analyzing fluorescence intensity autocorrelations from molecules diffusing through a confined observation volume; (C) Mechano-diffusion Characterization Platform (MDCP), which infers diffusivity by reconstructing concentration fields under controlled mechanical deformation. Adapted from Ref. 294 under a CC BY-NC license, Springer Nature. (D) Fluorescence Recovery After Photobleaching (FRAP), which estimates diffusivity from the spatiotemporal recovery of fluorescence following localized photobleaching; (E) Two-chamber diffusion method, which evaluates diffusivity from concentration equilibration across a membrane separating two reservoirs; and (F) Nuclear Magnetic Resonance (NMR), which measures diffusivity through diffusion-induced attenuation of spin-echo signals under pulsed field gradients. These indirect techniques determine ensemble-averaged diffusivities by monitoring collective diffusion behaviors of particles or molecules rather than directly tracking individual trajectories.

autocorrelation function takes the form

$$G(\tau) = \frac{1}{N}\left(1+\frac{\tau}{\tau_D}\right)^{-1}\left(1+\frac{\tau}{\kappa^2\tau_D}\right)^{-\frac{1}{2}} \tag{16}$$

where N is the average number of fluorescent particles within the observation volume, $\kappa = z_0/w_0$ is the aspect ratio of the axial (z_0) to lateral (w_0) dimensions of the focal volume, and τ_D is the characteristic diffusion time. The diffusivity D is obtained from

$$\tau_D = \frac{w_0^2}{4D} \tag{17}$$

where w_0 is the lateral radius of the confocal volume determined by optical calibration. Thus, FCS yields translational diffusivity by linking the temporal decay of fluorescence correlations to the time required for particles to traverse the observation volume, providing a highly sensitive, local measurement of diffusion dynamics at the single-molecule or few-molecule level.

FCS offers extremely high sensitivity, enabling measurements at the single-molecule or few-molecule level with excellent temporal resolution. Its main limitations include the requirement for fluorescent labeling, susceptibility to photobleaching and blinking artifacts, and a strong dependence on accurate calibration of the detection volume. In addition, FCS probes diffusion only locally and yields an effective diffusivity that may not represent transport behavior over larger length scales or in mechanically heterogeneous environments.

The mechano-diffusion characterization platform (MDCP) shown in Fig. 17**C** determines nanoparticle diffusivity by coupling controlled mechanical deformation with spatiotemporal imaging of concentration fields in a cylindrical hydrogel geometry. The MDCP provides a distinctive and complementary approach to diffusivity measurement by reconstructing particle diffusivity from spatiotemporally resolved concentration fields under controlled mechanical deformation. In the experiments, nanoparticles initially confined to a central reservoir diffuse radially and axially through the hydrogel while the sample is subjected to prescribed tension or torsion. The measured grayscale intensity from time-lapse images is treated as a proxy for local concentration $c(r,z,t)$. Diffusion is modeled using Fick's second law, starting from the Cartesian form $(\partial c/\partial t = D\nabla^2 c)$, and reformulated in cylindrical coordinates to reflect the sample geometry. Assuming angular symmetry $(\partial c/\partial\theta = 0)$, the governing equation reduces to,

$$\frac{\partial c}{\partial t} = D\left(\frac{\partial^2 c}{\partial r^2}+\frac{1}{r}\frac{\partial c}{\partial r}+\frac{\partial^2 c}{\partial z^2}\right) \tag{18}$$

where r and z denote radial and axial directions, respectively. This formulation enables extraction of effective diffusivities that can vary spatially, capturing the experimentally observed strain-dependent and position-dependent diffusion behavior under nonuniform stress fields in the deformed hydrogel. To quantitatively determine diffusivity D, the finite difference method (FDM) is implemented in MATLAB to solve the cylindrical diffusion equation over the experimentally defined domain. The hydrogel is discretized in rz space with boundaries and initial conditions matching the experiment: a constant concentration $c = c_0$ in the central reservoir region and zero concentration elsewhere at $t = 0$. Time integration of the discretized diffusion equation generates simulated concentration profiles $c_{sim}(r,z,t;D)$. The diffusivity is then obtained by fitting these simulated profiles to the experimentally measured grayscale-derived concentration maps, minimizing the discrepancy between simulation and experiment.

The MDCP extracts diffusivity based on Fick's law, enabling direct coupling between mechanical loading and transport behavior. This allows MDCP to capture spatially heterogeneous, strain-dependent, and non-equilibrium diffusion processes that are inaccessible to conventional techniques. However, the method is inherently model-dependent, relying on assumptions regarding diffusion equations, boundary conditions, and image-to-concentration mapping, and is currently limited to mesoscopic length and time scales where optical imaging is feasible.

In Fig. 17**D**, fluorescence recovery after photobleaching (FRAP) quantifies particle diffusivity by tracking the temporal recovery of fluorescence after irreversible photobleaching within a localized region. In a typical experiment, fluorescently labeled particles are imaged at steady state, followed by a high-intensity laser pulse that bleaches

fluorophores in a defined region of interest (ROI), creating a spatially nonuniform fluorescence profile. Fluorescence recovery occurs as unbleached particles diffuse into the ROI while bleached particles diffuse out. For an idealized two-dimensional system with an instantaneous circular bleach of radius w, the normalized fluorescence recovery can be expressed, following the Soumpasis Equation

$$f(t) = \exp\left(-\frac{2\tau_D}{t}\right)\left(I_0\left(\frac{2\tau_D}{t}\right) + I_1\left(\frac{2\tau_D}{t}\right)\right), \quad \tau_D = \frac{w^2}{4D} \tag{19}$$

where I_0 and I_1 are the 0th and 1st order modified Bessel functions, τ_D is the characteristic diffusion time, and D is the diffusivity. Because FRAP probes fluorescence recovery over micrometer length scales, it provides a spatially averaged measure of diffusivity and is particularly well-suited for characterizing transport in heterogeneous or constrained environments, such as membranes, polymer networks, and hydrogels.

A key advantage of FRAP is its conceptual simplicity and compatibility with complex biological and polymeric systems, including membranes and hydrogels. However, FRAP measurements are intrinsically spatially averaged over the bleached region and are sensitive to the assumed bleaching geometry and recovery model. Irreversible photobleaching, limited temporal resolution for fast diffusion, and difficulty in separating diffusion from binding or reaction kinetics further constrain its quantitative accuracy.

In Fig. 17**E**, the two-chamber diffusion cell measures membrane diffusivity by monitoring mass transport driven by a concentration difference across a membrane separating two well-stirred reservoirs. One donor chamber is initially loaded with solute at a concentration $C_1(0)$, while the other receiver chamber starts at $C_2(0) = 0$. Because each chamber is assumed to be spatially uniform, the only concentration gradient exists across the membrane thickness L and area A. The transmembrane flux follows a linear driving force form, $J(t) = P[C_1(t) - C_2(t)]$, where P is the membrane permeability. At the microscopic level, permeability is related to the intrinsic membrane diffusivity through, $P = KD/L$, K is the partition coefficient between the solution and the membrane, which can be regarded as 1. Thus, measuring P provides direct access to D once L is determined. The time evolution of concentrations in the two chambers follows mass conservation: $V_1\partial c_1/\partial t = -AJ$, $V_2\partial c_2/\partial t = AJ$, where V_1 and V_2 are the chamber volumes. Combining these equations yields an exponential decay of the concentration difference $\Delta C = C_1(t) - C_2(t)$,

$$\Delta C(t) = \Delta C(0)\exp\left[-AP\left(\frac{1}{V_1} + \frac{1}{V_2}\right)t\right] \tag{20}$$

By fitting the experimental concentration–time data to this expression, the permeability P is obtained from the decay rate, and the membrane diffusivity is then calculated as $D = PL/K$. This approach provides an effective, macroscopic measurement of diffusivity across the membrane under well-controlled boundary conditions.

The two-chamber diffusion cell method is robust, conceptually straightforward, and well-suited for studying transport across membranes under well-defined boundary conditions. Its main disadvantage is that it yields only a macroscopic, averaged diffusivity across the entire membrane thickness, providing no spatial or temporal resolution within the medium. Additionally, assumptions of uniform mixing, constant partition coefficients, and one-dimensional transport may limit accuracy in heterogeneous or deformable systems.

Fig. 17**F** illustrates how nuclear magnetic resonance (NMR) measures molecular diffusivity by encoding particle displacement into the phase of nuclear spins using magnetic field gradients. In a uniform magnetic field, nuclear spins process at the Larmor frequency, but when a pulsed magnetic field gradient (PFG) is applied, spins at different spatial positions acquire different phases. In a typical Hahn spin-echo or stimulated-echo PFG sequence, a first gradient pulse of strength g and duration δ imprints a position-dependent phase $\phi = \gamma g\delta x$, where γ is the gyromagnetic ratio. After a diffusion time Δ, during which molecules undergo Brownian motion, a second identical gradient pulse is applied. If molecules have not moved, the second pulse exactly refocuses the phases and a full echo is recovered; however, diffusive displacement causes incomplete refocusing, leading to attenuation of the echo signal.

The loss of signal intensity reflects the statistical distribution of molecular displacements and is quantitatively related to the diffusion coefficient. For free, isotropic diffusion, the normalized echo attenuation follows the Stejskal–Tanner equation :

$$\frac{S}{S_0} = \exp\left[-\gamma^2 g^2 \delta^2 \left(\Delta - \frac{\delta}{3}\right)D\right] \tag{21}$$

where S_0 is the echo amplitude without gradients, S is the measured signal, and D is the diffusivity. By systematically varying the gradient strength g or δ, and fitting the exponential of S/S_0, the diffusivity D can be extracted without requiring concentration gradients or optical labels. Because NMR probes ensemble-averaged molecular motion over micrometer length scales and millisecond timescales, it provides an absolute, model-independent measurement of diffusivity in liquids, gels, and porous media. NMR offers a major advantage in being noninvasive, label-free, and applicable to opaque or optically complex systems, including gels and porous media. Nevertheless, NMR typically requires specialized and expensive instrumentation, has relatively low spatial resolution compared to optical methods, and yields volume-averaged diffusivities that may obscure local heterogeneities or strain-induced variations in transport.

7.2. Direct Methods of Diffusivity Measurement

Direct diffusivity measurement methods determine particle diffusivity by explicitly resolving and analyzing the motion of individual particles. These direct methods are primarily based on advanced optical microscopy and include label-free interferometric scattering microscopy (iSCAT) [402,403] and fluorescence-based total internal reflection fluorescence microscopy (TIRF) [404,405]. In both cases, particle diffusivity is obtained from time-resolved trajectories and subsequent mean-squared displacement (MSD) analysis, providing a local and non-averaged description of transport dynamics.

The relationship between the mean-squared displacement (MSD) and diffusivity is a fundamental result of Brownian motion theory and provides the theoretical basis for extracting diffusivity from particle trajectories in single-particle tracking experiments. For a particle undergoing free and isotropic Brownian diffusion, the MSD is defined as $\mathrm{MSD}(\Delta t) = \left\langle |\boldsymbol{r}(t+\Delta t) - \boldsymbol{r}(t)|^2 \right\rangle$, where $r(t)$ is the particle position as time t, Δt is the time lag, and $\langle\cdot\rangle$ denotes an ensemble or time average. In this case, the MSD increases linearly with time lag, and the proportionality constant is directly related to the diffusivity D. In 2D scenarios, the diffusivity can be determined by,

$$D = \frac{MSD}{4\Delta t} \tag{22}$$

While in 3D scenarios, the diffusivity can be determined by,

$$D = \frac{MSD}{6\Delta t} \tag{23}$$

Interferometric scattering microscopy (iSCAT) is a label-free technique that detects nanoparticles through the interference between light scattered by the particle and a coherent reference field reflected from a nearby interface [406–408]. When a nanoparticle enters the illumination volume, it scatters a weak electromagnetic field whose amplitude depends on the particle's polarizability, which in turn is related to its size and refractive index. This scattered field interferes with the much stronger reference field, converting minute scattering signals into measurable intensity contrast on a camera. Because iSCAT does not rely on fluorophores, it avoids photobleaching and blinking, enabling long-term tracking of individual particles with nanometer spatial

precision and microsecond-to-millisecond temporal resolution. By localizing particle positions frame by frame, full trajectories are reconstructed, from which diffusivity is directly extracted via MSD analysis.

The iSCAT microscope can be implemented in a reflecting geometry using a widefield illumination path. In Fig. 18**A**, a coherent light source is expanded and weakly focused by a widefield lens and directed into the microscope objective via a beam splitter and steering mirror. The illumination is focused on the back focal plane of the objective, producing collimated illumination at the sample plane. Nanoparticles located at or near the coverslip-sample interface are illuminated through the objective. Light reflected from the refractive index discontinuity at the coverslip interface and light scattered by the nanoparticles are collected by the same objective and retrace the illumination path. After passing back through the beam splitter, the combined reflected and scattered fields are relayed by a tube lens onto a CMOS (Complementary Metal Oxide Semiconductor) camera, where the interferometric signal is recorded.

The iSCAT enables high-speed, label-free detection and tracking of nanoparticles, proteins, and other nanoscopic objects at interfaces, making it particularly powerful for single-particle tracking, membrane biophysics, and diffusion measurements. Its key characteristics include shot-noise-limited sensitivity, linear scaling of signal with particle polarizability, and compatibility with extremely high frame rates due to the absence of photobleaching or saturation effects. Compared with fluorescence microscopy, iSCAT offers superior temporal resolution and unlimited observation time; compared to dark-field scattering, it provides enhanced sensitivity to small particles. However, iSCAT also has limitations: it lacks intrinsic chemical specificity, is sensitive to mechanical and interferometric instability, and suffers from background artifacts under simple widefield illumination.

Total internal reflection fluorescence microscopy (TIRF), in contrast, is a fluorescence-based technique that selectively excites labeled particles near an interface. When light undergoes total internal reflection at a glass-water interface, an evanescent electromagnetic field is generated that decays exponentially away from the surface, typically penetrating only 100 −200 nm into the sample. Fluorescently labeled particles entering this evanescent field are selectively excited and emit fluorescence that is detected with high signal-to-noise ratio. This surface-confined excitation suppresses background fluorescence from the bulk, allowing precise localization and tracking of single particles near interfaces such as membranes or substrates. Although TIRF requires fluorescent labeling and is subject to photobleaching, it provides excellent chemical specificity and is widely used for direct diffusivity measurements in interfacial and near-surface environments.

In Fig. 18**B**, the TIRF microscope uses a laser coupled into an optical fiber and collimated by relay optics, with the beam laterally translated by a micrometer-controlled lens system to control its position at a plane which conjugates to the objective back focal plane (BFP) [409–411]. By displacing the beam off-axis at the objective's BFP, the illumination exits the high-NA oil-immersion objective at a supercritical angle, producing total internal reflection at the glass-sample interface and generating an evanescent field that selectively excites fluorophores within $\sim 100-200$ nm of the coverslip. Fluorescence emission is collected by the same objective, separated from the excitation light by a dichroic mirror, and imaged onto an EMCCD (Electron-Multiplying Charge-Coupled Device) camera via a tube lens.

TIRF microscopy enables highly selective imaging of fluorescently labeled molecules near interfaces by exciting fluorophores only within the evanescent field ($\sim 100 - 200$ nm) generated at the glass-sample boundary, making it particularly powerful for single-molecule detection, membrane biophysics, and near-surface diffusion measurements. Its key characteristics include excellent signal-to-background ratio due to suppressed bulk fluorescence, intrinsic chemical and molecular specificity provided by fluorescence labeling, and compatibility with single-particle tracking at high spatial precision. Compared to widefield fluorescence microscopy, TIRF offers superior background rejection and sensitivity for interfacial processes; compared to label-free methods such as iSCAT, it provides molecular specificity and multiplexing capability. However, TIRF is limited by the need for fluorescent labels, photobleaching and phototoxicity, a restricted axial observation depth, and finite temporal resolution imposed by fluorophore brightness and saturation.

8. Simulation Methods for Characterizing Diffusion Behaviors

The study of mechano-diffusion examines how an externally applied mechanical load alters the microstructural geometry of soft materials and subsequently reshapes the effective free-energy landscape governing penetrant motion [54,243]. These changes together control the transport characteristics of the polymer networks, influencing mean-squared displacements, long-time diffusion coefficients, and the onset of non-Fickian diffusion. However, determining exact microstructures and diffusion dynamics remains a formidable experimental challenge. Under this context, computational simulations offer a

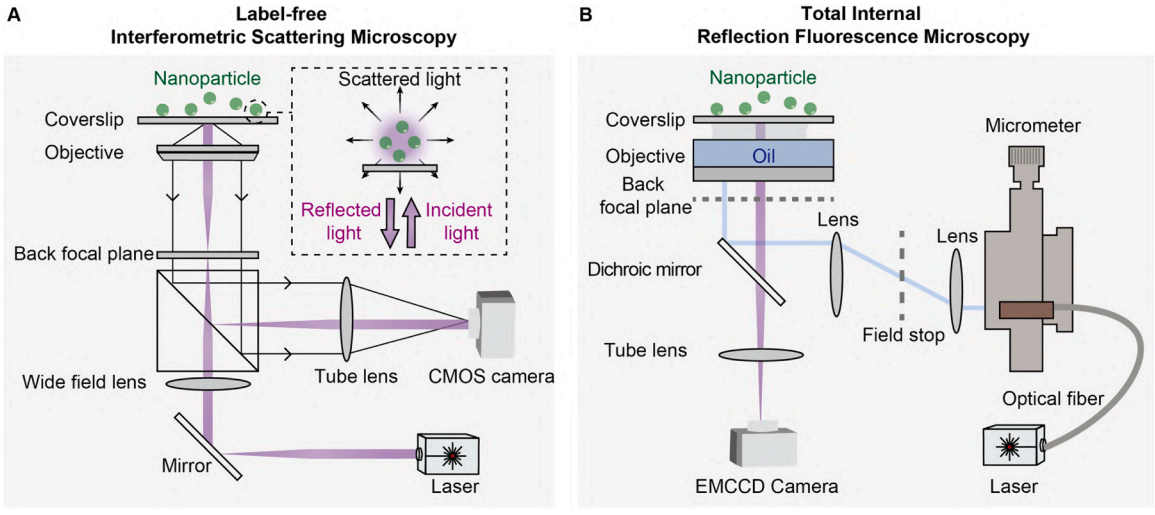


Fig. 18. Direct Methods to Measure Diffusivity iSCAT and TIRF Microscopy Optical Layouts. (A) The iSCAT microscopy leverages the interference between the reflective light from the cover slip and the scattered light from the nanoparticles, which can form monochromatic images on the CMOS camera. (B) The TIRF microscopy selectively excites fluorophores within $\sim 100-200$ nm of a glass-sample interface by using an evanescent field generated from total internal reflection, thereby enabling high signal-to-the background imaging. The direct methods to measure particle diffusivity can capture the trajectory of single particles or molecules.

straightforward framework to compute transport observables under prescribed deformation states and illustrate microscopic mechanisms that are obscure in experiments by explicit control over network structures, particle properties, and interaction potentials.

Simulations for characterizing transport behavior typically involve model construction, dynamics simulations, and analysis of dynamical observables. In this section, the typical methods for each part are discussed.

8.1. Network and Particle Model Construction

The first step in computational simulation is to properly set up models for polymer networks and penetrant particles, as well as to assign their governing interactions (Table 11). The polymer networks are typically modeled via bead-spring model [412], a standard model in molecular dynamics investigations of generic polymer properties. The model represents each group of monomers as a single bead connected via springs. The networks are composed of crosslinkers and strands between them, with a variety of properties such as crosslinker functionality and spatial arrangement, strand length dispersity and flexibility. They may also be subjected to topological defects and external mechanical loads.

The topology of polymer network describes the spatial connectivity of its components, typically idealized as crosslinkers and strands [430]. Crosslinker functionality defines the local connectivity dictated by precursors' geometric architectures and chemistry [163,431,432], forming 3-chain [332,413], 4-chain [243,339,413–417], 6-chain [64,65,384,413,414,418,419–424] and 8-chain [414] models. Both crosslinker functionality and spatial arrangement (Fig. 19**A**) define whether the polymer medium acts as an idealized lattice-like network or a random porous network. Lattice-like polymer networks [64,65,243,384,413–424] are frequently employed with compatible crosslinker functionality to establish clear mechanistic understanding for the influence of confinement on penetrant transport, framing the long-time diffusion as a series of movement between equivalent unit cells. In addition, the cell topology of lattice-like networks is shown to profoundly reshape the free-energy landscape, where changes in cell topology give rise to distinct dynamical regimes [413]. Conversely, real hydrogels and biological matrices inherently possess broad distributions of local crosslink densities, thereby leading to a wide range of pore sizes [425,433]. To capturing this reality, researchers employ disordered random networks [332,338,339,370,371,425–428] with monodisperse [64,65,243,339,384,413–424] or polydisperse [332,338,370,371,424,425–428] strand length distributions (Fig. 19**B**), which naturally produce spatially heterogeneous mobility, and non-Gaussian displacements within complex physiological environments. Beyond the overall polymer network architecture, localized topological defects (Fig. 19**C**) like loops and dangling chains also fundamentally alter the transport behaviors. In highly crosslinked environments, ring topologies effectively introduce additional crosslinking sites, resulting in a denser, smaller-mesh network compared to networks formed by linear chains. The compact structure increases matrix viscosity and suppresses the penetrant hopping behaviors [428]. Thus, network topology serves as a critical design parameter for both energy-landscape and dynamic mechanisms.

The flexibility of strands (Fig. 19**B**) in polymer networks brings about dynamics coupling between the polymer networks and penetrants. Physically, the flexibility is characterized by the persistence length (l_p) relative to the bond length (l_b) and contour length (L) of strand [434,435]. Flexible networks [65,332,338,339,370,371,384,413–417,419,420,422–424,428], where $l_p \approx l_b$ and $l_p \ll L$, typically model thermally fluctuating chains and capture pronounced loops' size fluctuation. Semiflexible networks [339,414,423,425,426], characterized by $l_b \ll l_p \ll L$ introduce a pronounced intrinsic bending stiffness. This rigidity creates an effective barrier that balances conformational entropy against mechanical bending energy required for particles penetration. Due to the overlap between the network's relaxation spectrum and the penetrant diffusion time-scale, the bending stiffness profoundly dictates the transport behaviors [414]. Conversely, rigid networks [64,414,420,421,423,426,427] with $l_p \gg L$ strongly suppress thermal fluctuations and approximate static porous scaffolds. They provide essential baseline models to isolate purely topological obstruction without the complex interference of viscoelastic relaxation.

Besides the polymer network features, the physical attributes of penetrants also affect the transport behaviors. Spherical penetrant particles [65,243,332,338,370,371,384,413,415–421,423,425,428] are the standard paradigm, reducing geometric complexity with isotropic scalar diffusivity. On the other hand, the anisotropic nature of many biological penetrants necessitates the use of rodlike particles [338,414,422,424,426] and sphero-cylinders [427]. These models reveal complex translation-rotation coupling, highlighting rotation-dependent diffusion pathways [422] and unconventional sliding dynamics [424].

Furthermore, particle rigidity dictates the deformability of the penetrant particles. While rigid particles [64,65,243,332,338,339,370,371,413–418,420,421–425,427,428] simplify penetrants' elasticity response to the environment, many real biological nanoparticles are highly compliant [419,426]. Incorporating elastic, deformable particles [384,419,426] allows simulations to capture how penetrant compliance reduces effective energy barriers. In the context of mechano-diffusion, this is particularly salient, as applied external deformation can act synergistically with particle deformation to alleviate steric hindrance.

The transport of particles through a polymer network is fundamentally governed by the effective energy landscape formed by particle-network interactions. These interaction potentials determine whether the transport is obstruction-limited, where motion is hindered by physical barriers, or trap-limited, where particles are delayed by attractive polymeric sites. To isolate the effects of geometric

Table 11
Overview of key simulation parameters for studying penetrant transport dynamics in polymer networks.

Category	Key parameter	Typical examples
Polymer network	Crosslinker functionality	3-chain [332,413], 4-chain [243,339,413–417], 6-chain [64,65,384,413,414,418,419–424], 8-chain [414]
	Crosslinker arrangement	Lattice-like [64,65,243,384,413–424], random [332,338,339,370,371,425–428]
	Strand length dispersity	Monodisperse [64,65,243,339,384,413–424], polydisperse [332,338,370,371,424,425–428]
	Strand flexibility	Flexible [65,332,338,339,370,371,384,413–417,419,420,422–424,428], semiflexible [339,414,423,425,426], rigid [64,414,420,421,423,426,427]
	Topological perfection	Defect-free [64,65,243,332,384,413–424], defective [338,370,371,425,426–428]
	Mechanical state	Uniaxial stretch [54,243], biaxial stretch [243], shear [243]
Penetrant particle	Shape	Spherical [65,243,332,338,370,371,384,413,415–421,423,425,428], rodlike [338,414,422,424,426], spherocylinder [427]
	Rigidity	Rigid [64,65,243,332,338,339,370,371,413–418,420,421–425,427,428], elastic [384,419,426]
Particle-network interaction	Excluded-volume interaction	Hard sphere potential [64,413,416], WCA potential [243,332,415,427,428]
	Soft repulsive interaction	DPD conservative potential [65,414,420,422,424,425,429]
	Van der Waals interaction	Lennard-Jones potential [332,338,339,370,371,384,417–419,421,423,426,428]
	Solvent-mediated interaction	Morse potential [427]
	Electrostatic interaction	Screened electrostatic potential [64], screened Debye–Hückel potential [416]

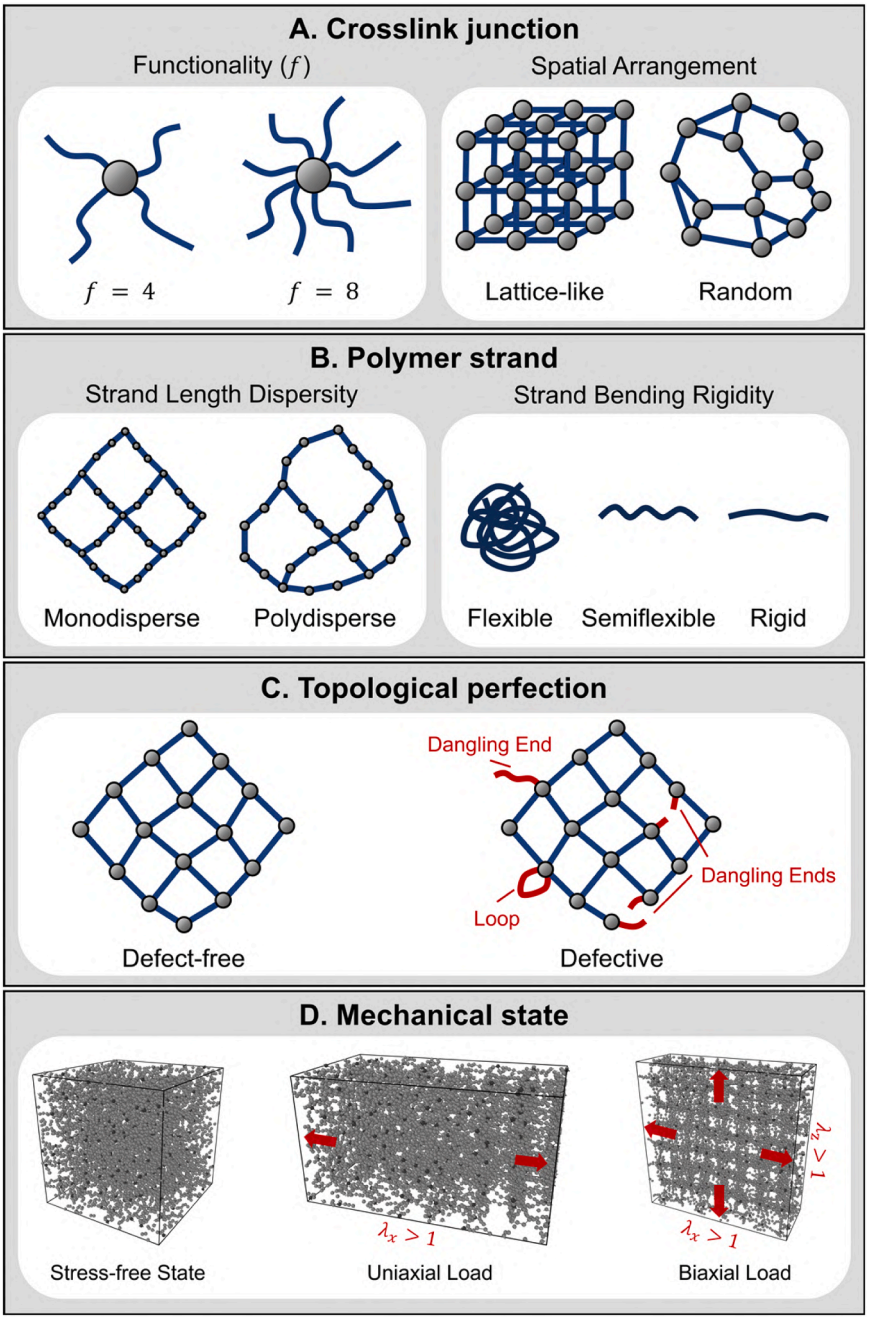


Fig. 19. Classification of computational polymer network models. Models are defined by properties of crosslink junctions and polymer strands. (A) Crosslink junctions are dictated by functionality f and spatial arrangement. (B) Polymer strands are characterized by length dispersity and bending rigidity. (C) Topological perfection contrasts ideal, fully connected networks against non-ideal networks containing defects such as dangling ends and loops. (D) External mechanical load actively reconfigures the network, inducing anisotropic pore geometry.

confinement, researchers typically employ purely repulsive interactions, ranging from idealized hard-sphere constraint [64,413,416] to the continuous Weeks-Chandler-Andersen (WCA) potential [243,332,415,427,428,436], which model excluded volume effect. Beyond these hard-core repulsions, dissipative particle dynamics (DPD) utilizes soft conservative repulsions coupled with dissipative and random forces [65,414,420,422,424,425,429]. The soft-repulsion formulation is particularly advantageous for studying mechano-diffusion, as it prevents numerical instabilities during large structural overlaps and provides robust hydrodynamic interactions under large mechanical deformations [437–443].

When chemical affinity must be considered – such as in mucosal barriers [418] or functionalized hydrogels [384,419] – attractive potentials become necessary to capture trap-limited diffusion. In coarse-grained frameworks, the standard Lennard-Jones (LJ) interaction remains foundational for tuning overall polymer-particle affinity [332,338,339,370,371,384,417–419,421,423,426,428]. Recent penetrant-in-network studies emphasize that LJ-mediated interactions can profoundly alter matrix segmental relaxation, coupling local nanoparticle hopping directly to polymer dynamics [338,371]. However, the traditional LJ potential rigidly couples the interaction range to the particle size, which can lead to non-physical long-range attraction in a dense network. To overcome this limitation, the Morse potential [444] is employed. By introducing an independent range parameter, the Morse potential allows for the precise decoupling of steric repulsion from adhesive interactions, enabling accurate modeling of discrete, short-range

adhesion sites without altering the particle's effective radius.

Beyond neutral steric and adhesive interactions, electrostatic forces introduce an additional layer of complexity in charged hydrogel networks or polyelectrolyte solutions. To model these effects, screened electrostatic potentials [64] or Debye-Hückel potential [416] are commonly utilized. These potentials capture the critical role of solvent ionic strength and the corresponding Debye screening length. Depending on the charge distribution, electrostatic interactions can either strongly exclude penetrants from polymer-dense regions via charge repulsion or induce long-lasting trapping through local electrostatic attraction, fundamentally altering the effective energy landscape the diffusing penetrants experience.

Ultimately, the selection of these modeling parameters forms a highly specific design space. Ordered lattices with repulsive interactions provide fundamental, interpretable models of barrier crossing, whereas the introduction of disorder in topology, semiflexibility in strand, and electrostatic attraction captures the highly heterogeneous, viscoelastic reality of biological tissues. By carefully calibrating these structural and interactive features, simulations lay the necessary groundwork for the subsequent imposition of external mechanical load, where the interplay between mechanical strain and the pre-defined energy landscape ultimately governs the emergent mechano-diffusive response.

8.1.1. Mechanical Control

In mechano-diffusion simulations, the applied mechanical loading protocol (Fig. 19**D**) serves as another control variable that dictates the pore anisotropy and strand-tension state of the polymer network. Practically, this is implemented by subjecting the network model to a prescribed mechanical deformation history. Recent computational studies have predominantly utilized strain-controlled protocols [54,243], enabling direct comparison of penetrant diffusivity at different strain states. The specific strain state, such as uniaxial, biaxial or shear strain, plays a critical role in reshaping the effective energy landscape and different transport responses.

8.1.2. Dynamic Solver

To precisely simulate the microscopic stochastic diffusion process necessitates careful selection of the dynamic solver. As summarized in Table 12, the choice of simulation algorithm dictates what physical phenomena are explicitly resolved depending on physical process desired to study.

At the highest level of resolution, all-atom molecular dynamics (AA-MD) retains full chemical specificity and explicit solvent molecules, thereby naturally preserving momentum and hydrodynamic interaction. It is primarily deployed when interfacial chemistry governs network permeability, such as resolving specific non-covalent drug binding [445] or elucidating how local hydration and ion concentrations dynamically respond to macroscopic mechanical actuation [429]. Furthermore, AA-MD is frequently employed as a foundational tool to rigorously compute localized interaction parameters, providing critical physicochemical inputs for mesoscale models. By coupling atomistic parameters with coarse-grained molecular dynamics (CG-MD), researchers can successfully reveal how the tuned deformability of soft nanoparticles allows them to adaptively bypass steric constrains in biological hydrogels [384,419]. Although chemical specificity is fully resolved in AA-MD, it is far too slow to systematically explore the large spatiotemporal scales typical of macroscopic diffusion.

To overcome the spatiotemporal limitations of AA-MD, CG-MD significantly accelerates the simulation by grouping neighboring monomers and solvent molecules into lumped beads thus reducing the degree of freedoms of dynamic variables. CG-MD successfully captures how network segment relaxation [370,371], particle shape [338,339], particle rigidity [419], and deformation-induced structural anisotropy [243] regulate penetrant transport. Nevertheless, explicitly resolving tens of thousands of solvent beads in CG-MD remains a severe computational bottleneck, limiting the accessible timescale for observing long-time penetrant diffusion.

To further accelerate simulations and access macroscopic spatiotemporal scales, implicit-solvent methods such as Langevin dynamics (LD) and Brownian dynamics (BD) offer highly efficient alternatives. These methods replace the solvent with a stochastic thermostat that balances continuous frictional drag with random thermal noise. The difference for both methods lies between that BD is overdamped and ignores inertial term. LD and BD are computationally efficient for investigating penetrant transport behavior in static or slowly evolving matrices [64,332,384,413,415–417,419,421,423,426,427,446] when the long-time diffusion behavior is of primary interest. However, the elimination of the explicit solvent breaks the conservation of local momentum, and solvent-mediated hydrodynamic interactions are lost. Consequently, LD and BD cannot accurately capture drag-coupled fluid flows under macroscopic deformations.

To resolve the dilemma between computational efficiency and hydrodynamic fidelity, DPD has emerged as a powerful tool [437–443]. DPD retains coarse-grained explicit solvent beads but replaces the hard-core repulsive potential of typical CG-MD with a soft potential, permitting larger integration timesteps and substantially boosting computational speed. Crucially, the pairwise dissipative and random forces in DPD are specifically designed to strictly conserve local momentum, thereby recovering Navier-Stokes hydrodynamics at the mesoscale [441]. By leveraging these advantages, recent DPD simulations have successfully elucidated complex transport mechanisms that depend heavily on fluid-structure interactions. For instance, DPD explicitly resolves local network deformations and energy barriers, enabling the tracking of bounce-back hopping events [65,414]. Furthermore, its explicit solvent reveals hydrodynamic lubricity that assists pore penetration [420], and captures the unconventional sliding of nanorods [424]. Consequently, DPD is uniquely advantageous for modeling drag-coupled penetrant motion under severe, large-strain mechanical loads.

8.1.3. Computational Observables and Trajectory Analysis

Translating raw simulation trajectories into physically meaningful insights requires the computation of specific statistical observables (Fig. 20). Direct visualization of these trajectories immediately reveals distinct transport modes, such as continuous diffusion, intermittent activated hopping, and constrained trapping [414] (Fig. 20**A**). The most fundamental observable is the mean-squared displacement (MSD) (Fig. 20**B**), calculated from the ensemble average of particle trajectories over time. The MSD yields the long-time effective diffusivity and identifies the transport regime via the anomalous exponent. While diffusion in simple liquids is typically Fickian, transport in complex polymer networks often exhibits transient subdiffusion [414,424]. Crucially, under anisotropic mechanical loads, the scalar diffusivity is generalized to a diffusion tensor. Analyzing the directional MSD allows researchers to directly quantify the degree of deformation-induced transport anisotropy [243].

Beyond time-averaged macroscopic metrics, simulations excel at

Table 12
Overview of molecular simulation methods and their governing physical approximations.

Method	Solvent	Momentum	Hydrodynamic interaction	Reference
AA-MD	Explicit	Conserved	Preserved	[384,419,429,445]
CG-MD	Explicit	Conserved	Preserved	[243,338,339,370,371,418]
LD	Implicit	Non-conserved	Neglected	[332,384,413,417,419,421,423,426]
BD	Implicit	Non-conserved	Neglected	[64,415,416,427,446]
DPD	Explicit	Conserved	Preserved	[65,414,420,422,424,425]

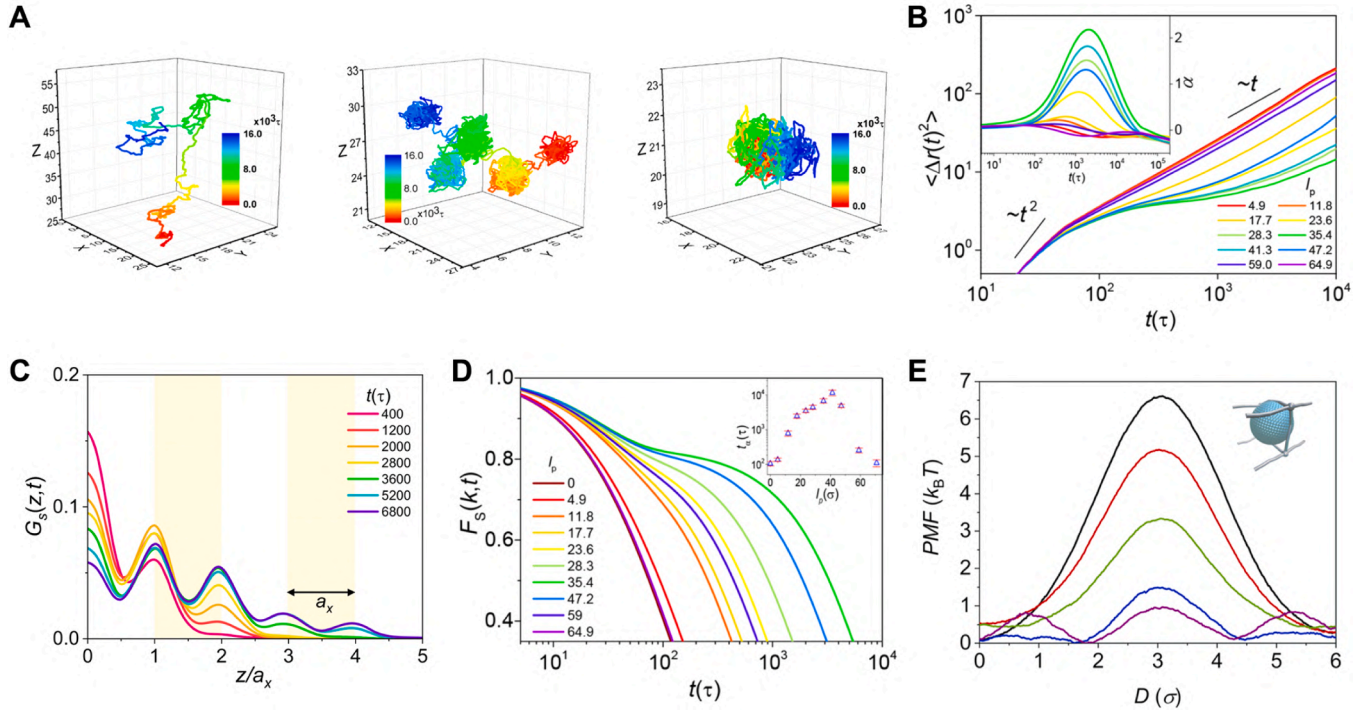


Fig. 20. Computational observables from penetrant dynamics to thermodynamic landscapes. (A) Representative 3D trajectories of distinct transport modes: continuous diffusion (left), intermittent activated hopping (middle), and constrained trapping (right). (B) Mean-squared displacement (MSD) and non-Gaussian parameter (inset) versus time for varying polymer chain rigidities. (C) The van Hove self-correlation function at different time intervals. (D) Intermediate scattering function capturing structural relaxation. Inset: Non-monotonic dependence of relaxation time on polymer rigidity. (E) PMF profiles mapping the free energy landscape; the hopping barrier peak varies with nanoparticle–polymer interaction strength. [414]. Copyright 2021 American Chemical Society (A, B, D). [424] under a Creative Commons Attribution 4.0 International License (C). [421]. Copyright 2022 AIP Publishing (E).
(a) (A), (B), and (D) adapted with permission from Ref. (b) Panel (E) adapted with permission from Ref. (c) (C) adapted from Ref.

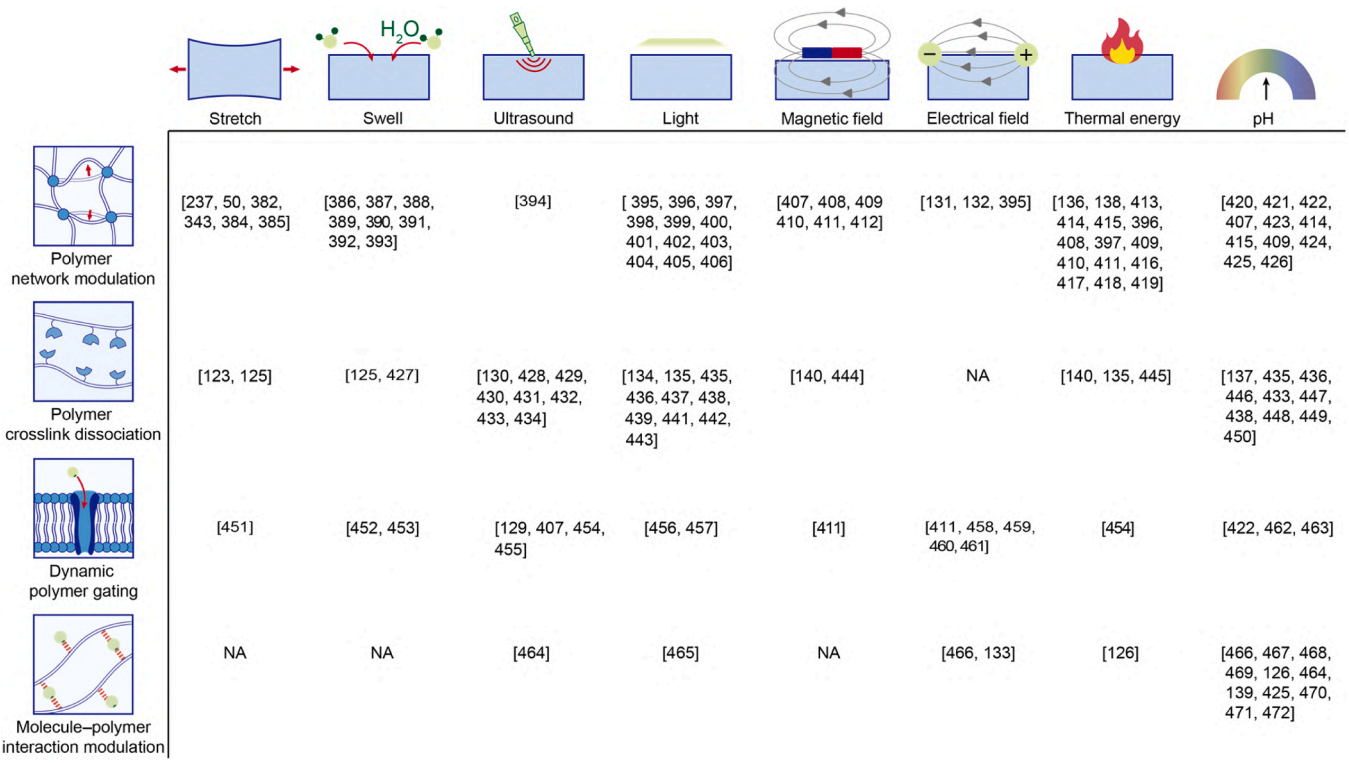
capturing microscopic dynamical heterogeneity. To explicitly identify the dominant transport regimes, researchers employ the non-Gaussian parameter and the van Hove self-correlation function (Fig. 20**C**), which straightforwardly illustrate the coexistence of slow (caged) and fast (hopping) particle populations [414,420,424]. Furthermore, the intermediate scattering function can be evaluated to capture the structural relaxation of the system (Fig. 20**D**). The extracted relaxation times often manifest complex dependencies on network parameters such as polymer strand flexibility [414].

Ultimately, these trajectory-derived observables are governed by the underlying energy landscape. By computing the spatial probability distribution of the penetrant or using enhanced sampling methods, the potential of mean force (PMF) can be extracted (Fig. 20**E**), which maps the effective free energy landscape with respect to a collective variable. This allows for the direct quantification of the hopping free energy barrier. Simulations have demonstrated that in semiflexible networks, the energy barrier possesses a non-monotonic dependence on polymer strand flexibility due to competition between the network's conformational entropy and its mechanical bending energy [414]. Furthermore, energetic analysis reveals that the barrier to transport is not merely deformation energy from loop stretching, but is significantly contributed by junction deviation [65].

9. Stimuli-Induced Mechano-Diffusion in Hydrogels

The foregoing discussion has established a mechanistic framework for understanding how external perturbations regulate transport in polymer networks by altering network geometry, interaction landscapes, and diffusion pathways. Building upon this foundation, we now turn to a major application domain in which these principles are actively leveraged: stimulus-responsive molecular release in hydrogels. In drug delivery systems, external stimuli—including mechanical loading, physical fields, and chemical environmental changes—are widely employed to regulate molecular diffusion and release. In many such systems, release modulation arises not simply from stimulus-triggered bulk response, but from stimulus-induced changes in polymer network structures, connectivity, or local molecule–polymer interactions. Consequently, molecular transport in these materials is often tightly coupled to network deformation or reconfiguration and can be interpreted within a broad mechano-diffusion framework. Despite this shared physical basis, existing studies are commonly organized according to stimulus type or material platform, emphasizing system-specific response behaviors. While informative, this structure obscures a direct comparison of transport-regulation mechanisms across systems, as common mechano-diffusion principles are scattered across otherwise disconnected studies. To provide a more unified and mechanism-oriented perspective, we therefore analyze stimulus-responsive molecular diffusion and release along two complementary but decoupled dimensions: external stimulation strategies, which describe how perturbations are imposed on polymer networks, and polymer-level transport-regulation mechanisms, which capture the fundamental origins of stimulus-induced changes in molecular transport (Fig. 21). By separating stimulus form from transport mechanism, this framework enables cross-stimulus and cross-material comparisons and helps identify transferable design principles for controlled molecular transport in polymer networks.

To establish a unified framework for stimulus-regulated molecular transport in polymer networks, we first classify existing studies according to the type of external stimulus applied. This stimulus-based categorization is motivated by the recognition that molecular release and transport are strongly regulated by externally imposed or environmentally derived triggers. The selected stimuli—including mechanical



	Stretch	Swell	Ultrasound	Light	Magnetic field	Electrical field	Thermal energy	pH
Polymer network modulation	[237, 50, 382, 343, 384, 385]	[386, 387, 388, 389, 390, 391, 392, 393]	[394]	[395, 396, 397, 398, 399, 400, 401, 402, 403, 404, 405, 406]	[407, 408, 409 410, 411, 412]	[131, 132, 395]	[136, 138, 413, 414, 415, 396, 408, 397, 409, 410, 411, 416, 417, 418, 419]	[420, 421, 422, 407, 423, 414, 415, 409, 424, 425, 426]
Polymer crosslink dissociation	[123, 125]	[125, 427]	[130, 428, 429, 430, 431, 432, 433, 434]	[134, 135, 435, 436, 437, 438, 439, 441, 442, 443]	[140, 444]	NA	[140, 135, 445]	[137, 435, 436, 446, 433, 447, 438, 448, 449, 450]
Dynamic polymer gating	[451]	[452, 453]	[129, 407, 454, 455]	[456, 457]	[411]	[411, 458, 459, 460, 461]	[454]	[422, 462, 463]
Molecule–polymer interaction modulation	NA	NA	[464]	[465]	NA	[466, 133]	[126]	[466, 467, 468, 469, 126, 464, 139, 425, 470, 471, 472]

Fig. 21. Overview of stimuli-responsive diffusion mechanisms in polymer networks. Summary of reported external stimuli and the corresponding polymeric mechanisms through which molecular diffusion and release are regulated in polymer networks.

deformation (stretching and swelling), physical fields (ultrasound, light, magnetic and electric fields), and thermodynamic or chemical cues (pH) — represent the dominant and practically accessible control modalities used to modulate transport and release in polymer-based delivery systems. Collectively, these stimuli define the control space through which kinetics, timing, and spatial selectivity can be programmed, making them a natural starting point for organizing stimulus-responsive drug delivery strategies. Building on the stimulus-based horizontal classification, we further organize the literature along a mechanistic axis that captures how external or environmental stimuli are transduced into changes in molecular transport within polymer networks. While stimuli define the mode of external control, their effects are realized through distinct response pathways governed by network architecture, crosslinking motifs, and molecule–polymer interactions. From this perspective, stimulus-induced transport modulation can be broadly understood in terms of polymer-network-level modulation, reversible restructuring of crosslinking domains, dynamic gating of transport pathways, and the regulation of molecule–polymer interactions. Together, these mechanistic pathways span responses from network-scale structural reorganization to molecular-scale interaction changes, enabling systematic comparison of transport and release behaviors across diverse stimulus conditions within a unified framework.

In stimulus-responsive polymer systems, polymer network modulation represents the most direct and widely encountered mechanism for regulating molecular transport [41,50,131,132,136,138,447–491]. Its defining feature lies in the ability of external or environmental stimuli to alter the structural state of the polymer network at the mesoscale, thereby directly reshaping diffusion pathways and release behavior. This mechanism does not rely on specific chemical reactions or molecular recognition events; instead, it operates through global changes in network geometry, chain conformation, effective mesh size, and free-volume distribution, which collectively modulate transport resistance. As is evident from the mechanism–stimulus matrix in Fig. 21, all classes of external stimuli can access this pathway, with optical, thermal, and pH-based triggers being particularly prominent. In these cases, molecular transport is regulated primarily through stimulus-induced network reorganization or volume evolution, rather than through specific interactions between the polymer matrix and the transported species. Owing to its structural, stimulus-agnostic nature, polymer network modulation constitutes the simplest and most general route for triggering diffusion and release in responsive polymer networks and forms a foundational physical framework for understanding stimulus-induced mechano-diffusion phenomena.

Beyond polymer network modulation, which is characterized by network-scale structural rearrangements, stimulus-responsive polymer systems also exhibit a distinct class of transport regulation mechanisms based on polymer crosslink dissociation [123–125,130,134,135,137, 140,492–515]. In this mechanism, external or environmental stimuli act directly on the network's connecting units, leading to changes in network connectivity and topology rather than through gradual geometric modulation. From a physicochemical perspective, crosslink dissociation commonly involves dynamic covalent bonds, coordination interactions, hydrogen bonding, ionic associations, or other supramolecular crosslinking motifs, whose stability can be weakened, reversibly or permanently disrupted, and reorganized upon stimulation. Crosslinking points play a central role in constraining chain mobility and maintaining network integrity, their dissociation is often accompanied by abrupt changes in effective crosslink density, chain length, and network constraints, resulting in step-like or threshold-dependent shifts in molecular transport behavior. Importantly, triggering crosslink dissociation generally requires either a substantial energy input or the deliberate design of responsive polymer architectures that allow external stimuli to couple selectively to the crosslinking domains. Therefore, this mechanism is most frequently realized under stimuli such as ultrasound, light irradiation, and pH modulation, which can efficiently target specific crosslinking interactions. These stimulus modalities enable controlled, stage-wise, or switch-like regulation of molecular diffusion and release, distinguishing crosslink dissociation–mediated mechano-diffusion from the more continuous transport modulation associated with network-level deformation.

In addition to the above-mentioned mechanisms, dynamic polymer gating represents a class of molecular transport-regulation mechanisms characterized by the spatiotemporally reversible opening and closing of transport pathways [129,472,476,516–528]. Unlike mechanisms that rely on global network deformation or changes in crosslink connectivity, dynamic gating does not require substantial alteration of the polymer network's overall geometry or topology. Instead, external or environmental stimuli induce localized conformational rearrangements, segmental reorientation, or reversible state switching of functional units, giving rise to transient and spatially confined transport channels. From a structural standpoint, this mechanism operates at an intermediate, mesoscopic scale, manifested as reversible modulation of local free volume, effective pore size, or transport energy barriers. Importantly, the scope of dynamic polymer gating is not restricted to the polymer matrix itself. In many delivery systems, gating behavior can occur both within the polymer carrier—where local channel dynamics regulate molecular diffusion—and within the surrounding biological tissue or target environment, where stimulus-induced changes in tissue microstructure, interstitial spacing, or barrier properties dynamically modulate molecular transport across interfaces. Under this mechanism, transport kinetics are governed not by bulk diffusivity or network connectivity, but by the probability, duration, and spatial distribution of gating events, leading to inherently non-steady and heterogeneous transport profiles. As a result, dynamic polymer gating is particularly suited for selective, pulsatile, or temporally programmable release and transport, and provides a mechanistic bridge between material-level design and dynamic regulation at biological interfaces.

Lastly, stimulus-responsive polymer systems also encompass a distinct pathway that operates directly at the molecular interaction level, referred to as molecule–polymer interaction modulation [126,133,139,491,529–538]. In this mechanism, external or environmental stimuli do not primarily alter the polymer network geometry, topology, or channel state; instead, they modulate the binding strength, interaction energy landscape, or association–dissociation kinetics between the transported molecules and the polymer matrix, thereby governing molecular mobility within the network. From a mechanistic perspective, this pathway represents the molecular-scale limit of stimulus-regulated transport, where diffusion and release behavior are dictated by interaction-mediated energetic barriers rather than by steric obstruction, network connectivity, or channel availability. Analysis of the reference distribution shown in Fig. 21 further reveals that examples based on molecule–polymer interaction modulation are comparatively sparse relative to the other three mechanism classes, with reported systems predominantly associated with pH-responsive conditions, while some stimulation modalities exhibit few or no clear examples. Importantly, this observation should not be interpreted as evidence that such mechanisms are fundamentally inaccessible under these stimuli. Rather, it reflects the higher design complexity and stricter requirements associated with selectively and reversibly coupling external stimuli to specific molecule–polymer interactions, while minimizing concurrent structural responses of the polymer network. Consequently, compared with structure-driven mechanisms, molecule–polymer interaction modulation has been less frequently adopted as a primary strategy for drug release, and is more often employed in contexts where chemical selectivity, payload specificity, or interaction-dominated transport behavior is the central design objective.

An integrated analysis of Fig. 21 indicates that the prevalence of different stimulus modalities in stimulus-responsive polymer transport studies is governed by a combination of implementation difficulty, controllability, and application-driven requirements. Thermal and pH-responsive stimuli constitute the largest fraction, largely because they function as relatively passive triggering mechanisms: in practical settings, drug-loaded polymer matrices can be deployed directly in vivo and activated by physiological temperature or local fluid pH, without the need for external instrumentation or complex operational procedures. By contrast, physical field–based stimuli—including light, magnetic fields, electric fields, and ultrasound—are supported by comparatively mature engineering technologies and offer externally controllable, spatially and temporally programmable regulation. These features make them widely adopted in systems requiring precise control over release behavior, albeit at the cost of increased system complexity. Swelling-mediated responses occupy a distinct position in the framework, as solvent uptake and volumetric expansion can naturally couple multiple environmental cues to transport regulation, particularly temperature and pH, thereby integrating different stimuli into a unified transport response. In comparison, mechanically induced stretching is represented by fewer reported examples, which likely reflect the practical challenges associated with precisely applying and maintaining controlled deformation under realistic delivery or in vivo conditions. Overall, the reference distribution trends observed in Fig. 21 are not determined solely by the intrinsic effectiveness of individual mechanisms, but instead reflect trade-offs between passive triggering and active control, design simplicity and regulatory precision, which collectively shape the dominant development pathways of stimulus-responsive molecular transport in polymer systems.

10. Mechano-diffusion of Active Particles in Hydrogels

Previous sections focused on passive particles, whose diffusion is driven by thermal fluctuations and can often be interpreted within equilibrium diffusion frameworks using effective diffusivity together with network descriptors. However, many real-world transport problems, particularly in biology, are dominated by active particles (e.g., flagellated bacteria [539–541], sperm cells [542–545], and flagellate microalgae [546–548]) whose diffusion arises from active self-propulsion mechanisms rather than passive Brownian motion [549,550]. Beyond biology, active particles are also central to emerging technologies such as soft microrobotics [551–554]. Their transport is fundamentally non-equilibrium, as persistent motion is sustained by continuous energy input, which in polymer networks couples strongly to geometric confinement and viscoelastic dissipation. Consequently, transport is jointly governed by particle activity (quantified by Péclet number, defined as the ratio of directed motion versus thermal diffusion), geometric confinement relative to the mesh size, and the network's mechanical compliance (e.g., bending stiffness) [555,556]. This interplay leads to distinct dynamical regimes as particle size approaches the pore scale. This section adopts a trajectory-based description to quantify swimming speed, directional persistence, and their distributions, thereby establishing a mechanistic bridge between single-particle motility, collective transport, and material design. We first clarify the conceptual distinction between passive and active particles (**Section 10.1**), then map representative active particles studied in polymeric environments (**Section 10.2**), and finally outline forward-looking design principles for hydrogels that regulate active-particle diffusion and selectivity (**Section 10.3**).

10.1. Distinction between Passive and Active Particles

Passive particles undergo Brownian diffusion driven by thermal fluctuations [557,558] (Fig. 22**A**). In the absence of external forcing, their trajectories show no intrinsic directional preference, and reorientation is frequent and random. In such equilibrium settings, diffusion is typically characterized by an effective diffusivity D and can often be interpreted within frameworks introduced in earlier chapters (e.g., size-ratio regimes and network descriptors).

In contrast, active particles are maintained out of equilibrium by continuous energy consumption [555] (Fig. 22**B**). Their "diffusion" at long times is not purely thermal; instead, it arises from self-propulsion (e.g., metabolic energy powering flagellar or ciliary beating [559]) or field-induced propulsion (e.g., magnetic, electric, optical, or chemically fueled mechanisms [560–562]). A defining feature is directional persistence over a finite time/length scale: trajectories remain

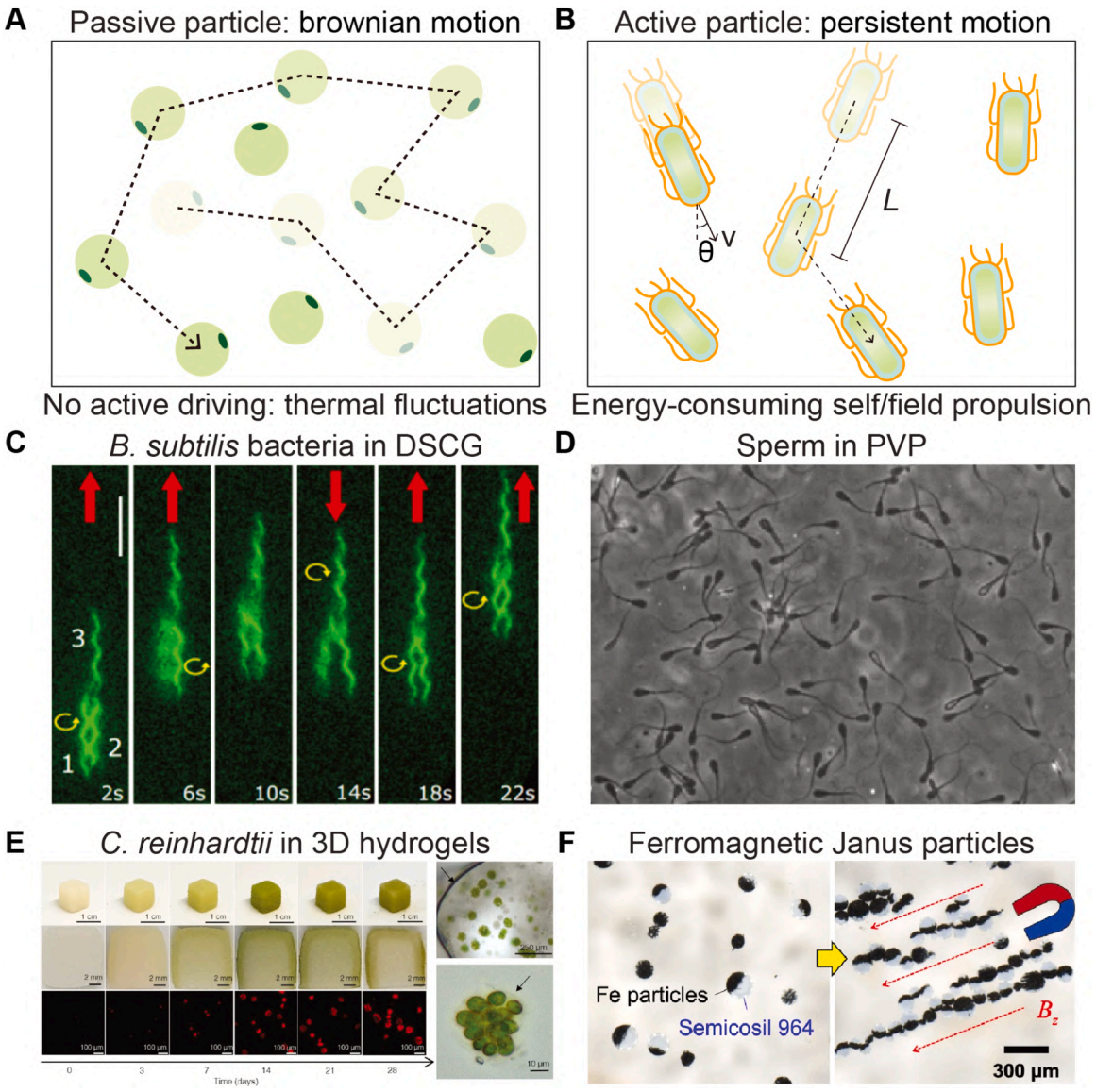


Fig. 22. Distinction between passive and active particles diffusion, and representative active particles in polymer networks. (A) Passive particle: Brownian motion driven solely by thermal fluctuations. In the absence of active driving, trajectories exhibit frequent random reorientations and no intrinsic directional persistence. (B) Active particle: Persistent motion powered by energy-consuming self-propulsion or field-induced propulsion. Trajectories maintain a preferred direction over a finite persistence time/length, characterized by an instantaneous velocity v and directionality θ, before undergoing stochastic reorientation. (C) Motile Bacillus subtilis bacteria with three flagellar bundles swimming in 18.75% DSCG (lyotropic, water-based disodium cromoglycate). 524 under a CC BY 4.0 license, APS. Scale bar: 5 μm. (D) Sperm cells swimming in a Newtonian viscous medium (3% PVP). 525 under a CC BY 4.0 license, Springer Nature. (E) Motile microalgae (Chlamydomonas reinhardtii) in 3D-printed hydrogel–based engineered living materials. 159 under a CC BY license, Wiley. (F) Synthetic active particles (ferromagnetic Janus particles), whose motion and interactions can be programmed by external fields to control propulsion direction/speed, alignment, and collective organization. 519 under a CC BY 4.0 license, Springer Nature.
(a) Adapted from Ref. (b) Adapted from Ref. (c) Adapted from ref. (d) Adapted from Ref.

approximately aligned for a persistence time τ_p (or a persistence length L), before stochastic reorientation events randomize the direction [563]. This distinction is illustrated schematically in Fig. 22**A** and 22**B,** where passive particles exhibit a random-walk-like trajectory dominated by thermal fluctuations, whereas active particles display persistent segments due to self/field propulsion.

Quantitatively, active motion can be parameterized by an instantaneous speed v and swimming orientation θ that remain correlated over τ_p [563]. At short times, motion can appear quasi-ballistic (approximately straight), while at long times repeated reorientation events yield an effective diffusive behavior. Because active propulsion requires sustained energy input, motility may also persist only over a finite duration, which we refer to as the motility lifetime T_{life} (e.g., fuel depletion, physiological changes, or removal of an external field). Notably, τ_p and T_{life} capture different aspects of active transport: τ_p quantifies how rapidly the swimming direction decorrelates, whereas T_{life} sets how long propulsion remains appreciable before weakening or ceasing. These timescales can be medium-dependent: in polymer networks, "activity" is often not a fixed property; it can depend on local confinement, viscoelastic loading, chemical microenvironments, or time-varying physiological states (for biological swimmers). In practice, a single diffusivity is often insufficient for active motion; instead, trajectories are more informatively described by the swimming speed v, orientation θ, persistence time τ_p, motility lifetime T_{life}, as well as how these quantities vary across particles and time.

Stretchable polymer networks add a further layer of coupling

because deformation reshapes the local microenvironment experienced by active swimmers: stretching can alter pore geometry and connectivity, induce microstructural anisotropy, and change viscoelastic dissipation pathways, thereby modulating propulsion efficiency, reorientation dynamics, and particle-network interactions. In this sense, stretchable hydrogels provide mechanical control handles for tuning the motility landscape underlying active diffusion.

10.2. Mechano-Diffusion of Active Particles in Polymer Networks

Active transport in polymer-rich, gel-like environments (mucus, extracellular matrix, biofilms, and engineered hydrogels) is strongly shaped by geometric confinement and viscoelastic dissipation, which can reshape motility statistics and can shift collective dynamics [564]. These effects are central in biological contexts (e.g., bacterial spreading and infection, sperm navigation and selection) and increasingly relevant to engineered functions (e.g., targeted delivery and microscale actuation). The literature therefore focuses on two main categories: biological swimmers and synthetic active particles, together spanning broad propulsion mechanisms and length scales.

10.2.1. Biological Active Particles

A common way to organize biological swimmers is by size scale, since particle length relative to pore or mesh size largely controls confinement and motility modes.

Motile bacteria. Motile bacteria such as *E. coli* and *B. subtilis* propel via rotating flagella bundles and are widely studied in polymeric and polymer-rich media relevant to infection, biofilm initiation, and penetration through mucus-like barriers. In polymer solutions and gel-like networks, their trajectories become sensitive to pore geometry, local anisotropy, and surface interactions, which can bias orientation dynamics and promote transitions among run-reorientation dynamics, intermittent trapping, and collective states. Fig. 22**C** shows motile *B. subtilis* in a lyotropic polymeric environment (DSCG) [565], illustrating how anisotropic microstructure can steer trajectories and, in turn, reshape transport statistics that matter for barrier crossing and colonization.

Sperm cells. Sperm transport in polymer-rich environments is central to reproductive biology and reflects a practical need for polymer- or gel-based media that can differentiate motility under realistic, mucus-like conditions. As a canonical flagellated swimmer, sperm consists of a head and a beating flagellum; in many studies the head is on the order of ~ 10 μm in length and ~ 5 μm in width with a flagellum tens of microns long (Fig. 22**D**) [566]. In viscous polymer solutions and gel-like mucus mimics, viscoelastic dissipation and confinement can reshape propulsion efficiency and turning behavior, thereby changing persistence and navigation performance. This sensitivity is why polymeric media are widely used to quantify how microstructure and rheology modulate sperm trajectories.

Motile microalgae. Biflagellate microalgae such as *Chlamydomonas reinhardtii* (*C. reinhardtii*) provide distinct kinematics and length scales that often approach the characteristic pore/mesh scales in 3D hydrogels, so steric confinement and pore connectivity can dominate migration. As shown in Fig. 22**E**, an individual *C. reinhardtii* cell is associated with a reported volume of 358 μm^3 [567]. (This corresponds to an effective cell scale on the order of ~ 10 μm.) Such organisms are therefore useful "active probes" for how 3D network connectivity and anisotropy regulate active transport, including intermittent obstruction, reorientation, and escape events.

10.2.2. Synthetic Active Particles

Alongside biological swimmers, synthetic active particles powered by chemical gradients or external fields offer tunable driving conditions and programmable particle designs. Two classification routes are commonly used: (i) propulsion arising from surface/chemical asymmetry (e.g., Janus swimmers) and (ii) propulsion arising from engineered body geometry or mechanics (e.g., rigid shape-designed swimmers and soft microrobotic swimmers).

Janus microswimmers (surface/chemical asymmetry-enabled). Janus particles carry an intrinsic asymmetry in composition or surface chemistry, which can be harnessed to generate propulsion through chemical reactions or external fields [560]. For example, Fig. 22**F** shows ferromagnetic Janus particles whose motion can be driven by an applied magnetic field. This platform is attractive because propulsion can be tuned by surface design and driving conditions while keeping the particle size and overall shape relatively simple, enabling systematic tests of how polymer microstructure modulates directionality, persistence, and collective organization.

Engineered microswimmers (geometry- and mechanics-enabled). Engineered microswimmers generate propulsion primarily through designed body geometry or controlled deformation. Rigid, shape-designed swimmers (e.g., helical swimmers) translate by rotating a designed geometry under an external field, offering a clean platform to isolate how confinement and anisotropy modulate swimming direction and speed [568,569]. Soft microrobotic swimmers rely on field-programmed deformation (flagella-like beating or body undulation), making their propulsion efficiency and reorientation especially sensitive to viscoelastic dissipation and mechanical constraints in polymer networks [570–572].

10.3. Engineering Polymer Network Architecture to Manipulate Active Particle Diffusion

While passive diffusion is primarily governed by steric exclusion between particles and the polymer mesh, active particles exhibit richer transport behaviors because self/field propulsion continuously couples to the network's confinement and viscoelastic dissipation. By engineering the architecture of stretchable hydrogels—through tuning key mesh and architecture descriptors (e.g., fibril orientation/spacing, reversible interactions, and topological defects) and applying macroscopic deformation—it becomes possible to regulate trajectory statistics (e.g., the probability distribution functions (PDFs) of v, θ, and L), moving beyond size-based filtering toward motility-based control and selection.

Macroscopic strain ε provides a direct route to break the isotropy and impose structural guidance. In an undeformed gel, a largely disordered microstructure offers no preferred direction, so the swimming orientation θ explores angles broadly over time. Under tensile loading, pore deformation and fibril alignment create an anisotropic environment that biases swimmer orientation, sharpening the orientation distribution toward a preferred direction θ_p (Fig. 23**A**). This effect is particularly relevant for elongated swimmers (e.g., *B. subtilis*, sperm), whose propulsion and steric interactions couple strongly with aligned microstructures.

Beyond directionality, confinement relative to mesh size modulates reorientation statistics and persistence. When the characteristic pore/mesh scale approaches the particle size, frequent encounters with the network can increase turning events, reducing the persistence time τ_p (or equivalently the persistence length $L \sim v\tau_p$) and reshaping the distributions of v, θ, and L extracted from trajectories (Fig. 23**A, left**). At elevated particle densities, the same confinement and anisotropy can also bias pair interactions and alignment, promoting collective states (swarming/clustering) that appear as multimodal PDFs of transport metrics (Fig. 23**A, right**).

These relationships between strain, geometry, and motility motivate the inverse-design framework illustrated in Fig. 23**B**. Rather than optimizing a single averaged metric, inverse-designed hydrogels target distributional signatures of transport: for a single particle type, the aim is to narrow the PDFs of mobility- and persistence-related quantities (reduced FWHM), whereas for mixed populations the aim is to enlarge peak-to-peak separation among their distributions. Even when different active particles have similar sizes, their motility signatures (speed,

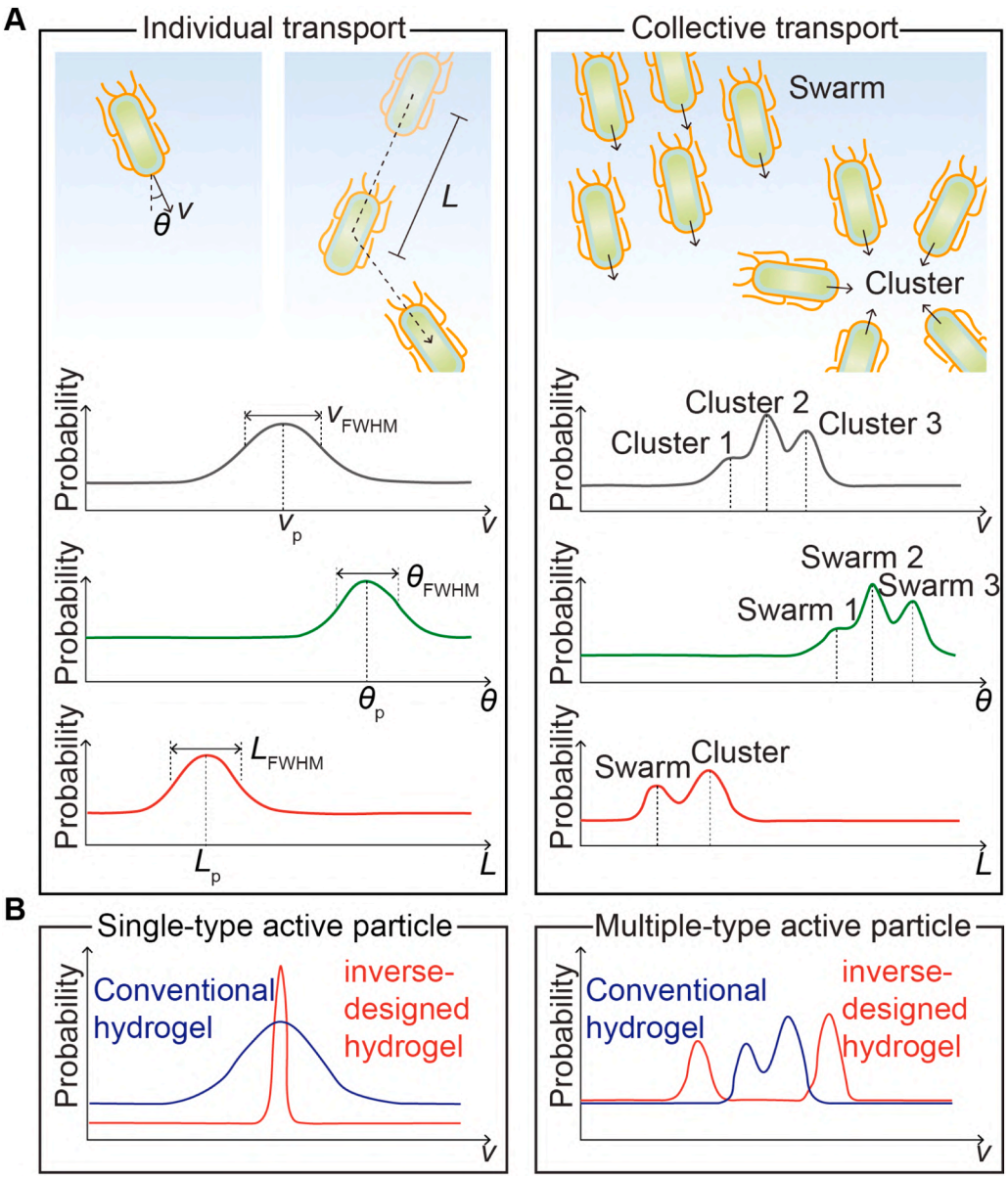


Fig. 23. Quantitative characterization of active particle diffusion and inverse-design principles for hydrogel-based regulation. (A) Schematic illustration of individual (left) versus collective (right) active-particle transport in polymer networks. For individual transport, the instantaneous velocity v, directionality θ, and persistence length L are quantified from single-particle trajectories. Their probability distribution functions (PDFs) typically exhibit single peaks, characterized by the peak values (v_p, θ_p, L_p) and the corresponding full widths at half maximum (v_{FWHM}, θ_{FWHM}, L_{FWHM}), reflecting characteristic motility and its variability. In collective regimes, PDFs can become multimodal, reflecting distinct dynamic states such as swarming and clustering; each mode can be associated with a specific collective state (e.g., Cluster 1–3, Swarm 1–3). (B) Inverse-design concept for amplifying transport selectivity in hydrogels. Relative to a conventional hydrogel, inverse-designed hydrogels can (left) narrow the distribution for a single particle type (reduced FWHM), yielding more uniform and controllable transport, and (right) increase the separation among distributions of different particle types (enhanced peak-to-peak contrast), enabling multi-modal discrimination and selection based on transport metrics.

persistence, and orientation statistics) can differ; engineered hydrogels can amplify these differences and enable robust sorting based on trajectory statistics rather than pore-size filtering alone.

11. Application and Outlook

In the preceding discussion, molecular transport has been framed as a tunable process governed by polymer network accessibility and the associated transport regimes, with external stimuli acting as modulators. When this physical perspective is translated into practical systems, diffusion ceases to be a fixed material property and instead becomes a functional variable that can be systematically engineered and regulated. Across diverse application contexts, controlling network architecture, accessibility, and their dynamic responses enables direct reconfiguration of transport pathways and flux distributions, thereby imparting specific functional outcomes. From this viewpoint, stimulus-responsive hydrogels and related soft materials emerge as a versatile platform for translating transport modulation into functional outcomes.

Here we leverage three representative application examples to highlight the design principles of mechano-diffusion in polymer networks. The first example, within the conceptual framework that treats molecular transport as a tunable process, selectively regulating molecular accessibility to functional interfaces emerges as a key design strategy for achieving reliable in situ biosensing [573–575]. In situ

biosensing offers distinct advantages, including real-time signal acquisition, minimal sample preprocessing, and the ability to perform continuous monitoring directly within physiological environments, making it highly attractive for diagnostic and health-monitoring applications [575–577]. In fact, complex biological fluids typically contain a large abundance of non-target biomolecules that can undergo nonspecific adsorption at the sensing interface, leading to biofouling (Fig. 24**A upper**) [578,579]. Such fouling competitively occupies interfacial accessibility, impedes effective contact between target biomarkers and the sensing element, and ultimately compromises detection accuracy and reliability. From a transport perspective, this challenge is not solely rooted in insufficient molecular recognition, but rather reflects a lack of effective differentiation in transport pathways and accessibility among coexisting molecular species prior to reaching the sensing interface. A broadly applicable strategy to address this issue is the introduction of a thin, selectively permeable hydrogel membrane upstream of the sensing surface, such that molecular transport is regulated before molecules encounter the sensing element. Existing studies have demonstrated that hydrogel-based permeation layers can achieve molecular discrimination through mechanisms such as size exclusion, charge-mediated interactions, and other weak physicochemical interactions (Fig. 24**A lower**) [580–583]. Building on these approaches, incorporating dynamic bonding as an additional network design dimension provides a distinct route for selective transport modulation. By embedding reversible interaction sites within the polymer network that transiently associate with target biomolecules, preferential and time-dependent transport pathways can be established. In this manner, target molecules are guided to permeate the hydrogel matrix and progressively reach the sensing interface, while non-target species lacking corresponding interactions are effectively excluded. This application illustrates that selective biosensing need not rely exclusively on the intrinsic specificity of sensing elements, but can instead be achieved through deliberate regulation of molecular accessibility and transport pathways at interfaces, offering a generalizable strategy for robust in situ detection in complex biological environments.

Second, within the conceptual framework that treats molecular transport as a tunable process, external stimuli provide a direct and effective means to impose spatiotemporal selectivity on molecular transport, a requirement that is particularly critical in drug delivery applications [584,585]. In complex physiological environments, conventional drug delivery systems often suffer from continuous leakage, off-target diffusion, and limited control over release timing, which collectively reduce therapeutic efficacy and increase the risk of side effects [586–588]. From a transport perspective, drug release is not merely a matter of cargo loading and passive diffusion, but fundamentally corresponds to whether—and when—drug molecules are permitted to overcome polymer network constraints and transition into the surrounding environment. External stimuli enable dynamic reconfiguration of polymer network structure and accessibility without altering the overall chemical composition of the material, thereby allowing reversible switching between distinct transport regimes and providing a physical basis for on-demand release [495]. Among various stimulus modalities, ultrasound has been widely employed in hydrogel-based drug delivery systems due to its noninvasive nature, spatial addressability, and precise temporal controllability, leading to relatively mature strategies for triggered release and diffusion enhancement [495,589]. In most existing studies, ultrasound is primarily treated as a switch or diffusion accelerator, with its effects manifested as a largely nonselective increase in network accessibility [495,590,591]. Under this paradigm, activation of ultrasound typically results in the simultaneous release of all diffusible species, offering limited discrimination among different molecular cargos. By contrast, integrating polymer network design and molecular transport considerations into ultrasound-responsive systems opens an underexplored avenue for achieving stimulus-driven selective permeability [592]. Through the coordinated tuning of network geometry, molecule–network interactions, and ultrasound parameters (e.g., intensity, frequency, and actuation sequence), it becomes possible to differentially regulate transport pathways such that specific molecules are preferentially permitted to permeate under defined stimulus conditions, while others

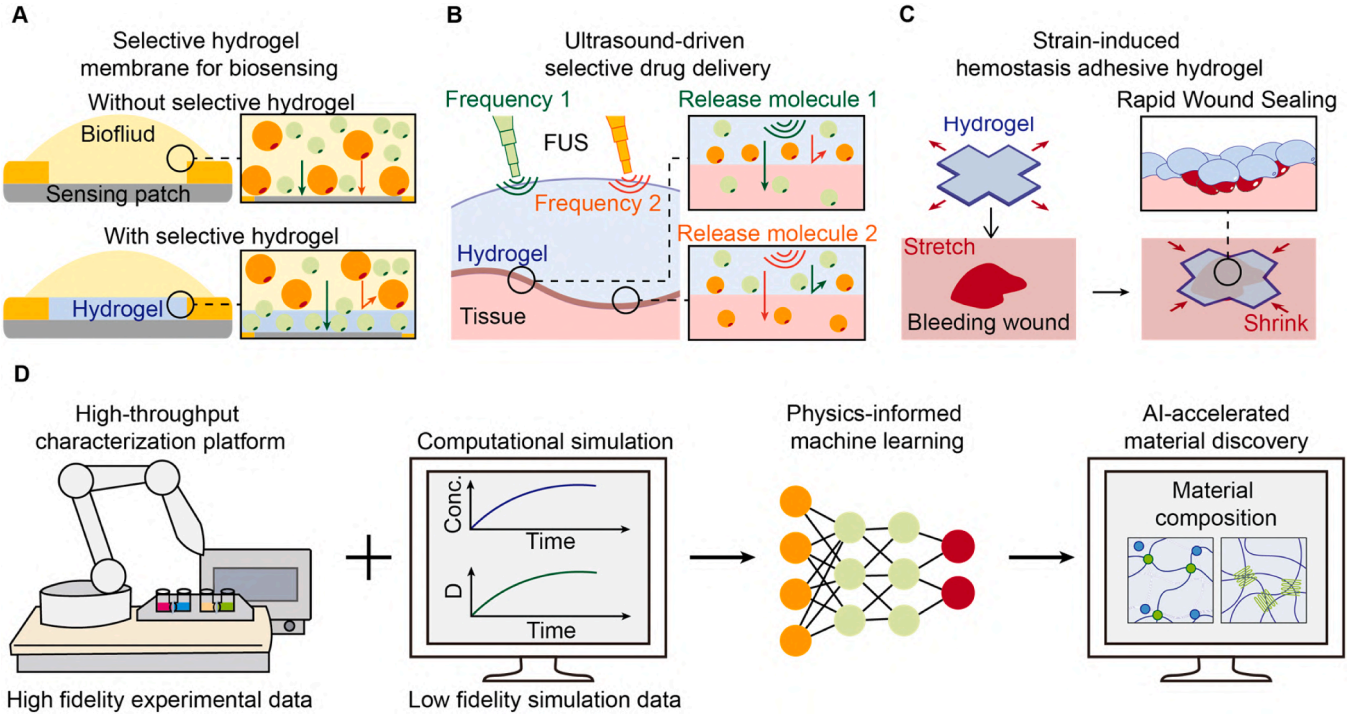


Fig. 24. Applications and outlook of mechano-diffusion. Representative applications enabled by mechano-diffusion, including (A) selective hydrogel membranes for in situ biosensing, (B) ultrasound-driven selective drug delivery, and (C) strain-induced hemostatic adhesive hydrogels. (D) Outlook toward AI-accelerated mechano-diffusive material design through the integration of high-throughput characterization, computational simulation, and physics-informed machine learning.

remain restricted, or even to reversibly switch transport selectivity across different stimulus states (Fig. 24**B**). Taken together, ultrasound-driven drug delivery can be extended beyond binary release triggering toward programmable control over transport pathways, enabling drug release that is selectively regulated across spatial, temporal, and dosage dimensions, and offering expanded design flexibility for multicomponent delivery and complex therapeutic scenarios.

Finally, within the broader landscape of transport regulation, mechanical deformation offers a uniquely direct and rapid means of modulating molecular and fluid transport, particularly in biomedical scenarios where interface transport must be suppressed on short time scales [593]. As a class of biocompatible soft materials, hydrogels have been widely explored for wound management and tissue repair [594–596]. Their porous polymer networks can rapidly sequester and immobilize hemostatic agents at the wound interface, forming a physical barrier that effectively limits uncontrolled fluid and molecular outflow and thereby enables rapid hemostasis [597,598]. Beyond this passive role, hydrogels provide a versatile structural platform for integrating mechanical responsiveness with transport regulation to actively support subsequent stages of wound healing. By tailoring the mechanical properties of the polymer network, hydrogels can be applied to wounds in a pre-strained state, exploiting their elastic recovery to exert a sustained inward contractile force as the material relaxes toward its equilibrium configuration [599,600]. This mechanically induced contraction promotes wound edge approximation and accelerates tissue closure without relying on external fixation. In parallel, the intrinsic capability of hydrogels to serve as drug delivery matrices enables further coupling between mechanical deformation and molecular transport. Strain-induced network reconfiguration can be leveraged to regulate the release of therapeutic agents at the wound site, such that mechanical deformation not only assists physical closure but also modulates local drug availability (Fig. 24**C**). Through this multiscale coupling of mechanical response and transport behavior, hydrogels transition from passive wound dressings to active, mechano-responsive systems that simultaneously support rapid hemostasis, mechanical wound closure, and localized drug delivery. This integrated design paradigm highlights how mechanically driven modulation of network accessibility and transport pathways can be harnessed to achieve efficient and multifunctional wound-healing outcomes [599–601].

Taken together, the applications discussed above demonstrate that mechano-diffusion and transport regulation can be deliberately leveraged across diverse functional contexts, rather than being confined to specific materials or isolated use cases. Building on these advances, the research perspective naturally extends toward the systematic exploration, comparison, and design of transport behaviors across polymer networks and external stimuli at larger scales [602]. In this context, the integration of high-throughput experimentation, computational simulation, and data-driven modeling is emerging as a particularly promising direction (Fig. 24**D**) [603,604]. High-throughput experimental platforms enable continuous and efficient acquisition of large volumes of high-fidelity transport data, capturing diffusion and transport behaviors in complex polymer networks under realistic conditions [603,605]. In parallel, computational simulations provide cost-effective access to broader parameter spaces, generating complementary datasets that extend beyond experimentally accessible regimes [602]. By combining these experimental and simulation datasets within physics-informed machine learning frameworks, it becomes possible to construct scalable databases that explicitly link network structure, stimulus conditions, and transport behavior [606,607]. Such databases, in turn, enable a shift in material design strategy: rather than relying on empirical screening or incremental optimization, materials can be designed starting from desired transport behaviors—such as prescribed release profiles, selective permeability, or transport regime switching—and working backward to identify appropriate polymer architectures, material compositions, and processing conditions [608–610]. Looking ahead, this transport-centric, data-driven approach has the potential to substantially accelerate the discovery of mechano-diffusive materials and to enable genuinely programmable and predictable molecular transport systems.

CRediT authorship contribution statement

Zhaohan Yu: Writing – review & editing, Writing – original draft, Visualization, Methodology, Investigation. **Tsz Hung Wong:** Writing – review & editing, Writing – original draft, Visualization, Validation, Methodology, Formal analysis, Conceptualization. **Chuwei Ye:** Writing – review & editing, Writing – original draft, Visualization, Methodology, Investigation. **Xinzhe Dai:** Writing – review & editing, Writing – original draft, Visualization, Methodology, Investigation, Formal analysis, Data curation. **Jie Ma:** Writing – review & editing, Writing – original draft, Visualization, Validation, Methodology, Investigation, Conceptualization. **Shaoting Lin:** Writing – review & editing, Supervision, Project administration, Funding acquisition, Conceptualization. **Jingjie Yeo:** Writing – review & editing, Supervision, Project administration, Funding acquisition, Conceptualization.

Declaration of Competing Interest

The authors declare the following financial interests/personal relationships which may be considered as potential competing interests: Shaoting Lin reports financial support was provided by National Science Foundation. Jingjie Yeo reports financial support was provided by National Science Foundation. If there are other authors, they declare that they have no known competing financial interests or personal relationships that could have appeared to influence the work reported in this paper.

Acknowledgments

S.L. thanks the support form the US National Science Foundation (CMMI−2338747), the US National Science Foundation (CBET−2320716), the US National Science Foundation (CMMI−2516178), and the American Chemical Society Petroleum Research Fund through grant PRF 69156-DNI9. J.Y. thanks the support from the US National Science Foundation (CMMI−2338518).

Data availability

Data will be made available on request.

References

[1] I. Levental, P.C. Georges, P.A. Janmey, Soft biological materials and their impact on cell function, Soft Matter 3 (2007) 299–306.
[2] Z. Xu, et al., Simulating transport of soft matter in micro/nano channel flows with dissipative particle dynamics, Adv. Theory Simul. 2 (2019) 1800160.
[3] J.P. Best, Y. Yan, F. Caruso, The role of particle geometry and mechanics in the biological domain, Adv. Healthc. Mater. 1 (2012) 35–47.
[4] L. Hokin, M. Hokin, Biological transport, Annu. Rev. Biochem. 32 (1963) 553–578.
[5] M. Kojic, et al., Transport in biological systems, J. Serb. Soc. Comp. Mech. 5 (2011) 101–128.
[6] A. Tsuda, F.S. Henry, J.P. Butler, Particle transport and deposition: basic physics of particle kinetics, Compr. Physiol. 3 (2013) 1437–1471.
[7] D.R. Gaskell, M.J.M. Krane, An introduction to transport phenomena in materials engineering, CRC Press, 2024.
[8] G. Michaud, C. Proffitt, Particle transport processes. International Astronomical Union Colloquium, Cambridge University Press, 1993, pp. 246–259.
[9] A. Imdakm, M. Sahimi, Computer simulation of particle transport processes in flow through porous media, Chem. Eng. Sci. 46 (1991) 1977–1993.
[10] M. Iguchi, O.J. Ilegbusi, Basic transport phenomena in materials engineering, Springer, 2014.
[11] M. Gomez-Florit, et al., Natural-based hydrogels for tissue engineering applications, Molecules 25 (2020) 5858.
[12] N.H. Thang, T.B. Chien, D.X. Cuong, Polymer-based hydrogels applied in drug delivery: an overview, Gels 9 (2023) 523.
[13] E. Prince, E. Kumacheva, Design and applications of man-made biomimetic fibrillar hydrogels, Nat. Rev. Mater. 4 (2019) 99–115.

[14] S. Nayak, L.A. Lyon, Soft nanotechnology with soft nanoparticles, Angew. Chem. Int. Ed. 44 (2005) 7686–7708.
[15] D. Chenthamara, et al., Therapeutic efficacy of nanoparticles and routes of administration, Biomater. Res. 23 (2019) 20.
[16] A.S. Hoffman, The origins and evolution of "controlled" drug delivery systems, J. Control. Release 132 (2008) 153–163.
[17] K. Park, Controlled drug delivery systems: past forward and future back, J. Control. Release 190 (2014) 3–8.
[18] S. Adepu, S. Ramakrishna, Controlled drug delivery systems: current status and future directions, Molecules 26 (2021) 5905.
[19] L. Robeson, W. Burgoyne, M. Langsam, A. Savoca, C. Tien, High performance polymers for membrane separation, Polymer 35 (1994) 4970–4978.
[20] S. Semenova, Polymer membranes for hydrocarbon separation and removal, J. Membr. Sci. 231 (2004) 189–207.
[21] L.M. Robeson, Polymer membranes for gas separation, Curr. Opin. Solid. State Mater. Sci. 4 (1999) 549–552.
[22] J. Mathew-Krotz, K. Shea, Imprinted polymer membranes for the selective transport of targeted neutral molecules, J. Am. Chem. Soc. 118 (1996) 8154–8155.
[23] B.A. Van Setten, M. Makkee, J.A. Moulijn, Science and technology of catalytic diesel particulate filters, Catal. Rev. 43 (2001) 489–564.
[24] H. Liu, et al., Progress on particulate matter filtration technology: basic concepts, advanced materials, and performances, Nanoscale 12 (2020) 437–453.
[25] B.E. Logan, Environmental transport processes, John Wiley & Sons, 2012.
[26] L.M. McDowell-Boyer, J.R. Hunt, N. Sitar, Particle transport through porous media, Water Resour. Res. 22 (1986) 1901–1921.
[27] Y. Ouyang, D. Shinde, R. Mansell, W. Harris, Colloid-enhanced transport of chemicals in subsurface environments: A review, Crit. Rev. Environ. Sci. Technol. 26 (1996) 189–204.
[28] J. Witten, K. Ribbeck, The particle in the spider's web: transport through biological hydrogels, Nanoscale 9 (2017) 8080–8095.
[29] J. Zachara, et al., Internal domains of natural porous media revealed: critical locations for transport, storage, and chemical reaction, Environ. Sci. & Technol. 50 (2016) 2811–2829.
[30] S. Pawłowska, T. Kowalewski, F. Pierini, Fibrous polymer nanomaterials for biomedical applications and their transport by fluids: An overview, Soft Matter 14 (2018) 8421–8444.
[31] S.R. Nagel, Experimental soft-matter science, Rev. Mod. Phys. 89 (2017) 025002.
[32] I. Hamley, Nanotechnology with soft materials, Angew. Chem. Int. Ed. 42 (2003) 1692–1712.
[33] R. Brighenti, Y. Li, F.J. Vernerey, Smart polymers for advanced applications: a mechanical perspective review, Front. Mater. 7 (2020) 196.
[34] A. Tuteja, M.E. Mackay, S. Narayanan, S. Asokan, M.S. Wong, Breakdown of the continuum Stokes– Einstein relation for nanoparticle diffusion, Nano Lett. 7 (2007) 1276–1281.
[35] G. Batchelor, Brownian diffusion of particles with hydrodynamic interaction, J. Fluid. Mech. 74 (1976) 1–29.
[36] J. Renn, Einstein's invention of Brownian motion, Ann. der Phys. 517 (2005) 23–37.
[37] M.J. Webber, M.W. Tibbitt, Dynamic and reconfigurable materials from reversible network interactions, Nat. Rev. Mater. 7 (2022) 541–556.
[38] S. Hackelbusch, T. Rossow, P. van Assenbergh, S. Seiffert, Chain dynamics in supramolecular polymer networks, Macromolecules 46 (2013) 6273–6286.
[39] Y. Gu, J. Zhao, J.A. Johnson, Polymer networks: from plastics and gels to porous frameworks, Angew. Chem. Int. Ed. 59 (2020) 5022–5049.
[40] M. Yu, et al., Rapid transport of deformation-tuned nanoparticles across biological hydrogels and cellular barriers, Nat. Commun. 9 (2018) 2607.
[41] C. Ye, et al., Mechano-diffusion of Particles in Stretchable Hydrogels, Soft Matter (2025).
[42] A.C. Daly, L. Riley, T. Segura, J.A. Burdick, Hydrogel microparticles for biomedical applications, Nat. Rev. Mater. 5 (2020) 20–43.
[43] M.M. Caruso, et al., Mechanically-induced chemical changes in polymeric materials, Chem. Rev. 109 (2009) 5755–5798.
[44] X. Zhao, A theory for large deformation and damage of interpenetrating polymer networks, J. Mech. Phys. Solids 60 (2012) 319–332.
[45] X. Li, W. Wu, J. Wang, Y. Duan, The swelling behavior and network parameters of guar gum/poly (acrylic acid) semi-interpenetrating polymer network hydrogels, Carbohydr. Polym. 66 (2006) 473–479.
[46] N.R. Richbourg, N.A. Peppas, The swollen polymer network hypothesis: Quantitative models of hydrogel swelling, stiffness, and solute transport, Progress. Polym. Sci. 105 (2020) 101243.
[47] S.J. Kim, S.J. Park, S.I. Kim, Swelling behavior of interpenetrating polymer network hydrogels composed of poly (vinyl alcohol) and chitosan, React. Funct. Polym. 55 (2003) 53–59.
[48] T.H. Wong, J. Ma, Z. Sherburne, S. Lin, Diffusion and Release of Molecules in Swelling Polymer Networks, Extrem. Mech. Lett. (2026) 102466.
[49] Y. Sun, L.-G. Chen, X.-M. Fan, J.-L. Pang, Ultrasound responsive smart implantable hydrogels for targeted delivery of drugs: reviewing current practices, Int. J. Nanomed. (2022) 5001–5026.
[50] C. Ye, S. Lin, A mechano-diffusion characterization platform for probing strain-programmable nanoparticle diffusion in hydrogels, MRS Commun. 14 (2024) 919–926.
[51] L.-H. Cai, S. Panyukov, M. Rubinstein, Hopping diffusion of nanoparticles in polymer matrices, Macromolecules 48 (2015) 847–862.
[52] K. Saalwächter, S. Seiffert, Dynamics-based assessment of nanoscopic polymer-network mesh structures and their defects, Soft Matter 14 (2018) 1976–1991.
[53] T. Ge, Scaling perspective on dynamics of nanoparticles in polymers: length-and time-scale dependent nanoparticle–polymer coupling, Macromolecules 56 (2023) 3809–3837.
[54] J. Liu, S. Lin, Strain-engineered particle diffusion in uniaxially deformed polymer networks, J. Mech. Phys. Solids 191 (2024) 105732.
[55] P.J. Moncure, Z.C. Simon, J.E. Millstone, J.E. Laaser, Relationship between gel mesh and particle size in determining nanoparticle diffusion in hydrogel nanocomposites, J. Phys. Chem. B 126 (2022) 4132–4142.
[56] L. Jiang, S. Granick, Real-space, in situ maps of hydrogel pores, ACS nano 11 (2017) 204–212.
[57] B. Amsden, An obstruction-scaling model for diffusion in homogeneous hydrogels, Macromolecules 32 (1999) 874–879.
[58] F. Burla, T. Sentjabrskaja, G. Pletikapic, J. Van Beugen, G.H. Koenderink, Particle diffusion in extracellular hydrogels, Soft Matter 16 (2020) 1366–1376.
[59] C. Xu, et al., Mechanical regulation of polymer gels, Chem. Rev. 124 (2024) 10435–10508.
[60] M.A. Maier, F. dos Santos Adrego, S.A. Jung, A.M. Boos, A. Pich, Mechano-Triggered Release of Biomolecules from Supramolecular Hyaluronic Acid Hydrogels, ACS Appl. Polym. Mater. 6 (2024) 13841–13854.
[61] P. Ma, et al., Recent advances in mechanical force-responsive drug delivery systems, Nanoscale Adv. 4 (2022) 3462–3478.
[62] E. Axpe, et al., A multiscale model for solute diffusion in hydrogels, Macromolecules 52 (2019) 6889–6897.
[63] Z.E. Dell, K.S. Schweizer, Theory of localization and activated hopping of nanoparticles in cross-linked networks and entangled polymer melts, Macromolecules 47 (2014) 405–414.
[64] J. Hansing, R.R. Netz, Hydrodynamic Effects on Particle Diffusion in Polymeric Hydrogels with Steric and Electrostatic Particle–Gel Interactions, Macromolecules 51 (2018) 7608–7620.
[65] Y. Lu, X.-Y. Liu, G.-H. Hu, Double-Spring Model for Nanoparticle Diffusion in a Polymer Network, Macromolecules 55 (2022) 4548–4556.
[66] X. Di, et al., Cellular mechanotransduction in health and diseases: from molecular mechanism to therapeutic targets, Signal. Transduct. Target. Ther. 8 (2023) 282.
[67] E.K. Pillai, K. Franze, Mechanics in the nervous system: From development to disease, Neuron 112 (2024) 342–361.
[68] I. Constantinou, E.E. Bastounis, Cell-stretching devices: advances and challenges in biomedical research and live-cell imaging, Trends Biotechnol. 41 (2023) 939–950.
[69] K.A. Jansen, et al., A guide to mechanobiology: Where biology and physics meet, Biochimica et Biophysica Acta (BBA)-Molecular Cell Research 1853 (2015) 3043–3052.
[70] M.N. Starodubtseva, Mechanical properties of cells and ageing, Ageing Res. Rev. 10 (2011) 16–25.
[71] A. Navis, M. Bagnat, Developing pressures: fluid forces driving morphogenesis, Curr. Opin. Genet. & Dev. 32 (2015) 24–30.
[72] K. Goodwin, C.M. Nelson, Mechanics of development, Dev. Cell. 56 (2021) 240–250.
[73] N. Felsenthal, E. Zelzer, Mechanical regulation of musculoskeletal system development, Development 144 (2017) 4271–4283.
[74] F. Boselli, J.B. Freund, J. Vermot, Blood flow mechanics in cardiovascular development, Cell. Mol. Life Sci. 72 (2015) 2545–2559.
[75] W. Yao, Y. Li, G. Ding, Interstitial fluid flow: the mechanical environment of cells and foundation of meridians, Evid. -Based Complement. Altern. Med. 2012 (2012) 853516.
[76] R.M. Gilbert, J.T. Morgan, E.S. Marcin, J.P. Gleghorn, Fluid mechanics as a driver of tissue-scale mechanical signaling in organogenesis, Curr. Pathobiol. Rep. 4 (2016) 199–208.
[77] G.A. Holzapfel, J.D. Humphrey, R.W. Ogden, Biomechanics of soft biological tissues and organs, mechanobiology, homeostasis and modelling, J. R. Soc. Interface 22 (2025).
[78] J.M. Rutkowski, M.A. Swartz, A driving force for change: interstitial flow as a morphoregulator, Trends Cell. Biol. 17 (2007) 44–50.
[79] J.B. Freund, J.G. Goetz, K.L. Hill, J. Vermot, Fluid flows and forces in development: functions, features and biophysical principles, Development 139 (2012) 1229–1245.
[80] A.R. Jackson, W.Y. Gu, Transport properties of cartilaginous tissues, Curr. Rheumatol. Rev. 5 (2009) 40–50.
[81] H.T. Nia, L. Han, Y. Li, C. Ortiz, A. Grodzinsky, Poroelasticity of cartilage at the nanoscale, Biophys. J. 101 (2011) 2304–2313.
[82] G.W. Greene, et al., Changes in pore morphology and fluid transport in compressed articular cartilage and the implications for joint lubrication, Biomaterials 29 (2008) 4455–4462.
[83] B. Sun, The mechanics of fibrillar collagen extracellular matrix, Cell. Rep. Phys. Sci. 2 (2021).
[84] S.P. Fritton, S. Weinbaum, Fluid and solute transport in bone: flow-induced mechanotransduction, Annu. Rev. Fluid. Mech. 41 (2009) 347–374.
[85] P.A. Netti, D.A. Berk, M.A. Swartz, A.J. Grodzinsky, R.K. Jain, Role of extracellular matrix assembly in interstitial transport in solid tumors, Cancer Res. 60 (2000) 2497–2503.
[86] E. Syková, C. Nicholson, Diffusion in brain extracellular space, Physiol. Rev. 88 (2008) 1277–1340.
[87] X. He, et al., Extracellular matrix physical properties govern the diffusion of nanoparticles in tumor microenvironment, Proc. Natl. Acad. Sci. 120 (2023) e2209260120.

[88] K.L. Kleinhans, L.M. Jaworski, M.M. Schneiderbauer, A.R. Jackson, Effect of static compressive strain, anisotropy, and tissue region on the diffusion of glucose in meniscus fibrocartilage, J. Biomech. Eng. 137 (2015) 101004.
[89] L.T. Baxter, R.K. Jain, Transport of fluid and macromolecules in tumors. I. Role of interstitial pressure and convection, Microvasc. Res. 37 (1989) 77–104.
[90] T. Stylianopoulos, et al., Causes, consequences, and remedies for growth-induced solid stress in murine and human tumors, Proc. Natl. Acad. Sci. 109 (2012) 15101–15108.
[91] H.T. Nia, et al., Solid stress and elastic energy as measures of tumour mechanopathology, Nat. Biomed. Eng. 1 (2016) 0004.
[92] R.K. Jain, J.D. Martin, T. Stylianopoulos, The role of mechanical forces in tumor growth and therapy, Annu. Rev. Biomed. Eng. 16 (2014) 321–346.
[93] T. Stylianopoulos, L.L. Munn, R.K. Jain, Reengineering the physical microenvironment of tumors to improve drug delivery and efficacy: from mathematical modeling to bench to bedside, Trends Cancer 4 (2018) 292–319.
[94] S. Villarruel, G.S. Ibbott, S.J. Lai-Fook, Effect of concentration and hydration on restriction of albumin by lung interstitium, Microvasc. Res. 63 (2002) 27–40.
[95] C.-H. Heldin, K. Rubin, K. Pietras, A. Östman, High interstitial fluid pressure—an obstacle in cancer therapy, Nat. Rev. Cancer 4 (2004) 806–813.
[96] E. Henke, R. Nandigama, S. Ergün, Extracellular matrix in the tumor microenvironment and its impact on cancer therapy, Front. Mol. Biosci. 6 (2020) 160.
[97] R.K. Jain, T. Stylianopoulos, Delivering nanomedicine to solid tumors, Nat. Rev. Clin. Oncol. 7 (2010) 653–664.
[98] M. Li, Y. Zhang, Q. Zhang, J. Li, Tumor extracellular matrix modulating strategies for enhanced antitumor therapy of nanomedicines, Mater. Today Bio 16 (2022) 100364.
[99] Y. Zhang, et al., Mechanical forces in the tumor microenvironment: roles, pathways, and therapeutic approaches, J. Transl. Med. 23 (2025) 313.
[100] C. Wang, G. Ramahdita, G. Genin, N. Huebsch, Z. Ma, Dynamic mechanobiology of cardiac cells and tissues: Current status and future perspective, Biophys. Rev. 4 (2023).
[101] M.J. Davis, S. Earley, Y.-S. Li, S. Chien, Vascular mechanotransduction, Physiol. Rev. 103 (2023) 1247–1421.
[102] B. O'hara, J. Urban, A. Maroudas, Influence of cyclic loading on the nutrition of articular cartilage, Ann. Rheum. Dis. 49 (1990) 536–539.
[103] R.C. Evans, T.M. Quinn, Dynamic compression augments interstitial transport of a glucose-like solute in articular cartilage, Biophys. J. 91 (2006) 1541–1547.
[104] L. Zhang, A. Szeri, Transport of neutral solute in articular cartilage: effects of loading and particle size, Proc. R. Soc. A Math. Phys. Eng. Sci. 461 (2005) 2021–2042.
[105] S.L. Sampson, M. Sylvia, A.J. Fields, Effects of dynamic loading on solute transport through the human cartilage endplate, J. Biomech. 83 (2019) 273–279.
[106] X. Jiang, et al., Curvature-mediated rapid extravasation and penetration of nanoparticles against interstitial fluid pressure for improved drug delivery, Proc. Natl. Acad. Sci. 121 (2024) e2319880121.
[107] M.B. Albro, et al., Dynamic loading of deformable porous media can induce active solute transport, J. Biomech. 41 (2008) 3152–3157.
[108] M. Fiori, S. Pramanik, C.W. MacMinn, Solute transport due to periodic loading in a soft porous material, J. Fluid. Mech. 1009 (2025) A15.
[109] I. Peter, K. Wu, E.R. Edelman, Structural biomechanics modulate intramuscular distribution of locally delivered drugs, J. Biomech. 41 (2008) 2884–2891.
[110] Q. Wang, S. Pei, X.L. Lu, L. Wang, Q. Wu, On the characterization of interstitial fluid flow in the skeletal muscle endomysium, J. Mech. Behav. Biomed. Mater. 102 (2020) 103504.
[111] R.L. Mauck, C.T. Hung, G.A. Ateshian, Modeling of neutral solute transport in a dynamically loaded porous permeable gel: implications for articular cartilage biosynthesis and tissue engineering, J. Biomech. Eng. 125 (2003) 602–614.
[112] T.M. Quinn, V. Morel, J. Meister, Static compression of articular cartilage can reduce solute diffusivity and partitioning: implications for the chondrocyte biological response, J. Biomech. 34 (2001) 1463–1469.
[113] E. Nimer, R. Schneiderman, A. Maroudas, Diffusion and partition of solutes in cartilage under static load, Biophys. Chem. 106 (2003) 125–146.
[114] H.A. Leddy, F. Guilak, Site-specific effects of compression on macromolecular diffusion in articular cartilage, Biophys. J. 95 (2008) 4890–4895.
[115] N.O. Chahine, et al., Effect of dynamic loading on the transport of solutes into agarose hydrogels, Biophys. J. 97 (2009) 968–975.
[116] A.F. Roca-Arroyo, J.A. Gutierrez-Rivera, L.D. Morton, D.A. Castilla-Casadiego, Hydrogel network architecture design space: impact on mechanical and viscoelastic properties, Gels 11 (2025) 588.
[117] X. Lin, X. Zhao, C. Xu, L. Wang, Y. Xia, Progress in the mechanical enhancement of hydrogels: Fabrication strategies and underlying mechanisms, J. Polym. Sci. 60 (2022) 2525–2542.
[118] E.M. Grad, et al., Influence of network topology on the viscoelastic properties of dynamically crosslinked hydrogels, Front. Chem. 8 (2020) 536.
[119] M. Vigata, C. Meinert, D.W. Hutmacher, N. Bock, Hydrogels as drug delivery systems: A review of current characterization and evaluation techniques, Pharmaceutics 12 (2020) 1188.
[120] P. Lu, et al., Harnessing the potential of hydrogels for advanced therapeutic applications: current achievements and future directions, Signal. Transduct. Target. Ther. 9 (2024) 166.
[121] O. Lieleg, K. Ribbeck, Biological hydrogels as selective diffusion barriers, Trends Cell. Biol. 21 (2011) 543–551.
[122] M.S. Yoon, et al., Dual-drug delivery systems using hydrogel–nanoparticle composites: recent advances and key applications, Gels 11 (2025) 520.
[123] J. Di, et al., Stretch-triggered drug delivery from wearable elastomer films containing therapeutic depots, ACS nano 9 (2015) 9407–9415.
[124] H. Jeon, M.S. Kim, S.K. Hong, S.J. Cho, G. Lim, Tensile strain-controlled drug delivery system based on a cracked metal structure, Sens. Actuators B Chem. 270 (2018) 64–71.
[125] X. Gao, J. Li, J. Li, M. Zhang, J. Xu, Pain-free oral delivery of biologic drugs using intestinal peristalsis–actuated microneedle robots, Sci. Adv. 10 (2024) eadj7067.
[126] H. Li, et al., Biodegradable flexible electronic device with controlled drug release for cancer treatment, ACS Appl. Mater. & Interfaces 13 (2021) 21067–21075.
[127] S. Li, et al., Stretchable electronic facial masks for sonophoresis, ACS nano 16 (2022) 5961–5974.
[128] T. Kubota, Y. Kurashina, J. Zhao, K. Ando, H. Onoe, Ultrasound-triggered on-demand drug delivery using hydrogel microbeads with release enhancer, Mater. & Des. 203 (2021) 109580.
[129] C.C. Yu, et al., A conformable ultrasound patch for cavitation-enhanced transdermal cosmeceutical delivery, Adv. Mater. 35 (2023) 2300066.
[130] E. Davoodi, et al., Imaging-guided deep tissue in vivo sound printing, Science 388 (2025) 616–623.
[131] Y. Yang, et al., Improved pharmacodynamics of epidermal growth factor via microneedles-based self-powered transcutaneous electrical stimulation, Nat. Commun. 13 (2022) 6908.
[132] H. Wang, et al., A wearable transdermal device for on-demand drug delivery, Matter 8 (2025).
[133] S.K. Misra, et al., Electro-Stimulated Graphene-Polymer Nanocomposites Enable Wearable Patches With Feedback-Controlled Drug Release, Adv. Healthc. Mater. (2025) e05894.
[134] K. Long, et al., Green light-triggered intraocular drug release for intravenous chemotherapy of retinoblastoma, Adv. Sci. 8 (2021) 2101754.
[135] Y. Zhang, et al., Fiber-optic drug delivery strategy for synergistic cancer photothermal-chemotherapy, Light Science & Applications 13 (2024) 228.
[136] L. Bauman, B. Zhao, Multi-thermo responsive double network composite hydrogel for 3D printing medical hydrogel mask, J. Colloid Interface Sci. 638 (2023) 882–892.
[137] W. Guan, et al., Molecularly functionalized biomass hydrogels for sustainable atmospheric water harvesting, Adv. Mater. 37 (2025) 2420319.
[138] J. Park, W. Guan, C. Lei, G. Yu, Self-irrigation and slow-release fertilizer hydrogels for sustainable agriculture, ACS Mater. Lett. 6 (2024) 3471–3477.
[139] B. Mirani, et al., An advanced multifunctional hydrogel-based dressing for wound monitoring and drug delivery, Adv. Healthc. Mater. 6 (2017) 1700718.
[140] S. Rao, et al., Remotely controlled chemomagnetic modulation of targeted neural circuits, Nat. Nanotechnol. 14 (2019) 967–973.
[141] J. He, Y. Zhang, X. Yu, C. Xu, Wearable patches for transdermal drug delivery, Acta Pharm. Sin. B 13 (2023) 2298–2309.
[142] A. Kar, et al., Wearable and implantable devices for drug delivery: Applications and challenges, Biomaterials 283 (2022) 121435.
[143] S.Y. Chin, et al., Additive manufacturing of hydrogel-based materials for next-generation implantable medical devices, Sci. Robot. 2 (2017) eaah6451.
[144] J. Crank, The mathematics of diffusion, Oxford university press, 1979.
[145] E.L. Cussler, Diffusion: mass transfer in fluid systems, Cambridge university press, 2009.
[146] J. Park, E.J. Bailey, R.J. Composto, K.I. Winey, Single-Particle Tracking of Nonsticky and Sticky Nanoparticles in Polymer Melts, Macromolecules 53 (2020) 3933–3939.
[147] P.J. Griffin, et al., Influence of the Bound Polymer Layer on Nanoparticle Diffusion in Polymer Melts, ACS Macro Lett. 5 (2016) 1141–1145.
[148] E.J. Bailey, P.J. Griffin, R.J. Composto, K.I. Winey, Multiscale Dynamics of Small, Attractive Nanoparticles and Entangled Polymers in Polymer Nanocomposites, Macromolecules 52 (2019) 2181–2188.
[149] E. Parrish, et al., Nanoparticle diffusion during gelation of tetra poly(ethylene glycol) provides insight into nanoscale structural evolution, Soft Matter 16 (2020) 2256–2265.
[150] A. Karatrantos, R.J. Composto, K.I. Winey, N. Clarke, Nanorod Diffusion in Polymer Nanocomposites by Molecular Dynamics Simulations, Macromolecules 52 (2019) 2513–2520.
[151] K. Wang, K.I. Winey, Nanoparticle Diffusion in Crowded Polymer Nanocomposite Melts, ACS Macro Lett. 13 (2024) 1192–1197.
[152] K. Wang, K.I. Winey, Vehicular and Core–Shell Nanoparticle Diffusion in Attractive Entangled Polymer Melts, Macromolecules 57 (2024) 6789–6795.
[153] K.A. Rose, et al., Shape Anisotropy Enhances Nanoparticle Dynamics in Nearly Homogeneous Hydrogels, Macromolecules 55 (2022) 8514–8523.
[154] X. Zhao, et al., Soft materials by design: unconventional polymer networks give extreme properties, Chem. Rev. 121 (2021) 4309–4372.
[155] C.W. Rajawasam, et al., Educational series: characterizing crosslinked polymer networks, Polym. Chem. 15 (2024) 219–247.
[156] V.A. Kong, T.A. Staunton, J.E. Laaser, Effect of cross-link homogeneity on the high-strain behavior of elastic polymer networks, Macromolecules 57 (2024) 4670–4679.
[157] G. Munoz, et al., Heterogeneity effects in highly cross-linked polymer networks, Polymers 13 (2021) 757.
[158] C. Li, et al., Effects of network structures on the fracture of hydrogel, Extrem. Mech. Lett. 49 (2021) 101495.
[159] H. Lei, et al., Stretchable hydrogels with low hysteresis and anti-fatigue fracture based on polyprotein cross-linkers, Nat. Commun. 11 (2020) 4032.
[160] Y. Tanaka, et al., Determination of fracture energy of high strength double network hydrogels, J. Phys. Chem. B 109 (2005) 11559–11562.

[161] E. Zhang, R. Bai, X.P. Morelle, Z. Suo, Fatigue fracture of nearly elastic hydrogels, Soft Matter 14 (2018) 3563–3571.
[162] J. Kim, G. Zhang, M. Shi, Z. Suo, Fracture, fatigue, and friction of polymers in which entanglements greatly outnumber cross-links, Sci. Adv. 374 (2021) 212–216.
[163] T. Sakai, et al., Design and fabrication of a high-strength hydrogel with ideally homogeneous network structure from tetrahedron-like macromonomers, Macromolecules 41 (2008) 5379–5384.
[164] Y. Akagi, T. Matsunaga, M. Shibayama, U.-i Chung, T. Sakai, Evaluation of topological defects in tetra-PEG gels, Macromolecules 43 (2010) 488–493.
[165] Y. Akagi, et al., Examination of the theories of rubber elasticity using an ideal polymer network, Macromolecules 44 (2011) 5817–5821.
[166] T. Sakai, Experimental verification of homogeneity in polymer gels, Polym. J. 46 (2014) 517–523.
[167] T. Katashima, K. Urayama, U.-i Chung, T. Sakai, Strain energy density function of a near-ideal polymer network estimated by biaxial deformation of Tetra-PEG gel, Soft Matter 8 (2012) 8217–8222.
[168] Y. Akagi, H. Sakurai, J.P. Gong, U.-i Chung, T. Sakai, Fracture energy of polymer gels with controlled network structures, J. Chem. Phys. 139 (2013).
[169] Y. Ren, P.K. Purohit, Applications of a continuum model for brush gels, Int. J. Solids Struct. 324 (2026) 113664.
[170] A.N. Keith, et al., Bottlebrush bridge between soft gels and firm tissues, ACS Cent. Sci. 6 (2020) 413–419.
[171] J.M. Sarapas, T.B. Martin, A. Chremos, J.F. Douglas, K.L. Beers, Bottlebrush polymers in the melt and polyelectrolytes in solution share common structural features, Proc. Natl. Acad. Sci. 117 (2020) 5168–5175.
[172] L.-H. Cai, Molecular structure of foldable bottlebrush polymers in melts, Macromolecules 58 (2025) 4320–4339.
[173] M. Abbasi, L. Faust, M. Wilhelm, Comb and bottlebrush polymers with superior rheological and mechanical properties, Adv. Mater. 31 (2019) 1806484.
[174] P. Xu, et al., Conductive and elastic bottlebrush elastomers for ultrasoft electronics, Nat. Commun. 14 (2023) 623.
[175] B.R. Clarke, et al., The impact of polymerization chemistry on the mechanical properties of poly (dimethylsiloxane) bottlebrush elastomers, Macromolecules 55 (2022) 10312–10319.
[176] V. Asadi, J. Ruiz-Franco, J. van der Gucht, T.E. Kodger, Tuning moduli of hybrid bottlebrush elastomers by molecular architecture, Mater. & Des. 234 (2023) 112326.
[177] T. Kang, et al., Entanglements and fracture in polymers, Chem. Rev. 125 (2025) 11032–11057.
[178] J.L. Self, et al., Dynamic bottlebrush polymer networks: self-healing in super-soft materials, J. Am. Chem. Soc. 142 (2020) 7567–7573.
[179] M.A. Haque, T. Kurokawa, J.P. Gong, Super tough double network hydrogels and their application as biomaterials, Polymer 53 (2012) 1805–1822.
[180] E.M. Foster, et al., Effect of polymer network architecture, enhancing soft materials using orthogonal dynamic bonds in an interpenetrating network, ACS Macro Lett. 6 (2017) 495–499.
[181] T. Matsuda, R. Kawakami, T. Nakajima, Y. Hane, J.P. Gong, Revisiting the origins of the fracture energy of tough double-network hydrogels with quantitative mechanochemical characterization of the damage zone, Macromolecules 54 (2021) 10331–10339.
[182] J. You, Z. Liu, Revealing novel insights into the toughening mechanism of double network hydrogels via uniaxial tensile tests, J. Mech. Phys. Solids 190 (2024) 105710.
[183] S. Wang, E. Euchler, K. Schneider, S. Wießner, Characterization of the deformation and fracture of tough double-network hydrogels, Polymer (2025) 129190.
[184] J. You, J. Zhang, B. Yang, C. Wang, Z. Liu, Damage mechanism insights into double network hydrogels: Predicting cyclic loading behaviors via monotonic loading, J. Mech. Phys. Solids (2025) 106324.
[185] Y. Noda, Y. Hayashi, K. Ito, From topological gels to slide-ring materials, J. Appl. Polym. Sci. 131 (2014).
[186] K. Ito, Novel Cross-Linking Concept of Polymer Network: Synthesis, Structure, and Properties of Slide-Ring Gels with Freely Movable Junctions, Polym. J. 39 (2007) 489–499.
[187] D. Chen, S. Panyukov, L. Sapir, M. Rubinstein, Elasticity of Slide-Ring Gels, ACS Macro Lett. 12 (2023) 362–368.
[188] J. Huang, J. Liu, S. Lin, Topological Mechanics of Entangled Networks. arXiv preprint arXiv:2509.17813 (2025).
[189] H. Tabit, et al., Tailoring Crosslinks through Time— A Paradigm for Tough Hydrogels, Chem. Rev. (2026).
[190] X. Bao, et al., Unusually long polymers crosslinked by domains of physical bonds, Nat. Commun. 16 (2025) 4749.
[191] N. Petelinšek, S. Mommer, Tough hydrogels for load-bearing applications, Adv. Sci. 11 (2024) 2307404.
[192] X. He, et al., Extreme hydrogel bioelectronics, Adv. Funct. Mater. 34 (2024) 2405896.
[193] S. Lin *et al.*, Impact of Topological Defects on Strain-Induced Crystallization in Elastocaloric Polymers.
[194] S. Lin, et al., Anti-fatigue-fracture hydrogels, Sci. Adv. 5 (2019) eaau8528.
[195] J. Wang, et al., Actuation mechanisms of a semicrystalline elastomer-based polymer artificial muscle with high actuation strain, Macromolecules 55 (2022) 3986–3999.
[196] H. Li, et al., Hierarchical crack-resistant, tissue-mimetic hydrogels enabled by progressive nanocrystallization of anisotropic polymer networks, Nat. Commun. 16 (2025) 10890.
[197] W. Chen, et al., Superstrong and tough hydrogel through physical cross-linking and molecular alignment, Biomacromolecules 20 (2019) 4476–4484.
[198] J. Zhang, M. Zhang, H. Wan, J. Zhou, A. Lu, Coordinatively stiffen and toughen polymeric gels via the synergy of crystal-domain cross-linking and chelation cross-linking, Nat. Commun. 16 (2025) 320.
[199] C. Xu, et al., Ultrastrong eutectogels engineered via integrated mechanical training in molecular and structural engineering, Nat. Commun. 16 (2025) 2589.
[200] H. Lee, J. Kim, M. Lee, J. Kang, Dynamic bond chemistry in soft materials: bridging adaptability and mechanical robustness, Chem. Rev. 125 (2025) 11379–11425.
[201] N. Zheng, Y. Xu, Q. Zhao, T. Xie, Dynamic covalent polymer networks: a molecular platform for designing functions beyond chemical recycling and self-healing, Chem. Rev. 121 (2021) 1716–1745.
[202] S.V. Wanasinghe, O.J. Dodo, D. Konkolewicz, Dynamic bonds: adaptable timescales for responsive materials, Angew. Chem. 134 (2022) e202206938.
[203] J.M. Winne, L. Leibler, F.E. Du Prez, Dynamic covalent chemistry in polymer networks: a mechanistic perspective, Polym. Chem. 10 (2019) 6091–6108.
[204] Z. Gong, et al., High-strength, tough, fatigue resistant, and self-healing hydrogel based on dual physically cross-linked network, ACS Appl. Mater. & Interfaces 8 (2016) 24030–24037.
[205] X. Liu, L. Duan, G. Gao, Rapidly self-recoverable and fatigue-resistant hydrogels toughened by chemical crosslinking and hydrophobic association, Eur. Polym. J. 89 (2017) 185–194.
[206] K. Yu, A. Xin, Q. Wang, Mechanics of self-healing polymer networks crosslinked by dynamic bonds, J. Mech. Phys. Solids 121 (2018) 409–431.
[207] L. Zhang, S. Chen, Z. You, Hybrid cross-linking to construct functional elastomers, Acc. Chem. Res. 56 (2023) 2907–2920.
[208] Q. Chen, et al., Fracture of the physically cross-linked first network in hybrid double network hydrogels, Macromolecules 47 (2014) 2140–2148.
[209] J. Xu, X. Liu, X. Ren, G. Gao, The role of chemical and physical crosslinking in different deformation stages of hybrid hydrogels, Eur. Polym. J. 100 (2018) 86–95.
[210] J.H.M. Wong, et al., Injectable hybrid-crosslinked hydrogels as fatigue-resistant and shape-stable skin depots, Biomacromolecules 23 (2022) 3698–3712.
[211] Y. Baba, et al., Mechanical properties of homogeneous polymer networks prepared by star polymer synthesis methods, Macromolecules 54 (2021) 10468–10476.
[212] F.A. Escobedo, J.J. De Pablo, Molecular simulation of polymeric networks and gels: phase behavior and swelling, Phys. Rep. 318 (1999) 85–112.
[213] R.J. Wagner, J. Dai, X. Su, F.J. Vernerey, A mesoscale model for the micromechanical study of gels, J. Mech. Phys. Solids 167 (2022) 104982.
[214] J. Lei, Y. Gao, S. Xu, L. He, Z. Liu, The effect of the effective polymer network on the extremely large deformation and fracture behaviors of polyacrylamide hydrogels, J. Mech. Phys. Solids 200 (2025) 106124.
[215] A.D. Drozdov, A. Papadimitriou, J. Liely, C.-G. Sanporean, Constitutive equations for the kinetics of swelling of hydrogels, Mech. Mater. 102 (2016) 61–73.
[216] D. Okumura, H. Kawabata, S.A. Chester, A general expression for linearized properties of swollen elastomers undergoing large deformations, J. Mech. Phys. Solids 135 (2020) 103805.
[217] H. Xin, S.Z. Saricilar, H.R. Brown, P.G. Whitten, G.M. Spinks, Effect of first network topology on the toughness of double network hydrogels, Macromolecules 46 (2013) 6613–6620.
[218] Z. Shao, Q. Liu, Independent characterization of the elastic and the mixing parts of hydrogel osmotic pressure, Extrem. Mech. Lett. 64 (2023) 102085.
[219] F.K. Metze, S. Sant, Z. Meng, H.-A. Klok, K. Kaur, Swelling-activated, soft mechanochemistry in polymer materials, Langmuir 39 (2023) 3546–3557.
[220] K. Garyfallogiannis, P.K. Purohit, J.L. Bassani, Energy release rate for cracks in hydrogels undergoing finite deformations, J. Mech. Phys. Solids 167 (2022) 105009.
[221] J.-F. Feng, et al., Bioinspired ultra tear-resistant elastomer with a slidable double-network structure, ACS Appl. Mater. & Interfaces 14 (2022) 31424–31434.
[222] J.R. Colvin, THE SIZE AND SHAPE OF LYSOZYME, Can. J. Chem. 30 (1952) 831–834.
[223] F. Gittes, B. Mickey, J. Nettleton, J. Howard, Flexural rigidity of microtubules and actin filaments measured from thermal fluctuations in shape, J. Cell. Biol. 120 (1993) 923–934.
[224] I.L. Ivanovska, et al., Bacteriophage Capsids: Tough Nanoshells with Complex Elastic Properties, Proc. Natl. Acad. Sci. USA 101 (2004) 7600–7605.
[225] B. Moss, Poxvirus entry and membrane fusion, Virology 344 (2006) 48–54.
[226] H. Gadêlha, E.A. Gaffney, Flagellar ultrastructure suppresses buckling instabilities and enables mammalian sperm navigation in high-viscosity media, J. R. Soc. Interface 16 (2019) 20180668.
[227] T.M. Koehler, Bacillus anthracis physiology and genetics, Mol. Asp. Med. 30 (2009) 386–396.
[228] M. Diez-Silva, M. Dao, J. Han, C.-T. Lim, S. Suresh, Shape and biomechanical characteristics of human red blood cells in health and disease, MRS Bull. 35 (2010) 382–388.
[229] T. Arce Fernando, et al., Nanoscale Structural and Mechanical Properties of Nontypeable Haemophilus influenzae Biofilms, J. Bacteriol. 191 (2009) 2512–2520.
[230] K. Sano, T. Fukuzono, T. Yokoyama, Y. Chiba, J. Kato, Breeding and conservation of Luciola cruciata Motschulsky, 1854 (Coleoptera: Lampyridae) larvae in forests near chemical factories, SN Appl. Sci. 4 (2022) 307.
[231] I.A. Chelnokova, I.A. Nikitina, M.N. Starodubtseva, Mechanical properties of blood exosomes and lipoproteins after the rat whole blood irradiation with X-rays in vitro explored by atomic force microscopy, Micron 184 (2024) 103662.

[232] S. Chakraborti, P. Chakrabarti, "Self-Assembly of Ferritin: Structure, Biological Function and Potential Applications in Nanotechnology", in: S. Perrett, A.K. Buell, T.P.J. Knowles (Eds.), Biological and Bio-inspired Nanomaterials: Properties and Assembly Mechanisms, Springer Singapore, Singapore, 2019, pp. 313–329, https://doi.org/10.1007/978-981-13-9791-2_10.
[233] J. Zhang, et al., Cargo loading within ferritin nanocages in preparation for tumor-targeted delivery, Nat. Protoc. 16 (2021) 4878–4896.
[234] I.A. Schaap, A. Eghiaian, F.Fau- des Georges, C. des Georges, A. Fau - Veigel, C. Veigel, Effect of envelope proteins on the mechanical properties of influenza virus, J. Biol. Chem. 287 (2012).
[235] P. Ramdas, A.K. Sahu, T. Mishra, V. Bhardwaj, A. Chande, From Entry to Egress: Strategic Exploitation of the Cellular Processes by HIV-1, Front. Microbiol. 11 (2020).
[236] X. Zhou, Y. Li, "Chapter 5 - Oral Mucosal Microbes", in: X. Zhou, Y. Li (Eds.), Atlas of Oral Microbiology, Academic Press, Oxford, 2015, pp. 95–107.
[237] R. Kuse, S. Schuster, H. Schübbe, S. Dix, K. Hausmann, Blood lymphocyte volumes and diameters in patients with chronic lymphocytic leukemia and normal controls, Blut 50 (1985) 243–248.
[238] E. Giolo, et al., Study of the mechanical properties of fresh and cryopreserved individual human oocytes, Eur. Biophys. J. 48 (2019) 585–592.
[239] D. Jaiswal, et al., Stiffness analysis of 3D spheroids using microtweezers, PLOS ONE 12 (2017) e0188346.
[240] W. Bai, et al., Toxicity of zinc oxide nanoparticles to zebrafish embryo: a physicochemical study of toxicity mechanism, J. Nanopart. Res. 12 (2010) 1645–1654.
[241] S. Christodoulou, et al., Synthesis of highly luminescent wurtzite CdSe/CdS giant-shell nanocrystals using a fast continuous injection route, J. Mater. Chem. C. 2 (2014) 3439–3447.
[242] B. Yang, L. Xu, Y. Liu, B. Liu, M. Zhang, Preparation of monodisperse polystyrene microspheres with different functional groups using soap-free emulsion polymerization, Colloid Polym. Sci. 299 (2021) 1095–1102.
[243] C. Ye, et al., Mechano-diffusion of particles in stretchable hydrogels, Soft Matter 21 (2025) 2230–2241.
[244] M. Abboud, et al., Superparamagnetic Fe3O4 nanoparticles, synthesis and surface modification, Mater. Sci. Semicond. Process. 39 (2015) 641–648.
[245] J. Ge, et al., Monodisperse SiO2 Spheres: Efficient Synthesis and Applications in Chemical Mechanical Polishing, Nanomaterials 15 (2025) 665.
[246] Y. Hu, et al., Preparation of large micron-sized monodisperse polystyrene/silver core–shell microspheres with compact shell structure and their electrical conductive and catalytic properties, RSC Adv. 5 (2015) 58–67.
[247] J. Xiao, H. Cao, H. Cong, Y. Shen, B. Yu, Preparation and modification of monodisperse large particle size crosslinked polystyrene microspheres and their application in high performance liquid chromatography, React. Funct. Polym. 178 (2022) 105357.
[248] K. Lim, J. Che, J. Lee, Experimental study on adsorption characteristics of a water and silica-gel based thermal energy storage (TES) system, Appl. Therm. Eng. 110 (2017) 80–88.
[249] N. Tomović, K.T. Trifković, M. Rakin, M. Rakin, B. Bugarski, Influence of compression speed and deformation percentage on mechanical properties of calcium alginate particles, Chem. Ind. & Chem. Eng. Q. 21 (2015) 411–417.
[250] L. Fang, et al., Movement patterns of ellipsoidal particles with different axial ratios in three-body abrasion of monocrystalline copper: a large scale molecular dynamics study, RSC Adv. 7 (2017) 26790–26800.
[251] R.C. Oliver, et al., Dependence of Micelle Size and Shape on Detergent Alkyl Chain Length and Head Group, PLOS ONE 8 (2013) e62488.
[252] X. Wang, et al., Nanoscale Investigation of Elasticity Changes and Augmented Rigidity of Block Copolymer Micelles Induced by Reversible Core-Cross-Linking, ACS Appl. Mater. & Interfaces 17 (2025) 27557–27567.
[253] N. Hao, Y. Nie, A. Tadimety, A.B. Closson, J.X.J. Zhang, Microfluidics-mediated self-template synthesis of anisotropic hollow ellipsoidal mesoporous silica nanomaterials, Mater. Res. Lett. 5 (2017) 584–590.
[254] C. Han, J. Han, Q. Li, J. Xie, Wet Chemical Controllable Synthesis of Hematite Ellipsoids with Structurally Enhanced Visible Light Property, Sci. World J. 2013 (2013) 410594.
[255] D. Schneider, et al., Elongated polystyrene spheres as resonant building blocks in anisotropic colloidal crystals, Soft Matter 9 (2013) 9129–9136.
[256] X. Kou, Y. Yang, Q. Lu, Q. Ke, Y. Zhang, Controlled construction of ellipsoidal microcapsules via tannic acid/cellulose nanocrystal interfacial engineering, Carbohydr. Polym. 369 (2025) 124273.
[257] X.D. Sun, H. Yang, Z. Duan, K. Yan, Polyethyleneimine modified cellulose nanofiber microgel for rapid and efficient Cr(VI) removal, Cellulose 32 (2025) 2537–2551.
[258] M.A. Rahman, M. Rahman, M. Mia, A.B.M.A. Asad, A. Fardin, Manufacturing of Al Alloy Microrods by Micro Cutting in a Micromachining Center, Micromachines 10 (2019) 831.
[259] S. Ma, N. Mukherjee, E. Mikhailova, H. Bayley, Gel Microrods for 3D Tissue Printing, Adv. Biosyst. 1 (2017) 1700075.
[260] A.W. Helkin, et al., Dyslipidemia Part 1—Review of Lipid Metabolism and Vascular Cell Physiology, Vasc. Endovasc. Surg. 50 (2016) 107–118.
[261] E. Jang, J. Robert, L. Rohrer, A. von Eckardstein, W.L. Lee, Transendothelial transport of lipoproteins, Atherosclerosis 315 (2020) 111–125.
[262] A.T. Jan, et al., Expedition into Exosome Biology: A Perspective of Progress from Discovery to Therapeutic Development, Cancers 13 (2021) 1157.
[263] N.J. Patel, A. Ashraf, E.J. Chung, Extracellular Vesicles as Regulators of the Extracellular Matrix, Bioengineering 10 (2023) 136.
[264] Y. Zhai, et al., Mechanical strength and biomechanics of extracellular vesicles, Nano Today 66 (2026) 102905.
[265] M. i Li, et al., Multiparametric atomic force microscopy imaging of single native exosomes, Acta Biochim. Et. Biophys. Sin. 53 (2021) 385–388.
[266] J. Zhang, C. Cui, X. Zhou, Study on elastic modulus of individual ferritin, Chin. Sci. Bull. 54 (2009) 723–726.
[267] R. Mehta, A. Kushwaha, S. Sah, J. Feehan, V. Apostolopoulos, Detection of vaccine-derived poliovirus type-3 in sewage of Kathmandu Valley, Nepal, Clin. Infect. Pract. 24 (2024) 100388.
[268] Y. Kurosawa, S. Sato, T. Okuyama, M. Taoka, Sequential two-step chromatographic purification of infectious poliovirus using ceramic fluoroapatite and ceramic hydroxyapatite columns, PLOS ONE 14 (2019) e0222199.
[269] N. Kol, et al., A stiffness switch in human immunodeficiency virus, Biophys. J. 92 (2006) 7.
[270] E.O. Freed, HIV-1 assembly, release and maturation, Nat. Rev. Microbiol. 13 (2015) 484–496.
[271] T. Noda, Native morphology of influenza virions, Front. Microbiol. 2 (2011).
[272] R. Boudjemaa, et al., Direct observation of the cell-wall remodeling in adhering Staphylococcus aureus 27217: An AFM study supported by SEM and TEM, Cell. Surf. 5 (2019) 100018.
[273] X. Cai, et al., Connection between biomechanics and cytoskeleton structure of lymphocyte and Jurkat cells: An AFM study, Micron 41 (2010) 257–262.
[274] D.-H. Kim, et al., Mechanical property characterization of the zebrafish embryo chorion, 26th Annu. Int. Conf. IEEE Eng. Med. Biol. Soc. (IEEE (2004) 5061–5064.
[275] V. Sergunova, et al., Investigation of Red Blood Cells by Atomic Force Microscopy, Sensors 22 (2022) 2055.
[276] S.M. Han, et al., M13 bacteriophage-based bio-nano systems for bioapplication, BioChip J. 16 (2022) 227–245.
[277] P. Sunanda, B. Panda, C. Dash, R.N. Padhy, P. Routray, An illustration of human sperm morphology and their functional ability among different group of subfertile males, Andrology 6 (2018) 680–689.
[278] S.C. Parija, "Haemophilus and Bordetella", in: S.C. Parija (Ed.), Textbook of Microbiology and Immunology, Springer Nature Singapore, Singapore, 2023, pp. 579–596, https://doi.org/10.1007/978-981-19-3315-8_40.
[279] M. Basavaraju, G.B. Shivanna, "Escherichia coli: An Overview of Main Characteristics", in: M. Starčič Erjavec (Ed.), Escherichia coli - Old and New Insights, IntechOpen, London, 2022, https://doi.org/10.5772/intechopen.105508.
[280] J. Lee, et al., Determining the Young's Modulus of the Bacterial Cell Envelope, ACS Biomater. Sci. & Eng. 10 (2024) 2956–2966.
[281] A.V. Nikolaev, T.J.S. Dennis, K. Prassides, A.K. Soper, Molecular structure of the C70 fullerene, Chem. Phys. Lett. 223 (1994) 143–148.
[282] T. Kizuka, K. i Miyazawa, T. Tokumine, Solvation-Assisted Young's Modulus Control of Single-Crystal Fullerene C70 Nanowhiskers, J. Nanotechnol. 2012 (2012) 583817.
[283] Z. Zhang, et al., Ultraprecise anisotropy mapping of Young's modulus in single-crystal diamond via mechanical resonance, Appl. Phys. Lett. 127 (2025) 181904.
[284] D. Chicot, et al., Mechanical properties of magnetite (Fe3O4), hematite (α-Fe2O3) and goethite (α-FeO·OH) by instrumented indentation and molecular dynamics analysis, Mater. Chem. Phys. 129 (2011) 862–870.
[285] D.R. Streltsov, K.M. Borisov, A.A. Kalinina, A.M. Muzafarov, Quantitative Elasticity Mapping of Submicron Silica Hollow Particles by PeakForce QNM AFM Mode, Nanomaterials 13 (2023) 1916.
[286] C. Kim, et al., Stem Cell Mechanosensation on Gelatin Methacryloyl (GelMA) Stiffness Gradient Hydrogels, Ann. Biomed. Eng. 48 (2020) 893–902.
[287] N. Kishore, V. Nagarajan, R. Chandiramouli, Mechanical properties and band structure of CdSe and CdTe nanostructures at high pressure-a first-principles study, Process. Appl. Ceram. 13 (2019) 124–131.
[288] H. McSkimin, Measurement of elastic constants at low temperatures by means of ultrasonic waves–data for silicon and germanium single crystals, and for fused silica, J. Appl. Phys. 24 (1953) 988–997.
[289] S. Lu, et al., Monodisperse Fluorescent Polystyrene Microspheres for Staphylococcus aureus Aerosol Simulation, Polymers 15 (2023) 3614.
[290] D. Guo, J. Li, G. Xie, Y. Wang, J. Luo, Elastic Properties of Polystyrene Nanospheres Evaluated with Atomic Force Microscopy: Size Effect and Error Analysis, Langmuir 30 (2014) 7206–7212.
[291] N. Tottori, S. Choi, T. Nisisako, Production of Monodisperse Oil-in-Water Droplets and Polymeric Microspheres Below 20 μm Using a PDMS-Based Step Emulsification Device, Micromachines 16 (2025) 132.
[292] T. Adachi, S. Sakka, Dependence of the elastic moduli of porous silica gel prepared by the sol-gel method on heat-treatment, J. Mater. Sci. 25 (1990) 4732–4737.
[293] C.R. Cantor, P.R. Schimmel, Biophysical chemistry: Part III: the behavior of biological macromolecules, Macmillan, 1980.
[294] S. De, K. Kaus, S. Sinclair, B.C. Case, R. Olson, Structural basis of mammalian glycan targeting by Vibrio cholerae cytolysin and biofilm proteins, PLOS Pathog. 14 (2018) e1006841.
[295] R. Wintjens, et al., ^{1}H NMR Study on the Binding of Pin1 Trp-Trp Domain with Phosphothreonine Peptides*, J. Biol. Chem. 276 (2001) 25150–25156.
[296] G. Antonini, et al., Glycomimetic antagonists of BC2L-C lectin: insights from molecular dynamics simulations, Front. Mol. Biosci. 10 - 2023 (2023).
[297] C. Robert, et al., Structural analysis of the interaction between human cytokine BMP-2 and the antagonist Noggin reveals molecular details of cell chondrogenesis inhibition, J. Biol. Chem. 299 (2023) 102892.

[298] D. Cunningham, et al., Structural and biophysical studies of PCSK9 and its mutants linked to familial hypercholesterolemia, Nat. Struct. & Mol. Biol. 14 (2007) 413–419.
[299] Z. Tnimov, et al., Quantitative Analysis of Prenylated RhoA Interaction with Its Chaperone, RhoGDI*, J. Biol. Chem. 287 (2012) 26549–26562.
[300] A.P. Behera, et al., Structural insights into the nanomolar affinity of RING E3 ligase ZNRF1 for Ube2N and its functional implications, Biochem. J. 475 (2018) 1569–1582.
[301] M. Cai, et al., Solution NMR Structure of the Barrier-to-Autointegration Factor-Emerin Complex*, J. Biol. Chem. 282 (2007) 14525–14535.
[302] M.J. van Raaij, E. Chouin, H. van der Zandt, J.M. Bergelson, S. Cusack, Dimeric Structure of the Coxsackievirus and Adenovirus Receptor D1 Domain at 1.7 Å Resolution, Structure 8 (2000) 1147–1155.
[303] B.A. Manjasetty, et al., X-ray structure of engineered human Aortic Preferentially Expressed Protein-1 (APEG-1), BMC Struct. Biol. 5 (2005) 21.
[304] C. Bee, et al., Exploring the Dynamic Range of the Kinetic Exclusion Assay in Characterizing Antigen-Antibody Interactions, PLOS ONE 7 (2012) e36261.
[305] C. Eigenbrot, M. Ultsch, A. Dubnovitsky, L. Abrahmsén, T. Härd, Structural basis for high-affinity HER2 receptor binding by an engineered protein, Proc. Natl. Acad. Sci. U. S. A. 107 (2010) 15039–15044.
[306] P. Czihal, et al., Api88 Is a Novel Antibacterial Designer Peptide To Treat Systemic Infections with Multidrug-Resistant Gram-Negative Pathogens, ACS Chem. Biol. 7 (2012) 1281–1291.
[307] Y.C. Wang, et al., Structural basis of SARS-CoV-2 main protease inhibition by a broad-spectrum anti-coronaviral drug, Am. J. Cancer Res. 10 (2020).
[308] G.J. Lake, A.G. Thomas, The strength of highly elastic materials, Proc. R. Soc. Lond. A. Math. Phys. Sci. 300 (1967) 108–119.
[309] C. Zhang, et al., Enhanced heat and corrosion resistance of organic silicone coatings by dual shielding effects of Zn powder, Electrochim. Acta 509 (2025) 145329.
[310] M. Tan, et al., Cobalt-nanoparticle impregnated nitrogen-doped porous carbon derived from Schiff-base polymer as excellent bifunctional oxygen electrocatalysts for rechargeable zinc-air batteries, J. Power Sources 490 (2021) 229570.
[311] E. Adabifiroozjaei, et al., Molecular dynamics simulation of vacancy cluster formation in β- and α-Si3N4, Comput. Mater. Sci. 178 (2020) 109632.
[312] W. Yu, S. Wang, C. Liu, Q. Li, X. Xu, Study on the thermal stability of a new siloxane working fluid modified by octamethyltrisiloxane and its application potential in organic Rankine cycle, Energy 320 (2025) 135017.
[313] L. Wang, et al., Photoelectrochemical nitrogen reduction: A step toward achieving sustainable ammonia synthesis, Chin. J. Catal. 43 (2022) 1761–1773.
[314] L. Shi, et al., Photocatalytic conversion of CO to fuels with water by B-doped graphene/g-C3N4 heterostructure, Sci. Bull. 66 (2021) 1186–1193.
[315] S.R. Kass, π-Bond Dissociation Energies: C–C, C–N, and C–O, J. Org. Chem. 89 (2024) 15158–15163.
[316] H. Li, H. Li, Q. Dai, H. Li, J.-L. Brédas, Hydrolytic Stability of Boronate Ester-Linked Covalent Organic Frameworks, Adv. Theory Simul. 1 (2018) 1700015.
[317] Y.-R. Luo, Comprehensive handbook of chemical bond energies, CRC press, 2007.
[318] Y. Hu, et al., Molecularly engineered cardanol derived epoxy vitrimers based on dynamic disulfide and dynamic ester exchanges with desirable dynamic response, degradability, and recyclability, Chem. Eng. J. 477 (2023) 147284.
[319] M.V. Basilevskii, A.G. Shamov, V.A. Tikhomirov, Transition state of the Diels-Alder reaction, J. Am. Chem. Soc. 99 (1977) 1369–1372.
[320] S. Liu, Y. Lei, X. Qi, Y. Lan, Reactivity for the Diels–Alder Reaction of Cumulenes: A Distortion-Interaction Analysis along the Reaction Pathway, J. Phys. Chem. A 118 (2014) 2638–2645.
[321] C.T. Mortimer, J. Waterhouse, Enthalpy of combustion of diphenyl diselenide, J. Chem. Thermodyn. 12 (1980) 961–965.
[322] T. Steiner, The Hydrogen Bond in the Solid State, Angew. Chem. Int. Ed. 41 (2002) 48–76.
[323] O. Markovitch, N. Agmon, Structure and Energetics of the Hydronium Hydration Shells, J. Phys. Chem. A 111 (2007) 2253–2256.
[324] D.B. Varshey, J.R.G. Sander, T. Friščić, L.R. MacGillivray, "Supramolecular Interactions", Supramol. Chem. (2012).
[325] P.E. Rouse, Jr, A Theory of the Linear Viscoelastic Properties of Dilute Solutions of Coiling Polymers, J. Chem. Phys. 21 (1953) 1272–1280.
[326] A. Einstein, On the motion of small particles suspended in liquids at rest required by the molecular-kinetic theory of heat, Ann. der Phys. 17 (1905) 208.
[327] M. von Smoluchowski, Zur kinetischen Theorie der Brownschen Molekularbewegung und der Suspensionen, Ann. der Phys. 326 (1906) 756–780.
[328] M. Doi, S.F. Edwards, S.F. Edwards, The theory of polymer dynamics, 73, oxford university press, 1988.
[329] M. Rubinstein, R.H. Colby, Polymer physics, Oxford university press, 2003.
[330] B. Mei, T.-W. Lin, C.E. Sing, K.S. Schweizer, Self-consistent hopping theory of activated relaxation and diffusion of dilute penetrants in dense crosslinked polymer networks, J. Chem. Phys. 158 (2023).
[331] P.-G.De Gennes, Scaling concepts in polymer physics, Cornell university press, 1979.
[332] V. Sorichetti, V. Hugouvieux, W. Kob, Dynamics of nanoparticles in polydisperse polymer networks: From free diffusion to hopping, Macromolecules 54 (2021) 8575–8589.
[333] C. Xue, X. Shi, Y. Tian, X. Zheng, G. Hu, Diffusion of Nanoparticles with Activated Hopping in Crowded Polymer Solutions, Nano Lett. 20 (2020) 3895–3904.
[334] C. Xue, Y. Huang, X. Zheng, G. Hu, Hopping Behavior Mediates the Anomalous Confined Diffusion of Nanoparticles in Porous Hydrogels, J. Phys. Chem. Lett. 13 (2022) 10612–10620.
[335] J. Wang, et al., Diffusion of rod-like nanoparticles in non-adhesive and adhesive porous polymeric gels, J. Mech. Phys. Solids 112 (2018) 431–457.
[336] T.H. Wong, J. Ma, A. Sherburne, S. Lin, Diffusion and release of molecules in swelling polymer networks, Extrem. Mech. Lett. 84 (2026) 102466.
[337] T.K. Venkatadri, C. Ye, T. Cohen, S. Lin, Torsion-mediated instabilities in confined elastic layers, J. Mech. Phys. Solids 198 (2025) 106064.
[338] T.-W. Lin, C.E. Sing, Effect of penetrant–polymer interactions and shape on the motion of molecular penetrants in dense polymer networks, J. Chem. Phys. 160 (2024) 114905.
[339] Y. Chen, et al., Anisotropic and Non-Gaussian Diffusion of Thin Nanorods in Polymer Networks, Macromolecules 57 (2024) 5105–5118.
[340] H. Xu, X. Zheng, X. Shi, Deciphering non-Gaussianity of diffusion based on the evolution of diffusivity, Phys. Rev. Res. 6 (2024) 023014.
[341] D.B. Mayer, et al., Two-dimensional Brownian motion of anisotropic dimers, Phys. Rev. E 104 (2021) 014605.
[342] J.P. Segovia-Gutiérrez, M.A. Escobedo-Sánchez, E. Sarmiento-Gómez, S. U. Egelhaaf, Diffusion of Anisotropic Particles in Random Energy Landscapes—An Experimental Study, Front. Phys. 7 - 2019 (2020).
[343] N.A. Peppas, J.Z. Hilt, A. Khademhosseini, R. Langer, Hydrogels in Biology and Medicine: From Molecular Principles to Bionanotechnology, Adv. Mater. 18 (2006) 1345–1360.
[344] E. Parrish, M.A. Caporizzo, R.J. Composto, Network confinement and heterogeneity slows nanoparticle diffusion in polymer gels, J. Chem. Phys. 146 (2017) 203318.
[345] R. Lin, S. Xu, Z. Liu, A visco-hyperelastic model for hydrogels with different water content and its finite element implementation, Int. J. Solids Struct. 293 (2024) 112761.
[346] A.J.A. Baker, et al., Mechanical characterization data of polyacrylamide hydrogel formulations and 3D printed PLA for application in human head phantoms, Data Brief. 48 (2023) 109114.
[347] W. Hong, X. Zhao, J. Zhou, Z. Suo, A theory of coupled diffusion and large deformation in polymeric gels, J. Mech. Phys. Solids 56 (2008) 1779–1793.
[348] K. Yue, et al., Synthesis, properties, and biomedical applications of gelatin methacryloyl (GelMA) hydrogels, Biomaterials 73 (2015) 254–271.
[349] D. Loessner, et al., Functionalization, preparation and use of cell-laden gelatin methacryloyl–based hydrogels as modular tissue culture platforms, Nat. Protoc. 11 (2016) 727–746.
[350] Z. Sheng, et al., Mechanics of single-network hydrogels with network imperfection, Giant 18 (2024) 100287.
[351] J. Ma, et al., Designing Ultratough Single-Network Hydrogels with Centimeter-Scale Fractocohesive Lengths via Inelastic Crack Blunting, Adv. Mater. 36 (2024) 2311795.
[352] M. Rubinstein, S. Panyukov, Nonaffine Deformation and Elasticity of Polymer Networks, Macromolecules 30 (1997) 8036–8044.
[353] C.M. Hassan, N.A. Peppas, Structure and Morphology of Freeze/Thawed PVA Hydrogels, Macromolecules 33 (2000) 2472–2479.
[354] Y. Okumura, K. Ito, The polyrotaxane gel: a topological gel by figure-of-eight cross-links, Adv. Mater. 13 (2001) 485–487.
[355] S. Kaessmair, et al., Identification of mechanical models and parameters for alginate-based hydrogels as proxy materials for brain tissue, Proc. Appl. Math. Mech. 20 (2021) e202000338.
[356] D. Caccavo, G. Lamberti, PoroViscoElastic model to describe hydrogels' behavior, Materials Science Engineering C 76 (2017) 102–113.
[357] C. Joly-Duhamel, D. Hellio, M. Djabourov, All Gelatin Networks: 1. Biodiversity and Physical Chemistry, Langmuir 18 (2002) 7208–7217.
[358] T. Behroozi Kohlan, Y. Wen, C. Mini, A. Finne-Wistrand, Schiff base crosslinked hyaluronic acid hydrogels with tunable and cell instructive time-dependent mechanical properties, Carbohydr. Polym. 338 (2024) 122173.
[359] J. Xu, Y. Liu, S.-h Hsu, Hydrogels Based on Schiff Base Linkages for Biomedical Applications, Molecules 24 (2019) 3005.
[360] X. Li, J.P. Gong, Design principles for strong and tough hydrogels, Nat. Rev. Mater. 9 (2024) 380–398.
[361] K.Y. Lee, D.J. Mooney, Alginate: Properties and biomedical applications, Progress. Polym. Sci. 37 (2012) 106–126.
[362] Q. Meng, X. Shi, A mechanistically motivated constitutive model of biopolymer hydrogels with structural evolution, J. Mech. Phys. Solids 173 (2023) 105205.
[363] Y. Mao, S. Lin, X. Zhao, L. Anand, A large deformation viscoelastic model for double-network hydrogels, J. Mech. Phys. Solids 100 (2017) 103–130.
[364] Z. Sheng, J. Ma, Z. Shen, S. Qu, Z. Jia, Chemomechanics Underpinning the Growth and Strengthening Behaviors of Mechanoresponsive Self-Growing Hydrogels, Macromolecules 56 (2023) 9398–9409.
[365] J.P. Gong, Y. Katsuyama, T. Kurokawa, Y. Osada, Double-network hydrogels with extremely high mechanical strength, Adv. Mater. 15 (2003) 1155–1158.
[366] Y. Ren, P.K. Purohit, Numerical experiments with a poro-viscoelastic continuum model for gels, J. Mech. Phys. Solids 211 (2026) 106600.
[367] N.A. Peppas, S.L. Wright, Solute Diffusion in Poly(vinyl alcohol)/Poly(acrylic acid) Interpenetrating Networks, Macromolecules 29 (1996) 8798–8804.
[368] K.A. Rose, et al., Nanoparticle dynamics in hydrogel networks with controlled defects, Soft Matter 18 (2022) 9045–9056.
[369] N.R. Richbourg, N.A. Peppas, Structurally decoupled stiffness and solute transport in multi-arm poly(ethylene glycol) hydrogels, Biomaterials 301 (2023) 122272.
[370] T.-W. Lin, B. Mei, K.S. Schweizer, C.E. Sing, Simulation study of the effects of polymer network dynamics and mesh confinement on the diffusion and structural relaxation of penetrants, J. Chem. Phys. 159 (2023) 014904.

[371] B. Mei, et al., How Segmental Dynamics and Mesh Confinement Determine the Selective Diffusivity of Molecules in Cross-Linked Dense Polymer Networks, ACS Cent. Sci. 9 (2023) 508–518.
[372] M.L. Huggins, Viscoelastic Properties of Polymers, J. Am. Chem. Soc. 83 (1961) 4110–4111.
[373] P. Calvert, Hydrogels for Soft Machines, Adv. Mater. 21 (2009) 743–756.
[374] S.R. Shin, et al., Carbon Nanotube Reinforced Hybrid Microgels as Scaffold Materials for Cell Encapsulation, ACS Nano 6 (2012) 362–372.
[375] K.L. Ngai, "Introduction to the Problems of Relaxation and Diffusion in Complex Systems". Relaxation and Diffusion in Complex Systems, Springer, 2010, pp. 1–47.
[376] J.D. Ferry, H.S. Myers, Viscoelastic Properties of Polymers, J. Electrochem. Soc. 108 (1961) 142C.
[377] H.A. Kramers, Brownian motion in a field of force and the diffusion model of chemical reactions, Physica 7 (1940) 284–304.
[378] B. Mei, et al., Structural Relaxation and Vitrification in Dense Cross-Linked Polymer Networks: Simulation, Theory, and Experiment, Macromolecules 55 (2022) 4159–4173.
[379] M.A. Biot, General Theory of Three-Dimensional Consolidation, J. Appl. Phys. 12 (1941) 155–164.
[380] Y. Hu, X. Zhao, J.J. Vlassak, Z. Suo, Using indentation to characterize the poroelasticity of gels, Appl. Phys. Lett. 96 (2010) 121904.
[381] M.L. Oyen, Mechanical characterisation of hydrogel materials, Int. Mater. Rev. 59 (2014) 44–59.
[382] E.J. Bailey, P.J. Griffin, R.J. Composto, K.I. Winey, Characterizing the Areal Density and Desorption Kinetics of Physically Adsorbed Polymer in Polymer Nanocomposite Melts, Macromolecules 53 (2020) 2744–2753.
[383] S. Yu, F. Tian, X. Shi, Diffusion of deformable nanoparticles in adhesive polymeric gels, J. Mech. Phys. Solids 167 (2022) 105002.
[384] F. Tian, H. Wang, H. Li, P. Cheng, X. Shi, Molecular simulation of diffusion of rigidity-tuned nanoparticles in biological hydrogels, Acta Mech. Sin. 35 (2019) 376–383.
[385] Y. Gu, M.E. Distler, H.F. Cheng, C. Huang, C.A. Mirkin, A General DNA-Gated Hydrogel Strategy for Selective Transport of Chemical and Biological Cargos, J. Am. Chem. Soc. 143 (2021) 17200–17208.
[386] Z. Ma, et al., Controlled tough bioadhesion mediated by ultrasound, Science 377 (2022) 751–755.
[387] H. Tang, et al., Injectable ultrasonic sensor for wireless monitoring of intracranial signals, Nature 630 (2024) 84–90.
[388] Y. Tian, et al., An implantable hydrogel-based phononic crystal for continuous and wireless monitoring of internal tissue strains, Nat. Biomed. Eng. 9 (2025) 1335–1348.
[389] Y. Zhou, G. Liu, S. Guo, Advances in ultrasound-responsive hydrogels for biomedical applications, J. Mater. Chem. B 10 (2022) 3947–3958.
[390] A. Karki, J.S. Marshall, J. Wu, Effect of ultrasound amplitude and frequency on nanoparticle diffusion in an agarose hydrogel, J. Acoust. Soc. Am. 152 (2022) 640–650.
[391] C. Einen, et al., Nanoparticle dynamics in composite hydrogels exposed to low-frequency focused ultrasound, Gels 9 (2023) 771.
[392] A. Leipertz, A.P. Fröba, "Diffusion measurements in fluids by dynamic light scattering". Diffusion in Condensed Matter: Methods, Materials, Models, Springer, 2005, pp. 579–618.
[393] R. Pecora, Dynamic light scattering measurement of nanometer particles in liquids, J. Nanopart. Res. 2 (2000) 123–131.
[394] T. Dertinger, et al., Two-focus fluorescence correlation spectroscopy: A new tool for accurate and absolute diffusion measurements, ChemPhysChem 8 (2007) 433–443.
[395] J.-P. Günther, M. Börsch, P. Fischer, Diffusion measurements of swimming enzymes with fluorescence correlation spectroscopy, Acc. Chem. Res. 51 (2018) 1911–1920.
[396] F. Waharte, K. Steenkeste, R. Briandet, M.-P. Fontaine-Aupart, Diffusion measurements inside biofilms by image-based fluorescence recovery after photobleaching (FRAP) analysis with a commercial confocal laser scanning microscope, Appl. Environ. Microbiol. 76 (2010) 5860–5869.
[397] N.R. Richbourg, N.A. Peppas, High-Throughput FRAP Analysis of Solute Diffusion in Hydrogels, Macromolecules 54 (2021) 10477–10486.
[398] J. Xu, et al., A study on the similarities between water vapor and VOC diffusion in porous media by a dual chamber method, CLEANSoil. Air Water 37 (2009) 444–453.
[399] C.H. Sotak, Nuclear magnetic resonance (NMR) measurement of the apparent diffusion coefficient (ADC) of tissue water and its relationship to cell volume changes in pathological states, Neurochem. Int. 45 (2004) 569–582.
[400] G. Costantini, S. Capuani, F.A. Farrelly, A. Taloni, A new perspective of molecular diffusion by nuclear magnetic resonance, Sci. Rep. 13 (2023) 1703.
[401] B.J. Berne, R. Pecora. Dynamic light scattering: with applications to chemistry, biology, and physics. Courier Corporation, Courier Corporation, 2000.
[402] J. Ortega-Arroyo, P. Kukura, Interferometric scattering microscopy (iSCAT): new frontiers in ultrafast and ultrasensitive optical microscopy, Phys. Chem. Chem. Phys. 14 (2012) 15625–15636.
[403] R.W. Taylor, V. Sandoghdar, "Interferometric scattering (iSCAT) microscopy and related techniques", in: Label-free super-resolution microscopy, Springer, 2019, pp. 25–65.
[404] K.N. Fish, Total internal reflection fluorescence (TIRF) microscopy, Curr. Protoc. Cytom. 50 (2009) 12.18. 11–12.18. 13.
[405] N. Ruthardt, D.C. Lamb, C. Bräuchle, Single-particle tracking as a quantitative microscopy-based approach to unravel cell entry mechanisms of viruses and pharmaceutical nanoparticles, Mol. Ther. 19 (2011) 1199–1211.
[406] N.S. Ginsberg, C.-L. Hsieh, P. Kukura, M. Piliarik, V. Sandoghdar, Interferometric scattering microscopy, Nat. Rev. Methods Prim. 5 (2025) 23.
[407] G. Young, P. Kukura, Interferometric scattering microscopy, Annu. Rev. Phys. Chem. 70 (2019) 301–322.
[408] R.W. Taylor, V. Sandoghdar, Interferometric scattering microscopy: seeing single nanoparticles and molecules via Rayleigh scattering, Nano Lett. 19 (2019) 4827–4835.
[409] N.S. Poulter, W.T. Pitkeathly, P.J. Smith, J.Z. Rappoport, The physical basis of total internal reflection fluorescence (TIRF) microscopy and its cellular applications, Adv. Fluoresc. Microsc. Methods Protoc. (2014) 1–23.
[410] D.R. Gibbs, A. Kaur, A. Megalathan, K. Sapkota, S. Dhakal, Build your own microscope: step-by-step guide for building a prism-based TIRF microscope, Methods Protoc. 1 (2018) 40.
[411] D.S. Johnson, J.K. Jaiswal, S. Simon, Total internal reflection fluorescence (TIRF) microscopy illuminator for improved imaging of cell surface events, Curr. Protoc. Cytom. 61 (2012) 12.29. 11–12.29. 19.
[412] K. Kremer, G.S. Grest, Dynamics of entangled linear polymer melts: A molecular-dynamics simulation, J. Chem. Phys. 92 (1990) 5057–5086.
[413] X. Dai, X. Zhang, L. Gao, Z. Xu, L.-T. Yan, Topology mediates transport of nanoparticles in macromolecular networks, Nat. Commun. 13 (2022).
[414] Z. Xu, et al., Enhanced Heterogeneous Diffusion of Nanoparticles in Semiflexible Networks, ACS Nano 15 (2021) 4608–4616.
[415] M. Quesada-Pérez, J.-A. Maroto-Centeno, M.D.M. Ramos-Tejada, A. Martín-Molina, Coarse-Grained Simulations of Solute Diffusion in Crosslinked Flexible Hydrogels, Macromolecules 55 (2022) 1495–1504.
[416] L. Pérez-Mas, M.D.M. Ramos-Tejada, A. Martín-Molina, J.-A. Maroto-Centeno, M. Quesada-Pérez, Electrostatic hindrance to diffusion in flexible crosslinked gels: A coarse-grained simulation study, J. Chem. Phys. 159 (2023) 014903.
[417] S. Milster, F. Koch, C. Widder, T. Schilling, J. Dzubiella, Tracer dynamics in polymer networks: Generalized Langevin description, J. Chem. Phys. 160 (2024) 094901.
[418] M. Yu, et al., Rotation-Facilitated Rapid Transport of Nanorods in Mucosal Tissues, Nano Lett. 16 (2016) 7176–7182.
[419] M. Yu, et al., Rapid transport of deformation-tuned nanoparticles across biological hydrogels and cellular barriers, Nat. Commun. 9 (2018) 2607.
[420] S.B. Chen, Dissipative Particle Dynamics Simulation of Nanoparticle Diffusion in a Crosslinked Polymer Network, J. Phys. Chem. B 126 (2022) 7184–7191.
[421] B.-R. Zhao, B. Li, Molecular simulation of hopping mechanisms of nanoparticles in regular cross-linked polymer networks, J. Chem. Phys. 157 (2022) 104901.
[422] X. Zhang, et al., Dynamic Heterogeneities of Rod Rotation in Macromolecular Networks, Macromolecules 56 (2023) 8428–8437.
[423] X. He, et al., Extracellular matrix physical properties govern the diffusion of nanoparticles in tumor microenvironment, Proc. Natl. Acad. Sci. 120 (2023).
[424] X. Zhang, et al., Unconventionally fast transport through sliding dynamics of rodlike particles in macromolecular networks, Nat. Commun. 15 (2024) 525.
[425] L. Zhao, S.L. Arias, W. Zipfel, I.L. Brito, J. Yeo, Coarse-grained modeling and dynamics tracking of nanoparticles diffusion in human gut mucus, Int. J. Biol. Macromol. 267 (2024) 131434.
[426] B.-R. Zhao, B. Li, X. Shi, Molecular simulation of the diffusion mechanism of nanorods in cross-linked networks, Nanoscale 13 (2021) 17404–17416.
[427] M.-R. Rokhforouz, D.D. Sin, S. Hedtrich, J.J. Feng, Brownian dynamics simulation of the diffusion of rod-like nanoparticles in polymeric gels, Soft Matter 21 (2025) 5529–5541.
[428] Z. Lv, et al., Unveiling Nanoparticle Diffusion Mechanisms Confined in Different Polymer Topologies, Macromolecules 58 (2025) 11017–11028.
[429] M. Yang, et al., Dynamic Control of Photocatalytic Proton Reduction through the Mechanical Actuation of a Hydrogel Host Matrix, J. Phys. Chem. Lett. 12 (2021) 12135–12141.
[430] Y. Gu, J. Zhao, J.A. Johnson, A (Macro)Molecular-Level Understanding of Polymer Network Topology, Trends Chem. 1 (2019) 318–334.
[431] M. Zhong, R. Wang, K. Kawamoto, B.D. Olsen, J.A. Johnson, Quantifying the impact of molecular defects on polymer network elasticity, Science 353 (2016) 1264–1268.
[432] S.P.O. Danielsen, et al., Molecular Characterization of Polymer Networks, Chem. Rev. 121 (2021) 5042–5092.
[433] L. Li, Z. Liu, R. Qi, Molecular dynamics simulations in hydrogel research and its applications in energy utilization: A review, Energy Rev. 3 (2024) 100072.
[434] Y. Kim, S. Joo, W.K. Kim, J.-H. Jeon, Active Diffusion of Self-Propelled Particles in Flexible Polymer Networks, Macromolecules 55 (2022) 7136–7147.
[435] Y. Kim, W.K. Kim, J.-H. Jeon, Active Diffusion of Self-Propelled Particles in Semiflexible Polymer Networks, 10.1021/acs.macromol.4c00087acs.macromol.4c00087, Macromolecules (2024), 10.1021/acs.macromol.4c00087acs.macromol.4c00087.
[436] J.D. Weeks, D. Chandler, H.C. Andersen, Role of Repulsive Forces in Determining the Equilibrium Structure of Simple Liquids, J. Chem. Phys. 54 (1971) 5237–5247.
[437] P.J. Hoogerbrugge, J.M.V.A. Koelman, Simulating Microscopic Hydrodynamic Phenomena with Dissipative Particle Dynamics, Europhys. Lett. (EPL) 19 (1992) 155–160.
[438] P. Español, P. Warren, Statistical Mechanics of Dissipative Particle Dynamics, Europhys. Lett. (EPL) 30 (1995) 191–196.
[439] R.D. Groot, P.B. Warren, Dissipative particle dynamics: Bridging the gap between atomistic and mesoscopic simulation, J. Chem. Phys. 107 (1997) 4423–4435.
[440] R.D. Groot, K.L. Rabone, Mesoscopic Simulation of Cell Membrane Damage, Morphology Change and Rupture by Nonionic Surfactants, Biophys. J. 81 (2001) 725–736.

[441] Anonymous, "Applications of Dissipative Particle Dynamics". Lecture Notes in Physics, Springer Berlin Heidelberg, Berlin, Heidelberg, 2004, pp. 5–38, https://doi.org/10.1007/978-3-540-39895-0_1.
[442] R.M. Füchslin, H. Fellermann, A. Eriksson, H.-J. Ziock, Coarse graining and scaling in dissipative particle dynamics, J. Chem. Phys. 130 (2009) 214102.
[443] J.R. Spaeth, T. Dale, I.G. Kevrekidis, A.Z. Panagiotopoulos, Coarse-Graining of Chain Models in Dissipative Particle Dynamics Simulations, Ind. & Eng. Chem. Res. 50 (2011) 69–77.
[444] P.M. Morse, Diatomic Molecules According to the Wave Mechanics. II. Vibrational Levels, Phys. Rev. 34 (1929) 57–64.
[445] H. Xia, Y. Xu, Z. Cheng, Y. Cheng, Tetramethylpyrazine-Loaded Hydrogels: Preparation, Penetration Through a Subcutaneous-Mucous-Membrane Model, and a Molecular Dynamics Simulation, AAPS PharmSciTech 18 (2017) 1720–1727.
[446] M. Ernst, et al., A Model for the Transient Subdiffusive Behavior of Particles in Mucus, Biophys. J. 112 (2017) 172–179.
[447] R. Huang, et al., Efficient fabrication of stretching hydrogels with programmable strain gradients as cell sheet delivery vehicles, Materials Science Engineering C 129 (2021) 112415.
[448] M.W. Abebe, R. Appiah-Ntiamoah, H. Kim, Gallic acid modified alginate self-adhesive hydrogel for strain responsive transdermal delivery, Int. J. Biol. Macromol. 163 (2020) 147–155.
[449] K. Mendez, et al., Mechanoresponsive drug release from a flexible, tissue-adherent, hybrid hydrogel actuator, Adv. Mater. 36 (2024) 2303301.
[450] Y. Jia, et al., Hydrogel dressing integrating FAK inhibition and ROS scavenging for mechano-chemical treatment of atopic dermatitis, Nat. Commun. 14 (2023) 2478.
[451] W. Guan, Y. Zhao, C. Lei, G. Yu, Molecularly confined hydration in thermoresponsive hydrogels for efficient atmospheric water harvesting, Proc. Natl. Acad. Sci. 120 (2023) e2308969120.
[452] B. Singh, A. Kumar, Graft and crosslinked polymerization of polysaccharide gum to form hydrogel wound dressings for drug delivery applications, Carbohydr. Res. 489 (2020) 107949.
[453] M. Akrami-Hasan-Kohal, M. Eskandari, A. Solouk, Silk fibroin hydrogel/dexamethasone sodium phosphate loaded chitosan nanoparticles as a potential drug delivery system, Colloids Surf. B Biointerfaces 205 (2021) 111892.
[454] G. Sharifzadeh, H. Hezaveh, I.I. Muhamad, S. Hashim, N. Khairuddin, Montmorillonite-based polyacrylamide hydrogel rings for controlled vaginal drug delivery, Materials Science Engineering C 110 (2020) 110609.
[455] S. Basu, S. Pacelli, A. Paul, Self-healing DNA-based injectable hydrogels with reversible covalent linkages for controlled drug delivery, Acta Biomater. 105 (2020) 159–169.
[456] I.A. Duceac, L. Verestiuc, C.D. Dimitriu, V. Maier, S. Coseri, Design and preparation of new multifunctional hydrogels based on chitosan/acrylic polymers for drug delivery and wound dressing applications, Polymers 12 (2020) 1473.
[457] Y. Yang, et al., Ultra-durable cell-free bioactive hydrogel with fast shape memory and on-demand drug release for cartilage regeneration, Nat. Commun. 14 (2023) 7771.
[458] F. Abasalizadeh, et al., Alginate-based hydrogels as drug delivery vehicles in cancer treatment and their applications in wound dressing and 3D bioprinting, J. Biol. Eng. 14 (2020) 8.
[459] D. Xu, et al., Ultrasound-responsive aligned piezoelectric nanofibers derived hydrogel conduits for peripheral nerve regeneration, Adv. Mater. 36 (2024) 2307896.
[460] S. Wang, H. Liu, D. Wu, X. Wang, Temperature and pH dual-stimuli-responsive phase-change microcapsules for multipurpose applications in smart drug delivery, J. Colloid Interface Sci. 583 (2021) 470–486.
[461] S. Samadzadeh, M. Babazadeh, N. Zarghami, Y. Pilehvar-Soltanahmadi, H. Mousazadeh, An implantable smart hyperthermia nanofiber with switchable, controlled and sustained drug release: Possible application in prevention of cancer local recurrence, Materials Science Engineering C 118 (2021) 111384.
[462] N. Liu, et al., pH/Thermal-sensitive nanoplatform capable of on-demand specific release to potentiate drug delivery and combinational Hyperthermia/Chemo/Chemodynamic Therapy, ACS Appl. Mater. & Interfaces 14 (2022) 29668–29678.
[463] R. Huang, et al., Remotely controlling drug release by light-responsive cholesteric liquid crystal microcapsules triggered by molecular motors, ACS Appl. Mater. & Interfaces 13 (2021) 59221–59230.
[464] I.O. de Solorzano, M. Prieto, G. Mendoza, V. Sebastian, M. Arruebo, Triggered drug release from hybrid thermoresponsive nanoparticles using near infrared light, Nanomedicine 15 (2020) 219–234.
[465] W. Zhang, et al., Light-triggered release of conventional local anesthetics from a macromolecular prodrug for on-demand local anesthesia, Nat. Commun. 11 (2020) 2323.
[466] X. Li, et al., Red light-triggered polyethylene glycol deshielding from photolabile cyanine-modified mesoporous silica nanoparticles for on-demand drug release, ACS Appl. Bio Mater. 3 (2020) 8084–8093.
[467] S. Campbell, et al., Injectable on-demand pulsatile drug delivery hydrogels using alternating magnetic field-triggered polymer glass transitions, ACS Appl. Mater. & Interfaces 15 (2023) 48892–48902.
[468] X. Qu, et al., Photothermal regulated multi-perceptive poly (ionic liquids) hydrogel sensor for bioelectronics, Chem. Eng. J. 453 (2023) 139785.
[469] I. Matai, G. Kaur, S. Soni, A. Sachdev, S. Mishra, Near-infrared stimulated hydrogel patch for photothermal therapeutics and thermoresponsive drug delivery, J. Photochem. Photobiol. B Biol. 210 (2020) 111960.
[470] Q.L. Zhu, et al., Distributed electric field induces orientations of nanosheets to prepare hydrogels with elaborate ordered structures and programmed deformations, Adv. Mater. 32 (2020) 2005567.
[471] X. Yang, et al., Multiple stimuli-responsive MXene-based hydrogel as intelligent drug delivery carriers for deep chronic wound healing, Small 18 (2022) 2104368.
[472] M. Wu, et al., Injectable and self-healing nanocomposite hydrogels with ultrasensitive pH-responsiveness and tunable mechanical properties: implications for controlled drug delivery, Biomacromolecules 21 (2020) 2409–2420.
[473] T. Hornsby, F.M. Kashkooli, A. Jakhmola, M.C. Kolios, J. Tavakkoli, Measuring drug release induced by thermal and non-thermal effects of ultrasound in a nanodrug delivery system. 2022 IEEE International Ultrasonics Symposium (IUS), IEEE, 2022, pp. 1–4.
[474] R.P. Dhavale, et al., Chitosan coated magnetic nanoparticles as carriers of anticancer drug Telmisartan: pH-responsive controlled drug release and cytotoxicity studies, J. Phys. Chem. Solids 148 (2021) 109749.
[475] A.G. Tabriz, et al., 3D printed bilayer tablet with dual controlled drug release for tuberculosis treatment, Int. J. Pharm. 593 (2021) 120147.
[476] Z. Wu, X. Wang, Y. Lu, Q. Xu, Multichamber magnetic capsule robot for selective liquid sampling and drug delivery, Natl. Sci. Rev. 12 (2025) nwaf400.
[477] A. Najafipour, A. Gharieh, A. Fassihi, H. Sadeghi-Aliabadi, A.R. Mahdavian, MTX-loaded dual thermoresponsive and pH-responsive magnetic hydrogel nanocomposite particles for combined controlled drug delivery and hyperthermia therapy of cancer, Mol. Pharm. 18 (2020) 275–284.
[478] T. Mahmood, et al., Preparation, in vitro characterization, and evaluation of polymeric pH-responsive hydrogels for controlled drug release, ACS Omega 9 (2024) 10498–10516.
[479] Q. Truong Hoang, et al., Oxygen-supplying piezocatalytic therapy of hypoxic tumors by intratumoral delivery of pH-responsive multicompartmental carriers with sequential drug release capability, Adv. Funct. Mater. 34 (2024) 2306078.
[480] J. Ding, et al., Temperature-responsive hydrogel system integrating wound temperature monitoring and on-demand drug release for sequentially inflammatory process regulation of wound healing, ACS Appl. Mater. & Interfaces 16 (2024) 67444–67457.
[481] X. Gong, C. Hou, Q. Zhang, Y. Li, H. Wang, Thermochromic hydrogel-functionalized textiles for synchronous visual monitoring of on-demand in vitro drug release, ACS Appl. Mater. & Interfaces 12 (2020) 51225–51235.
[482] X. Ji, et al., Injectable immunomodulation-based porous chitosan microspheres/HPCH hydrogel composites as a controlled drug delivery system for osteochondral regeneration, Biomaterials 285 (2022) 121530.
[483] P. Gheysoori, A. Paydayesh, M. Jafari, H. Peidayesh, Thermoresponsive nanocomposite hydrogels based on Gelatin/poly (N–isopropylacrylamide) (PNIPAM) for controlled drug delivery, Eur. Polym. J. 186 (2023) 111846.
[484] S. Zu, et al., A bioinspired 4D printed hydrogel capsule for smart controlled drug release, Mater. Today Chem. 24 (2022) 100789.
[485] M. Zhu, S. Zhang, X. Li, C. Xiao, N. Wang, A crosslinked PVA/GO hydrogel for wound dressing with pH-controlled drug release capabilities, Mater. Today Commun. 43 (2025) 111760.
[486] Z. Han, et al., Dual pH-responsive hydrogel actuator for lipophilic drug delivery, ACS Appl. Mater. & Interfaces 12 (2020) 12010–12017.
[487] Z. Guo, H. Li, J. Ma, G. Xu, Q. Jia, pH-sensitive metal–organic framework carrier decorated with chitosan for controlled drug release, Int. J. Pharm. 667 (2024) 124933.
[488] C. Wang, et al., A novel high doxorubicin-loaded Fe3O4@ void@ ZnO nanocomposite: pH-controlled drug release and targeted antitumor activity, J. Mater. Sci. 55 (2020) 16718–16729.
[489] F. Damiri, Y. Bachra, C. Bounacir, A. Laaraibi, M. Berrada, Synthesis and characterization of Lyophilized chitosan-based hydrogels cross-linked with benzaldehyde for controlled drug release, J. Chem. 2020 (2020) 8747639.
[490] Y. Yang, et al., Light-activatable liposomes for repetitive on-demand drug release and immunopotentiation in hypoxic tumor therapy, Biomaterials 265 (2021) 120456.
[491] H.T. Hoang, et al., Dual cross-linked chitosan/alginate hydrogels prepared by Nb-Tz 'click'reaction for pH responsive drug delivery, Carbohydr. Polym. 288 (2022) 119389.
[492] H. Guo, et al., Injectable and self-healing hydrogels with double-dynamic bond tunable mechanical, gel–sol transition and drug delivery properties for promoting periodontium regeneration in periodontitis, ACS Appl. Mater. & Interfaces 13 (2021) 61638–61652.
[493] Y. Wang, et al., Ultrasound-triggered piezocatalysis for selectively controlled NO gas and chemodrug release to enhance drug penetration in pancreatic cancer, ACS nano 17 (2023) 3557–3573.
[494] S. Wu, et al., Ultrasound-triggered in situ gelation with ROS-controlled drug release for cartilage repair, Mater. Horiz. 10 (2023) 3507–3522.
[495] J.H. Arrizabalaga, et al., Ultrasound-responsive hydrogels for on-demand protein release, ACS Appl. bio Mater. 5 (2022) 3212–3218.
[496] R.D. Field, et al., Ultrasound-Responsive Aqueous Two-Phase Microcapsules for On-Demand Drug Release, Angew. Chem. 134 (2022) e202116515.
[497] T. Kim, et al., Deep brain stimulation by blood–brain-barrier-crossing piezoelectric nanoparticles generating current and nitric oxide under focused ultrasound, Nat. Biomed. Eng. 7 (2023) 149–163.
[498] W. Xu, Y. Hong, A. Song, J. Hao, Peptide-assembled hydrogels for pH-controllable drug release, Colloids Surf. B Biointerfaces 185 (2020) 110567.
[499] M. Du, et al., Ultrasound responsive magnetic mesoporous silica nanoparticle-loaded microbubbles for efficient gene delivery, ACS Biomater. Sci. & Eng. 6 (2020) 2904–2912.
[500] Y. Zhao, et al., Incorporating pH/NIR responsive nanocontainers into a smart self-healing coating for a magnesium alloy with controlled drug release, bacteria killing and osteogenesis properties, Acta Biomater. 174 (2024) 463–481.

[501] Y. Cao, Y. Cheng, G. Zhao, Near-infrared light-, magneto-, and pH-responsive GO–Fe3O4/poly (N-isopropylacrylamide)/alginate nanocomposite hydrogel microcapsules for controlled drug release, Langmuir 37 (2021) 5522–5530.
[502] Y. Kwon, et al., Freeze-Induced Protein Assembly of α-Synuclein into Stable Microspheres to Fabricate Light-Induced Cargo Release Systems, ACS Appl. Mater. & Interfaces 17 (2024) 594–606.
[503] Y. Hu, et al., Photo-controllable drug releasing bulk polyacrylic intraocular lens material for safer posterior capsular opacification prevention, J. Control. Release 366 (2024) 494–504.
[504] A. Brion, et al., Red light-responsive upconverting nanoparticles for quantitative and controlled release of a coumarin-based prodrug, Adv. Healthc. Mater. 12 (2023) 2201474.
[505] Y. Meng, et al., Molecular Trojan Based on Membrane-Mimicking Conjugated Electrolyte for Stimuli-Responsive Drug Release, Adv. Mater. 37 (2025) 2415705.
[506] X. Xu, et al., Near-infrared light-triggered degradable hyaluronic acid hydrogel for on-demand drug release and combined chemo-photodynamic therapy, Carbohydr. Polym. 229 (2020) 115394.
[507] Y. Kim, et al., Azobenzene-grafted carboxymethyl cellulose hydrogels with photo-switchable, reduction-responsive and self-healing properties for a controlled drug release system, Int. J. Biol. Macromol. 163 (2020) 824–832.
[508] S. Nisar, A.H. Pandit, L.-F. Wang, S. Rattan, Strategy to design a smart photocleavable and pH sensitive chitosan based hydrogel through a novel crosslinker: A potential vehicle for controlled drug delivery, RSC Adv. 10 (2020) 14694–14704.
[509] Y. Tong, et al., Urea-bond scission induced by therapeutic ultrasound for biofunctional molecule release, J. Am. Chem. Soc. 144 (2022) 16799–16807.
[510] N. Mamidi, R.M.V. Delgadillo, Design, fabrication and drug release potential of dual stimuli-responsive composite hydrogel nanoparticle interfaces, Colloids Surf. B Biointerfaces 204 (2021) 111819.
[511] J. Chai, et al., Assembled Fe3O4 nanoparticles on ZnAl LDH nanosheets as a biocompatible drug delivery vehicle for pH-responsive drug release and enhanced anticancer activity, Appl. Clay Sci. 228 (2022) 106630.
[512] A. Pourjavadi, M. Kohestanian, C. Streb, pH and thermal dual-responsive poly (NIPAM-co-GMA)-coated magnetic nanoparticles via surface-initiated RAFT polymerization for controlled drug delivery, Materials Science Engineering C 108 (2020) 110418.
[513] T.T. Vu, M. Gulfam, S.-H. Jo, S.-H. Park, K.T. Lim, Injectable and biocompatible alginate-derived porous hydrogels cross-linked by IEDDA click chemistry for reduction-responsive drug release application, Carbohydr. Polym. 278 (2022) 118964.
[514] Y. Zeng, et al., Metal-organic framework-based hydrogel with structurally dynamic properties as a stimuli-responsive localized drug delivery system for cancer therapy, Acta Biomater. 145 (2022) 43–51.
[515] S. Wang, et al., A hydrogel-based drug delivery system reduces inflammation and oxidative stress to alleviate intervertebral disc degeneration, Acta Biomater. (2025).
[516] R.J. Nims, et al., A synthetic mechanogenetic gene circuit for autonomous drug delivery in engineered tissues, Sci. Adv. 7 (2021) eabd9858.
[517] F. Wu, Y. Pang, J. Liu, Swelling-strengthening hydrogels by embedding with deformable nanobarriers, Nat. Commun. 11 (2020) 4502.
[518] L. Wang, et al., Hydrogel-functionalized bandages with Janus wettability for efficient unidirectional drug delivery and wound care, Acs Nano 18 (2024) 3468–3479.
[519] L. Zhang, et al., Near-infrared triggered injectable ferrimagnetic chitosan thermosensitive hydrogel for photo hyperthermia and precisely controlled drug release in tumor ablation, Eur. Polym. J. 162 (2022) 110879.
[520] S. Chen, et al., Macrophage hitchhiking nanomedicine for enhanced β-elemene delivery and tumor therapy, Sci. Adv. 11 (2025) eadw7191.
[521] L. Wu, et al., A Light-Driven Electrochromic Materials-Based Nanomotor for H2S-Controlled Drug Release in Synergistic Cancer Chemotherapy Immunotherapy, Angew. Chem. 137 (2025) e202503297.
[522] X. Yin, et al., Palladium nanoparticle based smart hydrogels for NIR light-triggered photothermal/photodynamic therapy and drug release with wound healing capability, Nanoscale Adv. 5 (2023) 1729–1739.
[523] H. Joo, et al., Soft implantable drug delivery device integrated wirelessly with wearable devices to treat fatal seizures, Sci. Adv. 7 (2021) eabd4639.
[524] C. Wu, et al., Self-powered iontophoretic transdermal drug delivery system driven and regulated by biomechanical motions, Adv. Funct. Mater. 30 (2020) 1907378.
[525] Y.-H. An, et al., Facilitated transdermal drug delivery using nanocarriers-embedded electroconductive hydrogel coupled with reverse electrodialysis-driven iontophoresis, ACS nano 14 (2020) 4523–4535.
[526] D. Aycan, F. Karaca, A. Koca, N. Alemdar, Electro-stimulated drug release by methacrylated hyaluronic acid-based conductive hydrogel with enhanced mechanical properties, Int. J. Biol. Macromol. 231 (2023) 123297.
[527] X. Wang, et al., NIR-cleavable and pH-responsive polymeric yolk–shell nanoparticles for controlled drug release, Biomacromolecules 24 (2023) 2009–2021.
[528] A. Anwar, et al., Chitosan-based Dy2O3/CuFe3O4 bio-nanocomposite development, characterization, and drug release kinetics, Int. J. Biol. Macromol. 220 (2022) 788–801.
[529] D. Wu, et al., Nanoengineered on-demand drug delivery system improves efficacy of pharmacotherapy for epilepsy, Sci. Adv. 8 (2022) eabm3381.
[530] K. Ding, et al., NIR light-induced tumor phototherapy using ICG delivery system based on platelet-membrane-camouflaged hollow bismuth selenide nanoparticles, Chin. Chem. Lett. 31 (2020) 1168–1172.
[531] Y. Sun, et al., A self-powered wound dressing based on "Lock-ON/OFF" drug release combined electric stimulus therapy for accelerated infected wound healing, Adv. Funct. Mater. 34 (2024) 2315086.
[532] Y. Li, et al., Preparation of pH-responsive cellulose nanofibril/sodium alginate based hydrogels for drug release, J. Appl. Polym. Sci. 139 (2022) 51647.
[533] N. Mamidi, R.M. Velasco Delgadillo, E.V. Barrera, Covalently functionalized carbon nano-onions integrated gelatin methacryloyl nanocomposite hydrogel containing γ-cyclodextrin as drug carrier for high-performance pH-triggered drug release, Pharmaceuticals 14 (2021) 291.
[534] K.E. Balan, C. Boztepe, A. Künkül, Modeling the effect of physical crosslinking degree of pH and temperature responsive poly (NIPAAm-co-VSA)/alginate IPN hydrogels on drug release behavior, J. Drug. Deliv. Sci. Technol. 75 (2022) 103671.
[535] J. Luo, et al., Constructing a drug release model by central composite design to investigate the interaction between drugs and temperature-sensitive controlled release nanoparticles, Eur. J. Pharm. Biopharm. 183 (2023) 24–32.
[536] R. Jahanban-Esfahlan, et al., A bio-inspired magnetic natural hydrogel containing gelatin and alginate as a drug delivery system for cancer chemotherapy, Int. J. Biol. Macromol. 156 (2020) 438–445.
[537] H. Motasadizadeh, et al., Dual drug delivery system of teicoplanin and phenamil based on pH-sensitive silk fibroin/sodium alginate hydrogel scaffold for treating chronic bone infection, Biomater. Adv. 139 (2022) 213032.
[538] M.H. Karami, et al., Novel chitosan/γ-alumina/carbon quantum dot hydrogel nanocarrier for targeted drug delivery, Int. J. Biol. Macromol. 251 (2023) 126280.
[539] W. Wang, et al., Systemic immune responses to irradiated tumours via the transport of antigens to the tumour periphery by injected flagellate bacteria, Nat. Biomed. Eng. 6 (2022) 44–53.
[540] D. Lopez, E. Lauga, Dynamics of swimming bacteria at complex interfaces, Phys. Fluids 26 (2014).
[541] K.M. Thormann, C. Beta, M.J. Kühn, Wrapped Up: The Motility of Polarly Flagellated Bacteria, Annu. Rev. Microbiol. 76 (2022) 349–367.
[542] S.S. Suarez, A.A. Pacey, Sperm transport in the female reproductive tract, Human. Reprod. Update 12 (2005) 23–37.
[543] F.A. García-Vázquez, J. Gadea, C. Matás, W.V. Holt, Importance of sperm morphology during sperm transport and fertilization in mammals, Asian J. Androl. 18 (2016) 844–850.
[544] N. Kumar, A.K. Singh, The anatomy, movement, and functions of human sperm tail: an evolving mystery, Biol. Reprod. 104 (2020) 508–520.
[545] T. Hino, R. Yanagimachi, Active peristaltic movements and fluid production of the mouse oviduct: their roles in fluid and sperm transport and fertilization, Biol. Reprod. 101 (2019) 40–49.
[546] M.R. Stehnach, N. Waisbord, D.M. Walkama, J.S. Guasto, Viscophobic turning dictates microalgae transport in viscosity gradients, Nat. Phys. 17 (2021) 926–930.
[547] T. Pan, et al., Bio-Micromotor Tweezers for Noninvasive Bio-Cargo Delivery and Precise Therapy, Adv. Funct. Mater. 32 (2022) 2111038.
[548] Z. Ouyang, C. Liu, J. Lin, F. Bao, C. Tu, Motion of a single microalga with one defective flagellum, J. Fluid. Mech. 1010 (2025) A20.
[549] A. Shi, H. Wu, D.K. Schwartz, Nanomotor-enhanced transport of passive Brownian particles in porous media, Sci. Adv. 9 (2023) eadj2208.
[550] A. Wysocki, R.G. Winkler, G. Gompper, Propagating interfaces in mixtures of active and passive Brownian particles, New. J. Phys. 18 (2016) 123030.
[551] F. Zhang, et al., Biohybrid Microalgae Robots: Design, Fabrication, Materials, and Applications, Adv. Mater. 36 (2024) 2303714.
[552] Z. Wang, et al., Light-Directed Microalgae Micromotor with Supramolecular Backpacks for Photodynamic Therapy, Adv. Funct. Mater. 35 (2025) 2411070.
[553] H. Zhou, et al., Hydrogel-Based Stimuli-Responsive Micromotors for Biomedicine, Cyborg Bionic Syst. 2022 (2022).
[554] J. Li, B. Esteban-Fernández de Ávila, W. Gao, L. Zhang, J. Wang, Micro/nanorobots for biomedicine: Delivery, surgery, sensing, and detoxification, Sci. Robot. 2 (2017) eaam6431.
[555] C. Bechinger, et al., Active particles in complex and crowded environments, Rev. Mod. Phys. 88 (2016) 045006.
[556] Y. Kim, W.K. Kim, J.-H. Jeon, Active Diffusion of Self-Propelled Particles in Semiflexible Polymer Networks, Macromolecules 57 (2024) 7735–7744.
[557] B. Lukić, et al., Direct Observation of Nondiffusive Motion of a Brownian Particle, Phys. Rev. Lett. 95 (2005) 160601.
[558] U. Basu, P.L. Krapivsky, S.N. Majumdar, Universal dynamics of a passive particle driven by Brownian motion, Phys. Rev. E 110 (2024) 064105.
[559] J. Elgeti, R.G. Winkler, G. Gompper, Physics of microswimmers—single particle motion and collective behavior: a review, Rep. Progress. Phys. 78 (2015) 056601.
[560] S.Y. Kim, et al., Static-state particle fabrication via rapid vitrification of a thixotropic medium, Nat. Commun. 12 (2021) 3768.
[561] J. Zhang, B.A. Grzybowski, S. Granick, Janus Particle Synthesis, Assembly, and Application, Langmuir 33 (2017) 6964–6977.
[562] A. Walther, A.H. Müller, Janus particles, Soft Matter 4 (2008) 663–668.
[563] F.J. Sevilla, P. Castro-Villarreal, Generalized persistence dynamics for active motion, Phys. Rev. E 104 (2021) 064601.
[564] A. Martínez-Calvo, C. Trenado-Yuste, S.S. Datta, "Active Transport in Complex Environments", in: C. Kurzthaler, L. Gentile, H.A. Stone (Eds.), Out-of-equilibrium Soft Matter, The Royal Society of Chemistry, 2023, p. 0, https://doi.org/10.1039/9781839169465-00151.
[565] A.G. Prabhune, A.S. García-Gordillo, I.S. Aranson, T.R. Powers, N. Figueroa-Morales, Bacteria Navigate Anisotropic Media using a Flagellar Tug-of-Oars, PRX Life 2 (2024) 033004.

[566] C.-k Tung, et al., Fluid viscoelasticity promotes collective swimming of sperm, Sci. Rep. 7 (2017) 3152.
[567] J.-J. Oh, et al., Growth, Distribution, and Photosynthesis of Chlamydomonas reinhardtii in 3D Hydrogels, Adv. Mater. 36 (2024) 2305505.
[568] P. Piranfar, M. Naraghi, A.K. Egoli, Design and analysis of a novel magnetic helical swimmer, J. Fluids Struct. 126 (2024) 104093.
[569] L. Li, S.E. Spagnolie, Swimming and pumping of rigid helical bodies in viscous fluids, Phys. Fluids 26 (2014).
[570] I.S.M. Khalil, et al., Swimming Back and Forth Using Planar Flagellar Propulsion at Low Reynolds Numbers, Adv. Sci. 5 (2018) 1700461.
[571] T. Li, et al., Magnetically Propelled Fish-Like Nanoswimmers, Small 12 (2016) 6098–6105.
[572] R. Mhanna, et al., Artificial bacterial flagella for remote-controlled targeted single-cell drug delivery, Small 10 (2014) 1953–1957.
[573] T.H. Wong, et al., Tissue-adhesive hydrogel–MXene biosensor for in situ intraoral TNF-α detection, Sci. Adv. 12 (2026) eady9180.
[574] B. Wang, et al., Next-generation biosensing for in situ monitoring, Nat. Sens. 1 (2026) 111–130.
[575] G. Rong, S.R. Corrie, H.A. Clark, vivo biosensing: progress and perspectives, ACS Sens. 2 (2017) 327–338.
[576] T.H. Wong, et al., Electrical Tissue Adhesives for Strain-Insensitive In-situ Biosensing, Adv. Intell. Syst. (2024) 2400697.
[577] M. Hemdan, et al., Innovations in biosensor technologies for healthcare diagnostics and therapeutic drug monitoring: applications, recent progress, and future research challenges, Sensors 24 (2024) 5143.
[578] Z. Zhao, et al., Bionic engineered protein coating boosting anti-biofouling in complex biological fluids, Adv. Mater. 35 (2023) 2208824.
[579] A. Barfidokht, J.J. Gooding, Approaches toward allowing electroanalytical devices to be used in biological fluids, Electroanalysis 26 (2014) 1182–1196.
[580] R.T. Arwani, et al., Stretchable ionic–electronic bilayer hydrogel electronics enable in situ detection of solid-state epidermal biomarkers, Nat. Mater. 23 (2024) 1115–1122.
[581] S. Li, et al., Implantable hydrogel-protective DNA aptamer-based sensor supports accurate, continuous electrochemical analysis of drugs at multiple sites in living rats, ACS nano 17 (2023) 18525–18538.
[582] A. GhavamiNejad, et al., Continuous insulin monitoring using an antibody-protecting zwitterionic microneedle patch, Nat. Biomed. Eng. (2025) 1–13.
[583] X. Xie, et al., Reduction of measurement noise in a continuous glucose monitor by coating the sensor with a zwitterionic polymer, Nat. Biomed. Eng. 2 (2018) 894–906.
[584] H. Hu, P. Busa, Y. Zhao, C. Zhao, Externally triggered drug delivery systems, Smart Mater. Med. 5 (2024) 386–408.
[585] S. Nag, S. Mohanto, M.G. Ahmed, V. Subramaniyan, Smart" stimuli-responsive biomaterials revolutionizing the theranostic landscape of inflammatory arthritis, Mater. Today Chem. 39 (2024) 102178.
[586] T.C. Ezike, et al., Advances in drug delivery systems, challenges and future directions, Heliyon 9 (2023).
[587] T. Alejo, L. Uson, M. Arruebo, Reversible stimuli-responsive nanomaterials with on-off switching ability for biomedical applications, J. Control. Release 314 (2019) 162–176.
[588] J. Wang, J.A. Kaplan, Y.L. Colson, M.W. Grinstaff, Mechanoresponsive materials for drug delivery: Harnessing forces for controlled release, Adv. Drug. Deliv. Rev. 108 (2017) 68–82.
[589] M. Zuo, et al., Ultrasound-activated mechanochemical reactions for controllable biomedical applications, Smart Mater. Med. 5 (2024) 461–476.
[590] F. Gerayeli, N. Khalef, A. Bakri, P. Benech, D.K. Martin, Ultrasound-stimulated Brownian ratchet enhances diffusion of molecules retained in hydrogels, Nanomed. Nanotechnol. Biol. Med. 31 (2021) 102308.
[591] X. Lu, et al., Parametric study of acoustic droplet vaporization thresholds and payload release from acoustically-responsive scaffolds, Ultrasound Med. & Biol. 45 (2019) 2471–2484.
[592] J. Lee, J.-W. Kim, S.-H. Kim, Microfluidic production of hydrogel-shelled microcapsules and their applications, Curr. Opin. Colloid & Interface Sci. 78 (2025) 101936.
[593] B. Liu, K. Chen, Advances in hydrogel-based drug delivery systems, Gels 10 (2024) 262.
[594] V. Gounden, M. Singh, Hydrogels and wound healing: current and future prospects, Gels 10 (2024) 43.
[595] W. Zhang, et al., Hydrogel-based dressings designed to facilitate wound healing, Mater. Adv. 5 (2024) 1364–1394.
[596] M. Madaghiele, C. Demitri, A. Sannino, L. Ambrosio, Polymeric hydrogels for burn wound care: Advanced skin wound dressings and regenerative templates, 2321-3868, Burns & Trauma. 2 (2014) 143616.
[597] H. Montazerian, et al., Engineered hemostatic biomaterials for sealing wounds, Chem. Rev. 122 (2022) 12864–12903.
[598] W. Han, S. Wang, Advances in hemostatic hydrogels that can adhere to wet surfaces, Gels 9 (2022) 2.
[599] Y. Gao, et al., Hydrogel–mesh composite for wound closure, Proc. Natl. Acad. Sci. 118 (2021) e2103457118.
[600] Z. Bei, et al., Thermostimulated shrinking and adhesive hydrogel dressing for treating chronic diabetic wounds, Cell. Rep. Phys. Sci. 5 (2024).
[601] C. Liu, et al., Mechanically Active and Antimicrobial Wound Closure Using an Adhesive Hydrogel-Elastomer, ACS Pharmacol. & Transl. Sci. 8 (2025) 2795–2803.
[602] M.M. Fareed, S. Shityakov, Next-Generation hydrogel design: computational advances in synthesis, characterization, and biomedical applications, Polymers 17 (2025) 1373.
[603] R.A. Patel, M.A. Webb, Data-driven design of polymer-based biomaterials: high-throughput simulation, experimentation, and machine learning, ACS Appl. Bio Mater. 7 (2023) 510–527.
[604] P.A. Beaucage, D.R. Sutherland, T.B. Martin, Automation and machine learning for accelerated polymer characterization and development: past, potential, and a path forward, Macromolecules 57 (2024) 8661–8670.
[605] J. Zhang, et al., Rapid, autonomous high-throughput characterization of hydrogel rheological properties via automated sensing and physics-guided machine learning, Appl. Mater. Today 30 (2023) 101720.
[606] I. Malashin, V. Tynchenko, A. Gantimurov, V. Nelyub, A. Borodulin, Physics-informed neural networks in polymers: a review, Polymers 17 (2025) 1108.
[607] C. Fernandes, Scientific Machine Learning for Polymeric Materials, Polymers 17 (2025) 2222.
[608] R. Dangayach, et al., Machine learning-aided inverse design and discovery of novel polymeric materials for membrane separation, Environ. Sci. & Technol. 59 (2024) 993–1012.
[609] J. Wang, Y. Wang, Y. Chen, Inverse design of materials by machine learning, Materials 15 (2022) 1811.
[610] N. Richbourg, M.E. Wechsler, J.J. Rodriguez-Cruz, N.A. Peppas, Model-based modular hydrogel design, Nat. Rev. Bioeng. 2 (2024) 575–587.